NASA CONTRACTOR
REPORT

NASA CR-61331

RISE AND GROWTH OF SPACE VEHICLE ENGINE EXHAUST AND ASSOCIATED DIFFUSION MODELS

By Scott D. Thayer, Martin W. Chandler,
and Roland T. Chu

Geomet, Inc.
326 East Montgomery Ave.
Rockville, Maryland 20850

July 1970

Prepared for

NASA-GEORGE C. MARSHALL SPACE FLIGHT CENTER
Marshall Space Flight Center, Alabama 35812

TECHNICAL REPORT STANDARD TITLE PAGE

1. Report No. CR-61331	2. Government Accession No.	3. Recipient's Catalog No.
4. Title and Subtitle RISE AND GROWTH OF SPACE VEHICLE ENGINE EXHAUST AND ASSOCIATED DIFFUSION MODELS		5. Report Date July 1970 6. Performing Organization Code
7. Author(s) Scott D. Thayer, Martin W. Chandler and Roland T. Chu		8. Performing Organization Report No.
9. Performing Organization Name and Address GEOMET, Inc. 326 East Montgomery Ave. Rockville, Maryland 20850		10. Work Unit No. 11. Contract or Grant No. NAS8-24438
12. Sponsoring Agency Name and Address NASA-George C. Marshall Space Flight Center Marshall Space Flight Center, Al. 35812		13. Type of Report and Period Covered Contractor 14. Sponsoring Agency Code
15. Supplementary Notes Contract Monitor: Charles K. Hill, Aerospace Environment Division, Aero-Astrodynamics Laboratory.		

16. Abstract

The principal technical objectives under this contract involved the study of space vehicle plume rise and the development of diffusion models for normal and abnormal operations in the 5 to 30 km region of the atmosphere for launches conducted at the Kennedy Space Flight Center.

The work was carried out in the form of two separate and independent tasks as indicated in the contract title; the first task (described in section 2.0) involved the analysis of films of the exhaust clouds from static rocket engine test firings at MSFC and the use of these data in theoretical and statistical investigations to study the rise and growth of such clouds. The second task (described in section 3.0) consisted of the development of a predictive model to describe the diffusion and fallout of debris from rocket engine exhausts in launches from the Kennedy Space Flight Center (KSC) launch area. The background and objectives for each of these two major tasks are discussed in their respective sections (2.0 and 3.0).

17. Key Words	18. Distribution Statement FOR PUBLIC RELEASE: E. D. Geissler Dir., Aero-Astrodynamics Lab.		
19. Security Classif. (of this report) Unclassified	20. Security Classif. (of this page) Unclassified	21. No. of Pages 207	22. Price

Figure 2A. Technical Report Standard Title Page. This page provides the data elements required by DoD Form DD-1473, HEW Form OE-6000 (ERIC), and similar forms.

FOREWORD

This report is submitted to the National Aeronautics and Space Administration, George C. Marshall Space Flight Center, Huntsville, Alabama in partial fulfillment of the requirements under Contract No. NAS8-24438. The principal technical objectives under this contract involved the study of space vehicle plume rise and the development of diffusion models for normal and abnormal operations in the 5 to 30 km region of the atmosphere for launches conducted at the Kennedy Space Flight Center.

The films and meteorological data used in the analysis of clouds generated by static firings and the vehicle trajectory data used in generating the inputs for the trial case of the diffusion model were supplied by the following: Mr. Charles K. Hill, the Contracting Officer's Representative, Mr. John W. Kaufman, the alternate Contracting Officer's Representative of the Atmospheric Dynamics Branch of the Aero- Astro-Dynamics Laboratory, and Mr. William W. Vaughan, Chief of the Aerospace Environment Division at the George C. Marshall Space Flight Center.

TABLE OF CONTENTS

TABLE OF CONTENTS (Cont'd)

TABLE OF CONTENTS (Cont'd)

TABLE OF CONTENTS (Cont'd)

LIST OF TABLES AND FIGURES

TABLES

LIST OF TABLES AND FIGURES

TABLES (Cont'd)

LIST OF TABLES AND FIGURES

TABLES (Cont'd)

LIST OF TABLES AND FIGURES

TABLES (Cont'd)

FIGURES

LIST OF TABLES AND FIGURES

FIGURES (Cont'd)

LIST OF SYMBOLS AND DEFINITIONS

Section 2.0

Symbol	Definition
a_1, a_2	empirical constants used to derive diffusion parameter k from mean wind speed $\overline{u}$
A	cloud area in the data analysis, heat source parameter in the physical-numerical model
A_1, A_2, A^*	cloud area in phase 1, phase 2 and phase 1 plus 2, respectively
c	spreading coefficient
c_p	specific heat of exhaust gas at constant pressure
D	duration of rocket engine firing
F	fuel ratio in engine data, radial turbulent heat flux in the physical-numerical model
F^*	gas flow
g	acceleration due to gravity
H	actual height of tower on film
H_A	height of tower measured by the analyzer
k	diffusion parameter
K	eddy viscosity
M_o	molecular weight of exhaust gas
N	number of film frame
N_i	initial number of film frame
p	pressure of exhaust gas
$\overline{p}$	average pressure in layers of phase 1, phase 2, or phase 1 plus phase 2
Q	heat source strength

Symbol	Definition
r	radius of a circular-symmetric cloud
R	lateral extent of the exhaust cloud
R^*	universal gas constant
RH	relative humidity
$\overline{RH}$	average relative humidity in layers of phase 1, phase 2, or phase 1 plus phase 2
R_s	reading of film measurement of exhaust cloud by reader S
t	time
$\overline{T}$	average temperature in layers of phase 1, phase 2, or phase 1 plus phase 2
TH	rocket engine thrust
T_{gas}	temperature of exhaust gas
u	wind speed
$\overline{u}$	average wind speed in layers of phase 1, phase 2 or phase 1 plus phase 2
V	exit velocity of exhaust gas
w	vertical velocity of exhaust gas
w_o	initial vertical velocity of exhaust gas
w_1, w_2	vertical velocity of exhaust gas during phase 1 and phase 2, respectively
x	horizontal distance from the source point in the x-direction
X_A	coordinate of x as measured by the analyzer
X_F	coordinate of the initial firing point as measured by the analyzer

Symbol	Definition
Y	horizontal distance from the source point in the Y-direction
z	vertical distance from the source point
z_o	height of heat source in the physical-numerical model, height of launching pad in the statistical analyses
z_1, z_2	height of exhaust cloud rise in phase 1 and phase 2, respectively
z_m	maximum height of exhaust cloud rise
z^*	height of deflector
Z_A	coordinate of z as measured by the analyzer
Z_F	vertical coordinate of the initial firing point as measured by the analyzer
[illegible]	deflector angle
[illegible]	potential temperature of exhaust gas
[illegible]$_e$	ambient potential temperature
[illegible]$'$	potential temperature excess of exhaust gas
[illegible]$'_o$	initial potential temperature excess of exhaust gas
[illegible]$'_1$	potential temperature excess of exhaust gas at the transition height
[illegible]	the ratio of the circumference of a circle to its diameter (3.1416)
[illegible]	density of exhaust gas
[illegible]	**mean density of air in layers of phase 1, phase 2 or phase 1 plus phase 2**

Symbol	Definition
σ_A	standard deviation for a group of corrected exhaust cloud data
σ_B	standard deviation for a group of uncorrected exhaust cloud data
σ_D	the difference between σ_A and σ_B
τ	vertical turbulent shearing stress

Section 3.0

a	x coordinate of exit point of trajectory from layer in meteorological coordinate system
a_k	average along wind shear in k^{th} layer
A	parameter used in line integration to find concentration
b	y coordinate of exit point of trajectory from layer in meteorological coordinate system
b_k	alongwind component of the wind at the base of the k^{th} layer
B_3	third Bernoulli number
B	parameter used in line integration to find concentration
c_k	average lateral shear in k^{th} layer
$\overline{dT}/dz$	average thermal gradient in °C for k^{th} layer
$d\ell/dt$	speed of vehicle along trajectory
D	dosage
D^*	corrected dosage
D_{AT}	total dosage for abort
D_L	dosage for line source
D_m	molecular diffusivity

Symbol	Definition
D_p	dosage for point source
d_K'	lateral component of wind at base of k^{th} layer
e	base of natural logrithms = 2.718...
exp (x)	exponential function = e^x
erf (x)	error function = $2/\sqrt{\pi} \int_0^x \exp - q^2 \, dq$
F_c (x)	finite cosine transform of x
F	parameter used in line integration to find dosage
f (x,y,z)	initial distribution of material from source
G	parameter used in line integration to find dosage
H	thickness of layer
H_a	height of abort after stabilization
H_1, H_2	vertical coordinates of the upper and lower boundaries of the k layer with respect to the L coordinate system
i	summation index
k_1	twice the northerly component of the mean wind in the k^{th} layer
k_2	twice the easterly component of the mean wind in the k^{th} layer
k_x	eddy diffusivity in alongwind direction
k_y	eddy diffusivity in lateral direction
k_z	eddy diffusivity in vertical direction
k	average eddy diffusivity in vertical direction; layer index
L	layer index
ℓ	length along trajectory
m	summation index; power of y used in calculating moments

Symbol	Definition
$\dot{m}$	mass flow rate of vehicle exhaust
n	summation index; power of x used in calculating moments
Q	source strength
Q_P	source strength for point
Q_L	source strength for line
r_x	alongwind reference distance
r_y	lateral reference distance
r_z	vertical reference distance
t	time (usually travel time or assessment time)
t^*	time of transition
t_1	time in seconds after launch that precipitation begins
t_p	time at which peak concentration is calculated
$\overline{u}_k$	mean wind speed in k^{th} layer
u_{kT}	wind speed at top boundary of k^{th} layer
v_k	lateral component of wind in k^{th} layer
w_i $(i = 1,4)$	parameter used in formulation of vertical term
(X_G, Y_G, Z_G)	coordinates for a point in grid system
(X, Y, Z)	coordinates of a point in meteorological system
(x_i, y_i, z_i)	coordinates of receptor in L^{th} layer
$\overline{x}$	alongwind distance from cloud center to assessment point
x_x	alongwind virtual distance
x_y	lateral virtual distance
x_z	vertical virtual distance
(x_{rk}, y_{rk}, z_{rk})	grid system coordinates of vehicles entry point for the k^{th} layer

Symbol	Definition
x_k^*	alongwind travel distance from entry point to transition point
x_{sk}	eastward coordinate of cloud center at transition time t*
y_{sk}	northward coordinates of cloud center at transition time t*
z_{kT}	grid system coordinate of top boundary of the k^{th} layer
$\bar{z}_l$	a mean height within a specified layer
z_{kB}	grid system coordinate of bottom boundary of the k^{th} layer
z_{BL}, z_{TL}	vertical coordinate of bottom and top boundaries in L^{th} layer
α	tangent of elevation angle of trajectory within a layer; along wind power law exponent
β	lateral power law exponent
γ_0	decay coefficient
γ	vertical power law exponent
γ_w	washout coefficient
$\Delta\ell$	length of the trajectory within a specified layer
η	trajectory slope in along wind direction
$\overline{\theta_k}$	mean wind direction in k^{th} layer
θ_{KT}	wind direction at top boundary of k^{th} layer
θ_{BT}	wind direction at bottom boundary of k^{th} layer
$\bar{\theta}_L$	mean wind direction in the L^{th} layer

Symbol	Definition
θ_{nm}	moment of concentration at height z
Θ_{nm}	moment of concentration for the diffusing layer
$\acute{\theta}_{oo}$	finite cosine transform of θ_{oo}
π	pi = 3.14159...
σ_x	standard deviation of cloud in alongwind direction
σ_y	standard deviation of cloud in lateral direction
σ_z	standard deviation of cloud in vertical direction
σ_{xs}	initial standard deviation of cloud in alongwind direction
σ_{ys}	initial standard deviation of cloud in lateral direction
σ_{zs}	initial standard deviation of cloud in vertical direction
σ_{xr}	along wind diffusion parameter
σ_{yr}	lateral diffusion parameter
σ_{zr}	vertical diffusion parameter
σ_{xL}^2	alongwind variance of cloud with respect to the L coordinate system at time t*
σ_{yL}^2	lateral variance of cloud with respect to the L coordinate system at time t*
σ_{zL}^2	vertical variance of cloud with respect to the L coordinate system at time t*
$p\sigma_x^2$	variance of a point source in alongwind direction
τ	slope of trajectory in lateral direction
χ	concentration
$\hat{\chi}$	expected concentration with decay and washou
χ_{AT}	total concentration for abort
χ_L	concentration for line source

Symbol	Definition
χ_p	concentration for point source
ψ	parameter used in line integration to find concentration
$\sim$	indicates asymptotic approximation
>>	much greater than

1.0 INTRODUCTION

This report presents the results of a study by GEOMET, Incorporated, for the George C. Marshall Space Flight Center (MSFC) during the period 1 June 1969 through 31 May 1970, in compliance with Contract NAS8-24438 entitled, "Exhaust Cloud Growth and Debris Fallout Phenomena."

The work was carried out in the form of two separate and independent tasks as indicated in the contract title; the first task (described in Section 2.0) involved the analysis of films of the exhaust clouds from static rocket engine test firings at MSFC and the use of these data in theoretical and statistical investigations to study the rise and growth of such clouds. The second task (described in Section 3.0) consisted of the development of a predictive model to describe the diffusion and fallout of debris from rocket engine exhausts in launches from the Kennedy Space Flight Center (KSC) launch area. The background and objectives for each of these two major tasks are discussed in their respective sections (2.0 and 3.0).

2.0 TASK I - EXHAUST CLOUD RISE AND GROWTH

Most of the recent research programs dealing with air pollution place their emphasis on the time variation of air pollution because of the increasing amounts of foreign materials being introduced into the air from such sources as automobiles, factories, open fires, explosions, etc. While investigations have been conducted on the nature of buoyant clouds, most of this research is based on either small-scale or large-scale clouds as generated from smoke stacks or atomic explosions. Of considerable interest to NASA's vehicle program, is the type of clouds generated by large space vehicle engines. The information required is, for example, how fast do such clouds rise? what is their volumetric growth rate? what is the maximum height to which they ascend until they become environmentally stable? and where and how is the cloud transported and diffused until the particulates settle to the surface?

NASA is concerned with this problem because of results from investigations of solid and liquid propellants. It is known that exhausts from some types of fuels can be pungent to smell or somewhat toxic if inhaled. Use of such fuels would require close monitorship of atmospheric conditions and the utilization of atmospheric diffusion expressions to determine the expected transport, dispersion, and deposition of such fuel by-products. Past work done by NASA on the problem of atmospheric diffusion, while limited, has resulted in contributions made by the various NASA centers (in-house and by contractual efforts).

The objective of this task is to study the vehicle engine exhaust cloud rise and growth rate phenomena. Information is also desired on the maximum height to which these clouds rise before they become environmentally stable. Movie films of static vehicle engine tests conducted at MSFC were made available for extraction of data, plus photographs of vehicle exhausts taken during launches. Local atmospheric data were made available as observed during the static firings; however, synoptic weather phenomena were also available to be related to cloud rise and growth behavior during the periods in question.

The following sections describe the treatment of the film data, including the development of the theory and statistical analysis of the data.

2.1 Analyses of Film Records of Static Firings of Rocket Engines

A major part of the contract entitled "Exhaust Cloud Growth and Debris Fallout Phenomena" is concerned with the analyses of MSFC film data. The following discussion will trace the development of these data from receipt of all films from MSFC to their ultimate preparation for use in theoretical model validation (Section 2.2) and statistical interpretation (Section 2.3). The discussion is divided into the following phases:

- reasons for selection or rejection of cases and synopsis of the method used to reduce the raw data (2.1.1);
- statistical comparisons of independent readings of the data (2.1.2); and
- synopsis and verification of the atmospheric drift correction technique (2.1.3).

The films studied represent twenty cases from some forty records originally provided by MSFC of static firings during 1964 and 1965. An early screening process focused attention on the twenty cases described in the following sections. These were single camera records taken from a distance of about 4000 meters from the static firing test stand and accompanied by meteorological and engine data records.

2.1.1 Reasons for Selection or Rejection of Each Case

Of the forty cases of MFSC Film Data originally sent to GEOMET, Incorporated, as a basis for an empirical approach to cloud rise prediction and to give meaningful input parameters for a theoretical model, as well as statistical analyses, twenty were selected for detailed study. From these, ten cases were ultimately selected for analysis. The ten that were not selected were eliminated for one or more of the following reasons: the film record began after the initiation of firing; there was no reference point in the film for measurement purposes; no data on the engine firing were available; and the film record was too short. Table 2-1 lists all available cases with the reasons for the selection or rejection of each.

After selection of the useful cases, the data were processed. Since it was evident that the MSFC film data provided a keystone upon which the empirical approach to cloud rise prediction would depend, the following steps were taken to ensure its accuracy:

- a Vanguard Motion Analyzer was used to increase the accuracy in the readings of the film;
- two independent readings were taken of each case;
- statistical techniques were used to test each set of film readings for errors (2.1.2); and
- wind data and information on the "jet phase" (see 2.1.3) were used to develop correction procedures.

The film analyses consisted of measuring sequenced frames using the Vanguard Motion Analyzer. The cloud picture was divided into six horizontal segments consisting of a triangle at both the top and the bottom and four trapezoids in between (see Fig. 2-1). From this, there was available from each frame a total of twelve points with coordinates (X,Z). The records of the location of the points were punched on IBM cards and converted to the metric system.

Table 2-1 Summary of available films with quality and reasons for acceptance or rejection

Case	Quality	Accept or Reject?
TWF050	No reference point at start, camera position doubtful. Time t_0^* is not identified	reject
SIC06	Good reference and data	accept
SIC04	No reference point at start	reject
SA26	No reference point at start	reject
TWF032	Record begins after t_0	reject
TWF033	Good reference and data	accept
SIC05	Good reference and data	accept
TWF052	No reference point at start	reject
TWF023	Record begins after t_0, too brief to be of use	reject
TWF025	Record begins after t_0, too brief to be of use	reject
TWF026	Good reference and data	accept
TWF027	Good reference and data	accept
TWF028	Film of very poor quality, record begins after t_0	reject
TWF031	Good reference and data	accept
SA25	Record begins after t_0, too brief to be of use	reject
TWF057	Camera position doubtful	reject
TWF056	Good reference and data	accept
TWF037	Good reference and data	accept
TWF034	Good reference and data	accept
No. 23	Good reference and data	accept

*Time when a test firing first commences.

To convert the data, a reference height for each case was established. That reference was taken as the height of a tower that was in the plane of the launch. Figure 2-1 is a schematic diagram of the cloud after firing and the method of measurement. The time when firing commenced was designated as t_0. At that time, coordinates were taken of the initial firing point

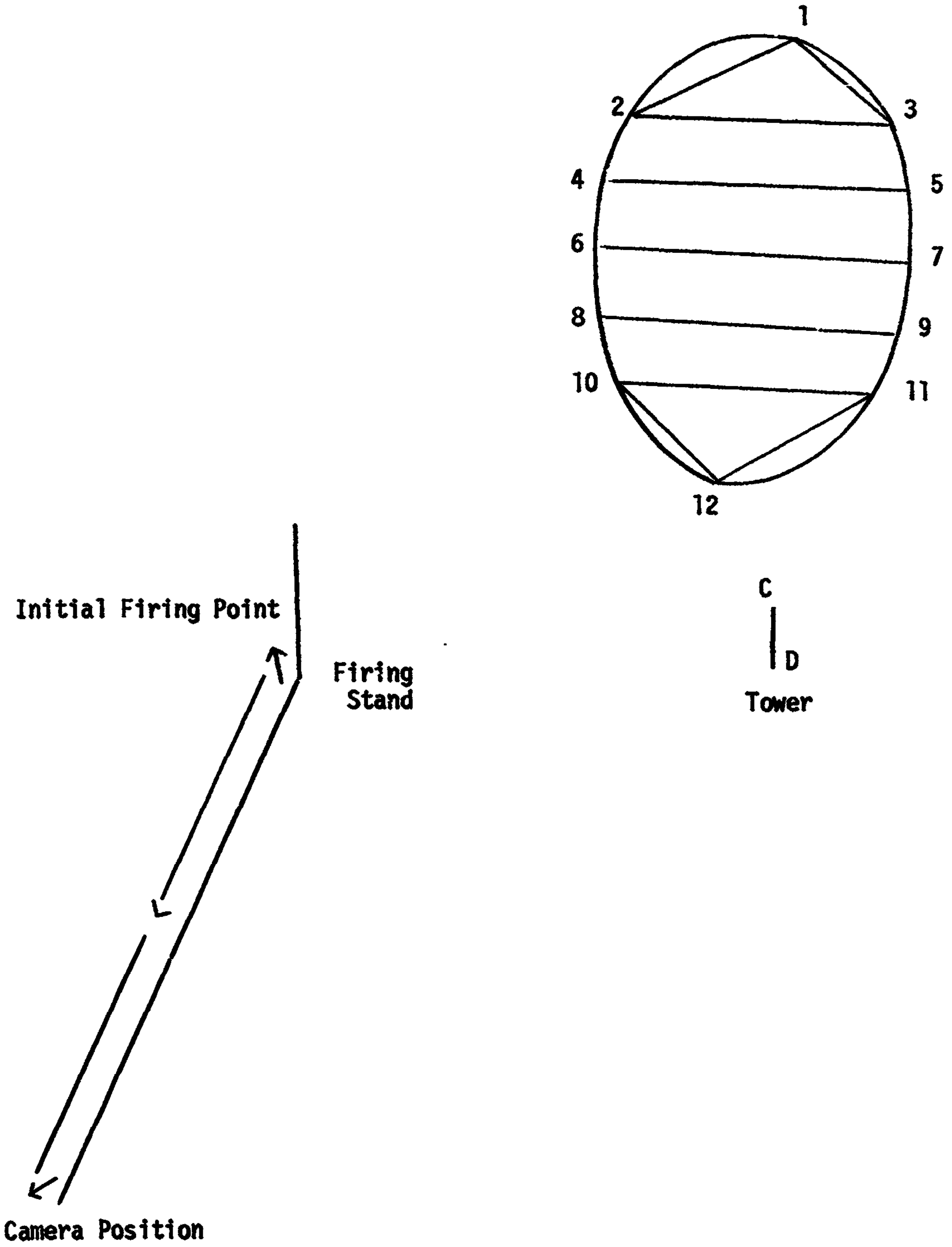

L = Distance in Meters From Camera Position to Firing Point.

Figure 2-1 The cloud after firing showing the method of measurement together with the tower coordinates. For selected times thereafter, coordinates of all points on the cloud shown in Fig. 2-1 were recorded in terms of frame number for conversion of time and inches on the viewing screen for conversion of distance. The measured coordinates were converted to the real dimensions in the metric system using the following relationships:

Vertical Coordinate:

$$z \text{ (meters)} = \frac{Z_A - Z_F}{H_A} \times H \qquad (2\text{-}1)$$

Horizontal Coordinate:

$$x \text{ (meters)} = \frac{X_A - X_F}{H_A} \times H \ . \qquad (2\text{-}2)$$

The frame number was converted to time in records using the fact that 24 frames per second were recorded. That relationship is:

$$t \text{ (seconds)} = (N - N_i)/24 \qquad (2\text{-}3)$$

where

N = frame number

N_i = initial frame number at time t_o

H = actual height of tower, CD, meters

H_A = height of tower, CD, as measured by the analyzer, inches

X_A = coordinate of X as measured by the analyzer, inches

X_F = coordinate of the initial firing point (X) as measured by the analyzer, inches

Z_A = coordinate of Z as measured by the analyzer, inches

Z_F = coordinate of the initial firing point (Z) as measured by the analyzer, inches.

The following paragraph explains the use of the preceding method.

Table 2-2 is a sample of output from Case TWF 037. The initial coordinates of the firing point are $Z_F = 2.195$ and $X_F = 2.815$ and the measured height of tower CD is 2.454 - 2.168 or 0.288. The initial frame number is 7650. Using (2-1) and (2-2) for point 1, we obtain $Z_A = 126.54$ meters and $X_A = 179.82$ meters. Using (2-3), the corresponding time for the frame is 7 seconds. The same procedure is followed for all other points and all time steps.

Table 2-2 **Sample of data taken from case TWF 037**

Frame Number	X Coordinate Lowest Point (B)	Y Coordinate Lowest Point (B)	X Coordinate Highest Point (A)	Y Coordinate Highest Point (A)	X Coordinate at Point		Y Coordinate at Point	
7818	2.815	2.195	3.299	2.522	1	3.195	1	2.468
					2	3.432	2	2.468
					3	3.124	3	2.413
					4	3.447	4	2.413
					5	3.077	5	2.358
					6	3.472	6	2.358
					7	3.014	7	2.303
					8	3.419	8	2.303
					9	2.953	9	2.248
					10	3.264	10	2.248

2.1.2 Statistical Comparisons of Independent Readings of the Data

In order to ensure the highest degree of accuracy possible in the readings, each film was read independently by two different analysts.* This provided the basic input for the statistical error analyses program described in this section. In essence, this program compared the replicate readings of a point and calculated the root mean square error for each set of films. These results were utilized both to minimize typographical errors in the data cards and to obtain an estimate of the uncertainty of the measurements for each film set.

After the raw film data had been reduced, the two independent readings for each case were compared. At every coordinate for each time step, the following were obtained: the difference between measured values; the mean of the differences; the mean of the absolute value of the differences; and the root mean square error of the differences. The root mean square error is defined as the square root of the sum of the squares of the difference between measured values divided by the total number of readings, i.e.,

$$(\mathrm{RMSE})_j = \left\{ \frac{\sum_{i=1}^{N} \left\{ R_{A_{ij}} - R_{B_{ij}} \right\}^2}{N} \right\}^{1/2} \qquad (2\text{-}4)$$

---

* The problems related to the capability of a film record of the visible cloud to represent the real dimensions of the cloud have not been considered in this study. For these firings, the film record is the only set of data describing the cloud behavior and thus has been used "as is" for that purpose.

where

N = the number of frames analyzed

i = the frame number

j = index of point being subjected to error analysis (see Fig. 2-1)

$R_{S_{ij}}$ = reading of point j by reader S in the ith frame.

Referring to Fig. 2-1, nineteen separate comparisons were run for each time increment. A check was made of all differences for all coordinates for each case. Where abnormally large differences were found, the original data were checked for punch errors and cards being out of sequence. By this method, typographical errors could be separated from the errors of measurement. Table 2-3 shows a typical comparison of the two readings for the Y-coordinate of the highest point of the cloud for Case TWF 037 after these typographical errors had been removed. What remains in each case is the random error associated with the actual reading. It is seen that the RMSE is about 12.6 meters, which is a typical value for all coordinates for this case. For other coordinates, this error ranged from 5 meters to 30 meters. Generally, the clearer the film, the lower was the error. The average among measured values was used as the actual coordinate value for each point. These values were used in the correction technique described in Section 2.1.3.

2.1.3 Correction Technique for Cloud Drift

2.1.3.1 General

After the raw data were converted from film to actual size measurements (2.1.1) and analyzed for errors (2.1.2), an allowance had to be made for any motion of the cloud toward or away from the camera caused by the initial jet effects and/or wind drift. The procedure for determining this

Table 2-3 Typical comparison of two readings for Y-coordinate for case TWF 037

Y-Coordinate of Highest Point of Cloud			
Time (sec)	1st Reader	2nd Reader	Difference
3.00	91.20	81.68	9.52
5.00	101.68	112.56	-10.88
7.00	126.91	143.04	-16.12
9.00	147.48	161.02	-13.54
11.00	174.65	187.99	-13.33
13.00	213.07	221.21	- 8.14
15.00	237.91	248.18	-10.27
17.00	265.85	278.67	-12.82
19.00	310.48	306.03	4.45
21.00	318.63	329.09	-10.46
25.00	371.81	370.52	1.29
29.00	411.78	407.65	4.13
33.00	428.08	442.82	-14.73
37.00	462.62	472.14	- 9.51
41.00	486.69	496.76	-10.07
45.00	526.66	521.38	5.28
49.00	541.41	548.74	- 7.33
53.00	563.53	580.01	-16.47
57.00	587.60	603.46	-15.85
61.00	626.41	633.95	- 7.54
65.00	643.10	657.40	-14.29
69.00	679.19	685.54	- 6.34
73.00	701.70	700.78	0.92
77.00	716.45	709.38	7.07
81.00	734.69	735.17	- 0.47
85.00	749.44	737.91	11.53
89.00	742.06	755.89	-13.82
93.00	797.95	789.89	8.06
97.00	803.39	784.81	18.57
101.00	798.34	829.37	-31.03
105.00	827.84	830.54	- 2.69
109.00	803.77	824.29	-20.52
113.00	816.58	838.75	-22.17

Mean of differences = -6.596

Mean of absolute value of differences = 10.888

Root mean square of differences = 12.671

Largest difference without regard to sign = -31.030

allowance is described as follows: The total test firing period was divided into two regions, one in which jet effects were dominant and one in which atmospheric effects were dominant. For each region, a correction was applied which was related to the amount of travel of the cloud toward or away from the camera. Appendix A describes the mathematical techniques involved for each of these correction techniques.

Application of these correction procedures requires knowledge of the transition height where jet effects become negligible. However, this is difficult to define from the films. The following material discusses this problem.

Two procedures, one objective and the other subjective, were developed to locate this transition point (see Fig. 2-2).

2.1.3.2 Objective Technique for Determining Transition Height

This technique is based on the assumption that the first significant decrease in the magnitude of the vertical velocity of the cloud is due to the fact that a change in phase took place, i.e., jet effects became negligible. For each of the ten trials, the change in height of the topmost point of the cloud with time (dz/dt) was computed as a function of height. Table 2-4 shows dz/dt as both a function of time and height for a sample case, No. 23. Note was made of the height at which dz/dt first began to decrease (time - 7 sec.). The level previous to that where dz/dt began to increase again (time - 9 sec.) was selected as the transition height (time - 7 sec.). The height is 172 meters.

2.1.3.3 Subjective Technique for Determining Transition Height

This technique is based on the assumption that the region in which the phase 1 influence ends will be identifiable in the film record as a significant deviation of the cloud's direction of travel from the jet axis.

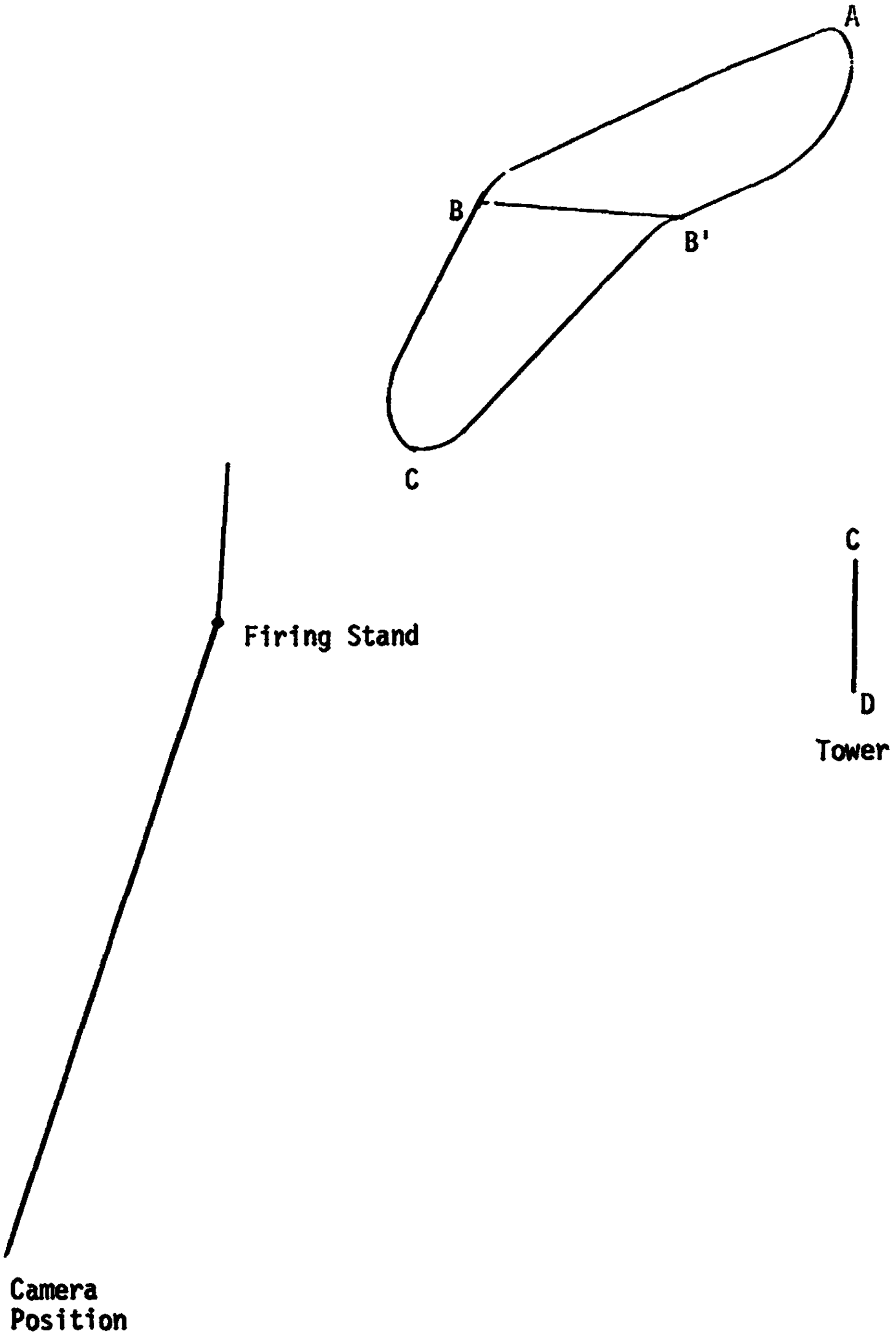

Figure 2- 2 Location of transition height where jet effects become negligible. Line BB' is at this height.

Table 2-4 Change in topmost point of cloud with time as a function of time and height for case No. 23

Time (sec)	dz/dt (m sec^{-1})	z (meters)
3	12.6	108
5	19.4	133
7	10.0	172
9	13.4	192
11	23.7	219
13	17.6	266
15	15.2	302
17	16.8	332
19	20.8	366
21	16.2	407
25	14.7	472
29	12.3	531
33	9.4	581
37	4.8	619
41	10.1	638
45	10.1	679
49	7.8	719
53	8.7	751

For each of the ten trials, the cloud was observed for several seconds during which the rocket was firing. The height coordinate was recorded where the cloud appeared to deviate from the jet axis. In Fig. 2-2 this height is given by the line BB'. Two independent readings of this level were taken. As might be expected, the two readings tended to vary, but their average differences were on the order of 25 meters.

2.1.3.4 Comparison of the Objective and Subjective Techniques

Table 2-5 is a comparison between both techniques. In addition, both readings using the subjective procedure were compared. It is seen that the two subjective readings tended to be comparable, and the objective method compared favorably to the subjective one, with their standard deviations also comparable.

Table 2-5 Transition heights as computed by the objective and subjective techniques

Case	Subjective Technique		Objective Technique
	1st Reader	2nd Reader	
TWF037	223	197	134
TWF034	174	155	148
TWF031	136	145	293
TWF026	166	146	196
TWF027	176	176	204
TWF033	185	132	118
TWF056	151	202	217
SIC05	154	99	197
SIC06	145	73	220
No. 23	99	34	172
Mean	160.9	135.9	189.9
Standard Deviation	31.1	50.9	47.8

2.1.4 Validation of the Correction Technique and Presentation of the Data for Use in Analyses

A technique was devised for verifying the validity of the correction methods employed. This technique is described in Appendix B and represents a combination of synthesizing a known cloud behavior and studying the goodness of applied corrections, plus detailed case studies of the actual ten test runs. The verification technique supports the correction of the data for atmospheric drift toward or away from the camera and was used to derive the final numbers characterizing cloud behavior for each test firing. Some of the finally derived data for all cases are presented in Tables 2-6a and 2-6b and cover the following: the dependent parameters of cloud height (z), rise rate ($\overline{dz/dt}$), area ($\overline{A}$), and the rate of increase of area ($\overline{dA/dt}$) for the jet phase (phase 1), the hot plume phase (phase 2), and the two phases combined; the engine parameters of fuel ratio (F), duration of firing (D), and thrust (TH); and the meteorological parameters of mean atmospheric temperature ($\overline{T}$), temperature change with height (dT/dZ), mean wind speed ($\overline{u}$), wind speed change with height (du/dZ), mean atmospheric pressure ($\overline{p}$) and change with height (dp/dz), mean relative humidity ($\overline{RH}$), and mean atmospheric density ($\overline{\rho}$). The data on observed cloud height (z) and area (A) as a function of time after firing for all cases, however, are tabulated in Appendix C. Also included in Appendix C are observed temperature (T), pressure (p), relative humidity (RH), wind direction (d), and wind speed (u) at levels from the surface to 2000 meters for all cases.

These data were the principal source of information for the validation studies of the theoretical development (Section 2.2) and for the multivariate statistical analyses (Section 2.3).

Table 2-6a Dependent and independent parameter* values employed in the analyses of Section 2.2 and 2.3

	Dependent Cloud Parameters				Independent Engine Parameters		
Trial	z	$\overline{dz/dt}$	$\overline{A}$	$\overline{dA/dt}$	F	D	TH
Phase 1							
TWF034	151.0	21.5	7157.0	2045.0	1.65	24.0	1,504,000
TWF033	119.0	23.8	4269.0	1707.0	1.47	66.0	1,504,000
TWF031	303.0	23.3	16510.0	1270.0	1.50	20.0	1,504,000
TWF056	222.0	24.8	10436.0	2319.0	2.42	40.0	1,504,000
TWF037	137.0	19.5	8120.0	2320.0	1.41	119.0	1,504,000
TWF027	210.0	23.3	13265.0	2948.0	1.57	50.0	1,504,000
TWF026	201.0	22.3	10022.0	2227.0	1.42	23.0	1,504,000
NO 23	171.0	24.4	8261.0	2370.0	17.50	35.0	1,600,000
SICO5	198.0	39.6	20266.0	8106.0	1.89	15.0	7,500,000
SICO6	222.0	44.5	20026.0	8010.0	1.38	40.0	7,500,000
Phase 2							
TWF034	670.0	6.4	83362.0	1534.0	1.65	24.0	1,504,000
TWF033	617.0	14.0	79624.0	3003.0	1.47	66.0	1,504,000
TWF031	284.0	11.8	52150.0	1594.0	1.50	20.0	1,504,000
TWF056	817.0	17.0	132036.0	4631.0	2.42	40.0	1,504,000
TWF037	789.0	7.4	180775.0	3104.0	1.41	119.0	1,504,000
TWF027	890.0	13.9	162740.0	4256.0	1.57	50.0	1,504,000
TWF026	597.0	11.9	84117.0	2414.0	1.42	23.0	1,504,000
NO 23	601.0	12.0	78731.0	2488.0	17.50	35.0	1,600,000
SICO5	1056.0	33.0	210916.0	10338.0	1.89	15.0	7,500,000
SICO6	883.0	27.8	235701.0	12228.0	1.38	40.0	7,500,000
1 plus 2							
TWF034	821.0	8.4	76205.0	1571.0	1.65	24.0	1,504,000
TWF033	736.0	15.0	78355.0	3311.0	1.47	66.0	1,504,000
TWF031	587.0	15.8	35640.0	1926.0	1.50	20.0	1,504,000
TWF056	1039.0	18 2	121600.0	4266.0	2.42	40.0	1,504,000
TWF037	926.0	8.2	172650.0	3055.0	1.41	119.0	1,504,000
TWF027	1100.0	15.1	149475.0	4095.0	1.57	50.0	1,504,000
TWF026	798.0	14.0	74095.0	2429.0	1.42	23.0	1,504,000
NO 23	772.0	13.5	70470.0	2818.0	17.50	35.0	1,600,000
SICO5	1254.0	33.8	190650.0	10305.0	1.89	15.0	7,500,000
SICO6	1105.0	29.8	215678.0	11117.0	1.38	40.0	7,500,000

*See text for parameter definitions and units

Continued

Table 2-6b Dependent and independent parameter* values employed in the analyses of Section 2.2 and 2.3 - Concluded

	Dependent Cloud Parameters				Independent Meteorological Parameters							
Trial	z	$\overline{dz/dt}$	$\overline{A}$	$\overline{dA/dt}$	$\overline{T}$	dT/dz	$\overline{u}$	du/dz	$\overline{P}$	dp/dz	$\overline{RH}$	[illegible]
Phase 1												
TWF034	151.0	21.5	7157.0	2045.0	288.6	-0.0110	3.9	0.0170	996.5	-0.1170	41.3	3.45
TWF033	119.0	23.8	4269.0	1707.0	295.6	-0.0010	4.7	0.0120	994.9	-0.1140	90.0	3.36
TWF031	303.0	23.3	16510.0	1270.0	304.3	-0.01366	4.3	0.00466	987.1	-0.1093	56.6	3.24
TWF056	222.0	24.8	10436.0	2319.0	303.1	-0.01400	5.1	0.00550	985.1	-0.1110	38.4	3.25
TWF037	137.0	19.5	8120.0	2320.0	288.2	-0.0030	4.7	0.0320	1001.6	-0.1180	37.3	3.47
TWF027	210.0	23.3	13265.0	2948.0	301.2	-0.010	5.0	-0.007	985.4	-0.1110	40.7	3.27
TWF026	201.0	22.3	10022.0	2227.0	301.0	-0.0025	5.7	0.0360	983.5	-0.1105	71.0	3.23
NO 23	171.0	24.4	8261.0	2370.0	294.3	-0.00150	4.9	0.028	989.7	0.1145	30.1	3.35
SIC05	198.0	39.6	20266.0	8106.0	300.2	-0.0150	4.7	0.0125	990.8	-0.1120	45.5	3.30
SIC06	222.0	44.5	20026.0	8010.0	299.6	-0.00650	3.1	0.0035	990.4	-0.1110	53 [illegible]	3.30
Phase 2												
TWF034	670.0	6.4	83362.0	1534.0	284.9	-0.00885	5.7	0.00271	950.9	-0.1278	47.5	3.33
TWF033	617.0	14.0	79624.0	3003.0	294.9	-0.00216	4.1	0.0266	956.3	-0.1096	77.8	3.24
TWF031	284.0	11.8	52150.0	1594.0	300.9	-0.090	4.9	0.0030	945.5	-0.1063	56.6	3.14
TWF056	817.0	17.0	132036.0	4631.0	297.5	-0.0104	6.9	0.003	937.2	-0.1057	43.3	[illegible]
TWF037	789.0	7.4	180775.0	3104.0	285.2	-0.00828	7.7	0.00387	960.3	-0.1165	30.4	3.33
TWF027	890.0	13.9	162740.0	4256.0	296.9	-0.00825	4.8	0.00125	931.7	-0.1065	51.9	3.13
TWF026	597.0	11.9	84117.0	2414.0	298.5	-0.0075	8.1	0.00125	940.5	-0.1065	67.0	3.15
NO 23	601.0	12.0	78731.0	2438.0	291.8	-0.00966	7.8	0.00033	945.2	0.1101	26.1	3.23
SIC05	1056.0	33.0	210916.0	10338.0	293.7	-0.00937	8.1	0.00718	923.7	-0.1067	62.8	3.14
SIC06	883.0	27.8	235701.0	12228.0	295.0	-0.00887	5.3	0.00637	936.2	-0.1076	65.6	3.17
1 plus 2												
TWF034	821.0	8.4	76205.0	1571.0	285.4	-0.00912	5.4	0.0045	956.8	0.1140	49.2	3.35
TWF033	736.0	15.0	78355.0	3311.0	295.0	-0.00233	3.5	0.004	962.0	-0.1102	81.8	3.26
TWF031	587.0	15.8	35640.0	1926.0	302.9	-0.02256	4.2	0.00383	962.0	-0.1078	60.0	3.17
TWF056	1039.0	18.2	121600.0	4266.0	298.9	-0.00171	6.3	0.0035	938.3	-0.1063	52.9	3.13
TWF037	926.0	8.2	172650.0	3055.0	285.3	-0.00871	6.1	0.007	956.2	-0.1029	35.1	3.35
TWF027	1100.0	15.1	149475.0	4095.0	297.9	-0.0085	5.5	-0.005	942.8	-0.1074	56.1	3.16
TWF026	798.0	14.0	74095.0	2429.0	298.8	-0.00625	4.4	-0.00575	951.6	-0.1075	71.0	3.18
NO 23	772.0	13.5	70470.0	2818.0	291.9	-0.01016	5.0	0.00725	956.7	0.1112	30.9	3.27
SIC05	1254.0	33.8	190650.0	10305.0	295.2	-0.01236	6.9	0.0087	934.9	-0.1073	53.3	3.15
SIC06	1105.0	29.8	215678.0	11117.0	296.1	-0.01025	3.2	0.004	947.3	-0.1083	61.5	3.19

*See text for parameter definitions and units.

2.2 Theoretical Study

2.2.1 General Background

Numerous theories on the rise of a heated buoyant cloud have been reported in the literature. However, few attempts have been made to apply these theories to an exhaust cloud produced from static vehicle engine firing. Recently, Hage and Bowne (1965) computed the maximum height attained by such a cloud using equations developed by Machta (1950), Sutton (1950), and Morton, Taylor and Turner (1956). However, no features of exhaust cloud rise phenomena, other than maximum height, were examined in their study.

In this investigation, a physical-numerical model has been developed following a theory of the bent-over plume of heated gas from a continuous source developed by Priestley (1956). In addition to the maximum height of cloud rise, this model predicts other features of exhaust cloud rise and growth such as instantaneous height, rise rate, growth rate, and temperature excess of the cloud. Furthermore, environmental factors such as wind and thermal stability, that are often neglected in models of this type, have been taken into account in this model. All these refinements make this a very useful and general model which may be applied not only to exhaust clouds produced from static engine firing, but also to other types of buoyant clouds from a heated source.

2.2.2 A Physical-Numerical Model for Exhaust Cloud Rise and Growth

Based on the formal analyses given by Rouse, Yih and Humphreys (1952), Priestley (1953, 1956), Priestley and Ball (1955), and Morton

Taylor and Turner (1956), a physical-numerical model for exhaust cloud rise and growth was derived. The model was designed to yield the following informaton on exhaust cloud behavior: (1) the maximum height to which the cloud ascents before it becomes environmentally stable, (2) the height of the cloud as a function of time after its formation, (3) the rise rate or the vertical velocity of the cloud as a function of height or time after its formation, (4) the temperature of the cloud as a function of height or time after its formation, and (5) the growth rate of the cloud.

The ascent, spreading, and diffusion of the exhaust cloud were regarded as subject to three phases (Priestly 1965). The first phase being the jet phase, during which the exhaust cloud moves through the resisting air and is subjected to turbulence induced by its own motion. In the second phase, the jet-induced motion decreases in intensity and the atmospheric turbulence becomes dominant. The mixing of exhaust gas with ambient air at this point proceeds at a rate determined by atmospheric properties. The maximum height to which the cloud ascends until it becomes environmentally stable is reached during this phase. The third and final phase begins after the cloud has lost its effective independent motion and buoyancy and the stage is set for pure atmospheric diffusion. Since our objective for Task I is to study cloud rise and growth, only the first two phases will be simulated in the model.

2.2.2.1 Model Equations

2.2.2.1.1 Equations for the First Phase of Cloud Rise and Growth

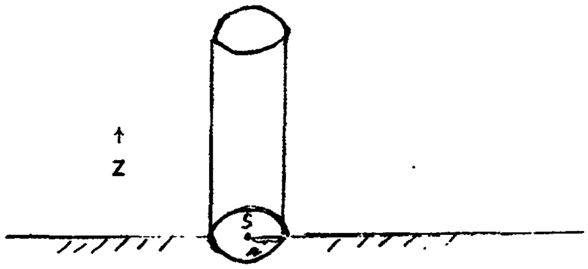

Figure 2-3 Schematic sketch of a circular-symmetric cloud column

The derivation of model equations begins with a very general system of a circular-symmetric cloud column as sketched in Fig. 2-3. In Fig. 2-3, S is the source point, r is the radius of the ring, and z is the vertical coordinate. The basic equations governing the first phase of the rise and growth of the exhaust cloud is the equation of continuity,

$$\frac{\partial}{\partial z}(rw\rho) + \frac{\partial}{\partial r}(ru\rho) = 0, \tag{2-5}$$

the equation of vertical motion,

$$\frac{\partial}{\partial z}(rw^2\rho) + \frac{\partial}{\partial r}(ruw\rho) = r\frac{\theta'}{\theta_e}\rho g + \frac{\partial}{\partial r}(\tau r), \tag{2-6}$$

and the equation of heat conservation

$$\frac{\partial}{\partial z}(rw\theta\rho) + \frac{\partial}{\partial r}(ru\theta\rho) = -\frac{1}{c_p}\frac{\partial}{\partial r}(rF), \tag{2-7}$$

where

r = the radius of the circular-symmetric cloud,
z = the height above the source of the cloud,
w = the vertical velocity of the cloud (dz/dt),
ρ = density of exhaust gas in the cloud,
u = radial velocity of the exhaust cloud,
θ = potential temperature in the cloud,
θ_e = potential temperature outside the cloud,
θ' = excess potential temperature of the cloud ($\theta-\theta_e$),
τ = vertical turbulent shearing stress,
g = acceleration due to gravity,
c_p = specific heat of air at constant pressure,
F = radial turbulent heat flux.

All quantities in Equations (2-5) through (2-7) refer to mean values for the ring-shaped cloud surface. It is assumed that the ambient pressure is undisturbed, that the vertical turbulent mixing is negligible compared with the horizontal, and that the density is constant except insofar as it affects the buoyancy.

From Equations (2-5) and (2-6) may be derived the kinetic energy equation

$$\frac{\partial}{\partial z}\left(\frac{1}{2} r w^3 \rho\right) + \frac{\partial}{\partial r}\left(\frac{1}{2} r u w^2 \rho\right) = r w \frac{\theta'}{\theta_e} \rho g + w \frac{\partial}{\partial r}(\tau r) \quad (2\text{-}8)$$

and from Equations (2-5) and (2-7) we have the following equation:

$$\frac{\partial}{\partial z}(r w \theta' \rho) + \frac{\partial}{\partial r}(r u \theta' \rho) = -\frac{1}{c_p}\frac{\partial}{\partial r}(rF) - r w \rho \frac{\partial \theta_e}{\partial z}. \quad (2\text{-}9)$$

Integration of Equation (2-6) from $r = 0$ to $r = \infty$ gives

$$\frac{d}{dz}\int_0^\infty rw^2\rho dr = \int_0^\infty r\frac{\theta'}{\theta_e}\rho gdr \qquad (2\text{-}10)$$

where $r\rho u$ is assumed to remain finite as r approaches ∞ and τr and w approach zero at $r = \infty$. Integration of Equations (2-8) and (2-9) for the same limits yields

$$\frac{d}{dz}\int_0^\infty \frac{1}{2}rw^3\rho dr = \int_0^\infty rw\frac{\theta'}{\theta_e}\rho gdr - \int_0^\infty \tau r\frac{\partial w}{\partial r}dr \qquad (2\text{-}11)$$

$$\frac{d}{dz}\int_0^\infty rw\theta'\rho dr = -\int_0^\infty \rho rw\frac{\partial\theta_e}{\partial z}\ dr \qquad (2\text{-}12)$$

where, again, $r\rho u$ remains finite and rF, τr, w and θ' all approach zero at $r = \infty$.

Both Priestley and Ball (1955) and Morton, Taylor and Turner (1956) assumed that the lateral profiles of w and θ' are of similar shape at different distances from the source. Following Sutton (1950) and citing results from laboratory experiments by Rouse, Yih and Humphreys (1952) and by Railston (1954), Priestley and Ball assumed that the profiles are Gaussian and the measures of dispersion are approximately the same for w and θ. Written in mathematical terms we have

$$\frac{w}{w_0} = \exp\left(-\frac{r^2}{2R^2}\right) \qquad (2\text{-}13)$$

$$\frac{\theta'}{\theta'_0} = \exp\left(-\frac{r^2}{2R^2}\right) \qquad (2\text{-}14)$$

where w_0, θ'_0 are values of w and θ' on the axis of the cloud and R is some linear characteristic of its lateral extent. Different assumptions were made by different investigators of the rate of entrainment. Morton, Taylor and Turner (1956) argued that the rate should be proportional to the ascending velocity and to the surface area of the cloud element, while Priestley and Ball assumed that the cloud experiences a vertical drag proportional to the square of the ascending velocity. The latter assumption was expressed as

$$\frac{\tau}{\frac{1}{2}\rho w_o^2} = f\left(\frac{r}{R}\right) \qquad (2\text{-}15)$$

where the function f is yet to be defined.

With the relationships expressed in Equations (2-13), (2-14) and (2-15), we can now integrate Equations (2-10), (2-11) and (2-12) to obtain

$$\frac{d}{dz}\left(R^2 w^2\right) = 2R^2 \frac{\theta'}{\theta_e} g \qquad (2\text{-}16)$$

$$\frac{d}{dz}\left(R^2 w^3\right) = 3R^2 w \frac{\theta'}{\theta_e} g - cRw^3 \qquad (2\text{-}17)$$

$$\frac{d}{dz}\left(R^2 w \theta'\right) = -\, 2R^2 w \frac{\partial \theta_e}{\partial z} \qquad (2\text{-}18)$$

where c is a profile constant and the subscript o has been dropped. The combination of Equations (2-16) and (2-17) yields the following:

$$\frac{dR}{dz} = c$$

$$\text{or } R = cz + \text{constant.} \qquad (2\text{-}19)$$

The constant c may be regarded as a spreading coefficient.

Priestley (1956) argued that Equations (2-16) through (2-19) apply, not only to a circular-symmetric cloud column (under calm wind conditions) as sketched in Fig. 2-3, but also to a bent-over plume (under the influence of wind u) as in Fig. 2-4. He maintained that the relative motion between plume and air is the source of spreading during the first phase, and that the only modification necessary when applying the system of equations to a plume in a crosswind of speed u, is to make c, the spreading coefficient variable, as a function of u. He further suggested that c is proportional to the square root of wind speed u, but has a value of 0.1 under calm conditions. For details of Priestley's argument, the readers are referred to Priestley's 1956 paper.

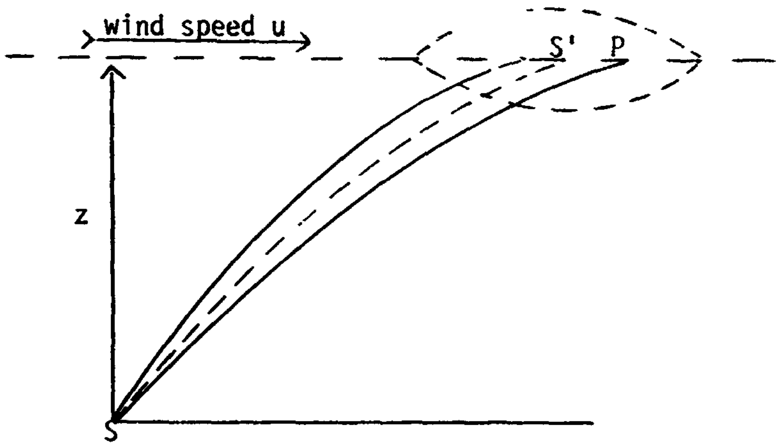

Figure 2-4 Schematic sketch of a plume in a crosswind of speed u. S is the source point, SS' is the center line of the plume, SO and SP are the boundaries of the plume.

Under neutral conditions ($\partial\theta_e/\partial z = 0$) the solution to Equations (2-16), (2-17) and (2-18) is given by (2-19) together with

$$w = \left[\frac{3Ag}{2\theta_e c^2}\left(\frac{1}{z} - \frac{z_0^2}{z^3}\right) + \frac{w_0^3 z_0^3}{z^3}\right]^{1/3} \quad (2\text{-}20)$$

$$\eta' = \frac{A}{c^2 z^2 w} \quad (2\text{-}21)$$

where

$A = Q/\pi\rho c_p$ (Q being the heat source strength),

z_o = the height at the source, and

w_o = vertical velocity at the source.

No general analytical solution has been found when the thermal stratification is not neutral ($\partial\theta_e/\partial z \neq 0$). However, the solution can be found numerically from the following equation (Priestley and Ball 1955).

$$(zw)^2 \frac{d}{dz}(zw) = \frac{gz}{\theta_e c^2}\left(A^2 - \frac{\theta_e}{g}\frac{\partial\theta_e}{\partial z} c^2 z^4 w^4\right)^{1/2} \qquad (2\text{-}22)$$

where all boundary conditions at $z = z_o$ are assumed to be known.

2.2.2.1.2 Equations for the Second Phase of Cloud Rise and Growth

The equations for the rise and growth of the exhaust cloud during the second phase are

$$\frac{dw}{dt} = \frac{g}{\theta_e}\theta' - kw \qquad (2\text{-}23)$$

$$\frac{d\theta'}{dt} = -k\theta' \qquad (2\text{-}24)$$

where the mixing rate k is a function of the effective radius of the cloud and the environmental eddy viscosity K.

The solution of Equations (2-23) and (2-24) for neutral stratification was given by Priestley (1956) as

$$w = \left(w_i + \frac{g\theta'_i}{\theta_e} t\right) e^{-kt} \qquad (2\text{-}25)$$

$$\theta' = (\theta'_i e^{-kt}) \qquad (2\text{-}26)$$

where the variables with subscript$_1$ are those valued at the transition from phase 1 to phase 2 and t is time from the transition. Equation (2-25) can be integrated to yield the height as a function of time and the maximum height the cloud will reach under neutral conditions as

$$z_m - z_1 = \frac{w_1}{k} + \frac{g\theta'_1}{k^2\theta_e} \tag{2-27}$$

where z_m is the maximum height and z_1 is the height reached at the transition. The maximum height for thermal stratifications other than neutral was given (Priestley 1953) as

$$z_m - z_1 = (kw_1 + \frac{g\theta'_1}{\theta_e})/(\frac{g}{\theta_e}\frac{\partial\theta_e}{\partial z} + k^2). \tag{2-28}$$

Note that when $\partial\theta_e/\partial z = 0$, Equation (2-28) becomes Equation (2-27).

2.2.2.1.3 The Transition from the First to the Second Phase

The transition from phase 1 to phase 2 was defined by Priestley (1956) as the point at which

$$(\frac{dw}{dz})_1 = (\frac{dw}{dz})_2 \tag{2-29}$$

with the transition height being z_1. When w_1 and w_2 are plotted as a function of z, z_1 can be easily located graphically.

Spurr (1957) showed that a cubic equation in z_1^2 can be derived to compute z_1:

$$\frac{1}{k^3 z_1^4}[\frac{3}{2}\frac{Ag}{\theta_e c^2} + \frac{1}{z_1^2}(w_o^3 z_o^3 - \frac{3}{2}\frac{Ag}{\theta_e c^2}z_o^2)] = 1. \tag{2-30}$$

2.2.2.2 The General Model Characteristics

The general characteristics of the model may be summarized as follows:

(1) The model formulations are general in nature, applying to all types of buoyant clouds or plumes from a continuous point source.

(2) The model takes atmospheric conditions such as wind, temperature and thermal stratification into account.

(3) Analytical solutions to model equations under neutral thermal stratification are available. When the thermal stratification is non-neutral, numerical methods are to be employed to obtain solutions.

(4) Linear spreading of the cloud with height (Equation (2-19)) during the first phase is a necessary property of the model. Growth of the cloud during the second phase is not treated in the present model formulations.

2.2.2.3 Computational Form of Model Equations

Most model equations are in algebraic form and of analytical nature and, therefore, are readily solvable. The only equation that has to be rewritten in finite-difference form and solved numerically is Equation (2-22), now becoming Equation (2-31):

$$w(j+1) = w(j) + \left[z(j+1) - z(j)\right] \left\{ \left[\frac{g}{\overline{\theta}_e c^2 \; z(j)^2 \; w(j)^2}\right] \left[A^2 - \frac{\overline{\theta}_e}{g} \frac{\overline{\partial \theta}_e}{\partial z} \overline{c}^4 \; z(j)^4 \; w(j)^4\right]^{1/2} - \frac{w(j)}{z(j)} \right\} \tag{2-31}$$

where j is the height index and $\overline{\theta}_e$, $\overline{c}$ and $\overline{\frac{\partial\theta_e}{\partial z}}$ are the properly averaged values of θ_e, c and $\frac{\partial\theta_e}{\partial z}$ respectively for the layer in which the first phase of cloud rise and growth takes place. The boundary condition is $w(o) = w_o$ at $z = z_o$. In the actual computations, a uniform vertical spacing, $z(j+1) - z(j)$, of 20 meters was used throughout the layer.

The only other equation which needs to be discussed is Equation (2-30), but for a different reason. It is recalled that Equation (2-30) is a cubic equation in z_1^2, for which an analytic solution of z_1 can be obtained only when the following conditions exist:

$$w_o^3 z_o^3 > \frac{3}{2} \frac{Ag}{\theta_e c^2} z_o^2 \tag{2-32}$$

$$\frac{\left[k^{-3}\left(w_o^3 z_o^3 - \frac{3}{2}\frac{Ag}{\theta_e c^2} z_o^2\right)\right]^2}{4} \geq \frac{\left[\frac{3}{2}\frac{Ag}{\theta_e c^2 k^3}\right]^3}{27} . \tag{2-33}$$

When either of the two conditions is violated, iterative methods will have to be used to obtain a solution numerically. Fortunately, for the ranges of numerical value of constants and variables in this study, the two conditions were always satisfied and an analytical solution to Equation (2-30) was available all the time. The method of solution to Equation (2-30) will be described in Appendix D.

2.2.3 Input Data and Auxiliary Equations

Input data used for model predictions of exhaust cloud rise and growth are tabulated in Table 2-7. Note that there are two types of input data: model input and raw input. Model input data are those derived from raw input data and used directly in the computations. For example, w_0 is a model input entity, which is derived from the raw input of V and α. However, model constants such as g, z and t in Table 2-7 are directly available and need no derivations.

Auxiliary equations were used to compute some model input from raw input quantities. For instance, the initial vertical velocity of the exhaust cloud was computed from the following equation:

$$w_0 = V \sin \alpha . \qquad (2\text{-}34)$$

A series of auxiliary equations were employed to arrive at the heat source parameter A:

$$\rho = \frac{pM_0}{R^* \, Tgas} \qquad (2\text{-}35)$$

$$Q = F^* \theta ' c_p \qquad (2\text{-}36)$$

$$A = \frac{Q}{\pi \rho c_p} . \qquad (2\text{-}37)$$

Diffusion parameter k was computed as a linear function of wind speed :

$$k = a_1 \bar{u} + a_2 . \qquad (2\text{-}38)$$

Based on Priestley's estimates (1956) a_1 and a_2 were set at 0.0204 and 0.004 respectively. $\bar{u}$ is an averaged value of all wind speeds observed in the layer where exhaust cloud rise and growth take place.

Table 2-7 Input data for model predictions of exhaust cloud rise and growth

	Model Input	Unit	Definition	Raw Input	Unit	Definition
Engine and exhaust gas data	w_o	cm sec^{-1}	initial vertical velocity of exhaust cloud	V	ft sec^{-1}	exit velocity of exhaust gas when the plume center impinges on the deflector
				α	degree	deflector angle
	z_o	cm	height of heat source	z*	cm	height of deflector
	A	cm^3°K sec^{-1}	heat source parameter	F*	lb min^{-1}	gas flow
				c_p	cal gm^{-1}°K^{-1}	specific heat of gas at constant pressure
				θ'	°K	potential temperature excess of exhaust gas
				p	lb/in^2	pressure of exhaust gas
				Tgas	°K	temperature of exhaust gas
				M_o	gm mol^{-1}	molecular weight of exhaust gas
				R*	erg mol^{-1}°K^{-1}	universal gas constant
Atmospheric Data	k	sec^{-1}	diffusion parameter	u(z)	m sec^{-1}	wind speed

Continued

Table 2-7 Input data for model predictions of exhaust cloud rise and growth - Concluded

	Model Input	Unit	Definition	Raw Input	Unit	Definition
	c	--	spreading coefficient	$R(z)$	cm	observed lateral extent of cloud
				z	cm	height of vertical grid point
	$\partial\theta_e/\partial z$	°K cm^{-1}	stability	$\theta_e(z)$	°K	ambient potential temperature
	$\theta_e(z)$	°K	ambient potential temperature	$\theta_e(z)$	°K	ambient potential temperature
Model constants	g	cm sec^{-2}	acceleration due to gravity			
	z	cm	height of vertical grid points			
	t	sec	time of computation in the second phase			

The spreading coefficient c was computed simply as an averaged value of the ratio of R(z)/z at all levels in the layer of interest. It could be a function of wind speed u, as suggested by Priestley (1956) and discussed in Section 2.2.2.1.1. Finally, the stability term was computed in the following way:

$$\frac{\partial\theta_e}{\partial z} = \frac{\theta_e(j+1) - \theta_e(j)}{z(j+1) - z(j)} \qquad (2\text{-}39)$$

where again j is the height index. In the actual computation an averaged value of $\partial\theta_e/\partial z$ for the layer of interest was used.

2.2.4 Computational Procedures

The procedures for model computations of exhaust cloud rise and growth are outlined in the following flow diagram.

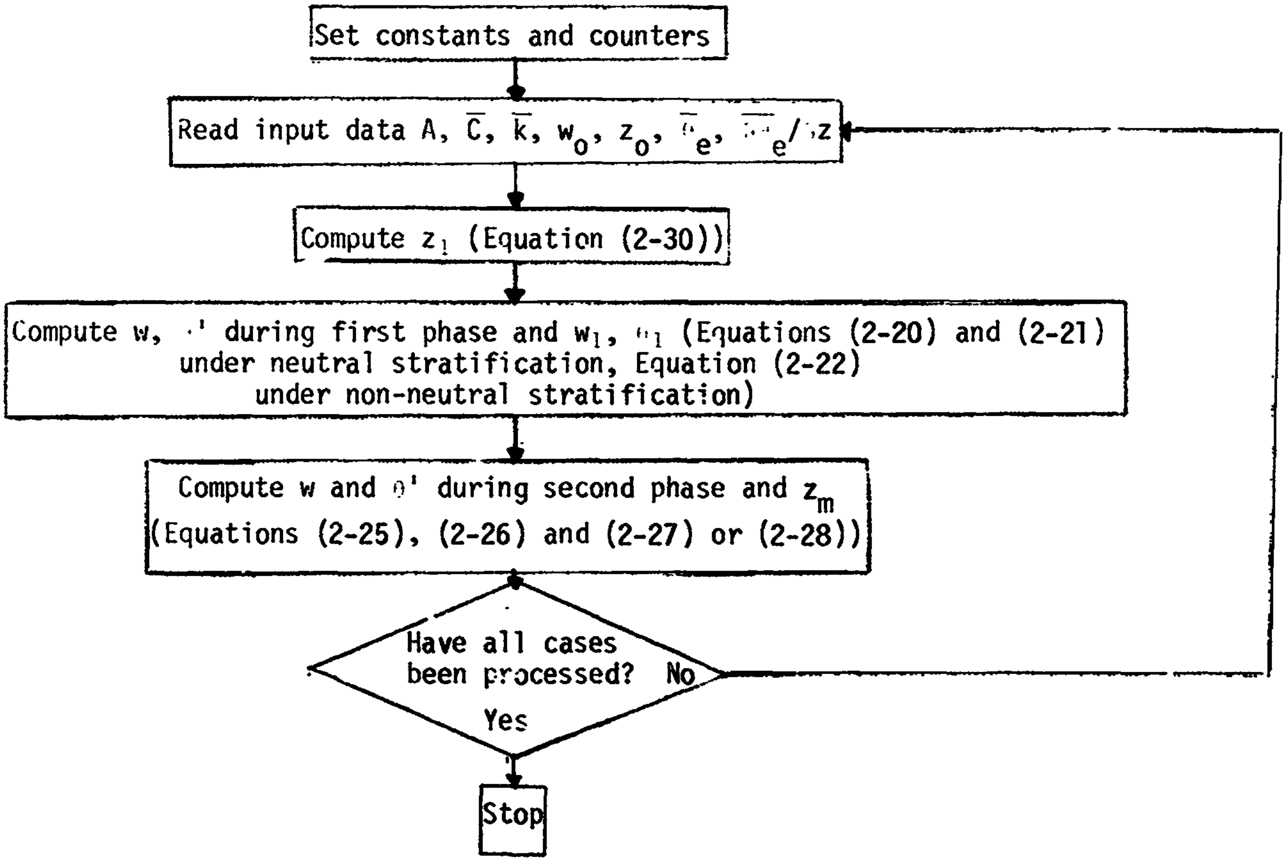

Figure 2-5 Flow diagram for computations of exhaust cloud rise and growth

2.2.5 Results of Model Computations

Model computations were carried out for twelve static engine tests for which film observation data of exhaust cloud rise and growth were available. For each of the twelve cases, the model predicts the following: (1) maximum height of cloud rise, (2) rise rate or vertical velocity of cloud as a function of height or time after its initial formation, and (3) temperature excess of cloud as a function of height or time. Growth rate of cloud is not predicted per se; rather, the linear variation of its lateral extent with height during the first phase is a derived property of the model as discussed previously in Section 2.2.2.2. Growth of the cloud during the second phase is not treated in the present model formulations.

Results of model computations were compared with observed data of cloud rise. It should be pointed out, however, that uncertainties about observed cloud rise existed in four out of the twelve cases processed for various reasons. For example, there were three cases where no reference point could be found on the early frames of the film. Observation was uncertain for another case (TWF 033) where the cloud was behind a tower for at least part of the observation period.

Table 2-8 tabulates the input data for all twelve cases for which model calculations were carried out. Note that model constants such as g, z and t are not listed in the table. In the actual computations, g had a value of 980 cm sec^{-2}, z ranged from 20 to 1600 meters (with a vertical spacing of 20 meters), and t ranged from 0 to 200 seconds.

Table 2-8 Input data for twelve cases of exhaust cloud rise and growth to be predicted by a physical-numerical model

Case	Test No.	Date	Firing Time (CST)	Duration of Firing (sec)	Model Input (Engine & Exhaust Gas Data)		
					w_o (m sec^{-1})	z_o (m)	A (10^{14}cm^3°K sec^{-1})
TWF 026	2	7/9/64	1619	23	1404	20	0.4575
TWF 027	3	7/10/64	1654	50	1404	20	0.4576
TWF 031	5	8/4/64	1124	20	1404	20	0.4568
TWF 033	6	8/25/64	1706	66	1404	20	0.4587
TWF 034	9	10/9/64	1621	24	1404	20	0.4609
TWF 035	10	10/10/64	1429	132	1404	20	0.4610
TWF 037	11	10/23/64	1640	119	1404	20	0.4609
TWF 050	12	2/18/65	1639	48	1404	20	0.4612
TWF 052	13	3/1/65	1414	60	1404	20	0.4626
S-IC 05	17	5/6/65	1510	15.6	488	30	0.4579
S-IC 06	18	5/20/65	1200	40.6	488	30	0.4580
TWF 056	19	5/26/65	1400	40	1404	20	0.4572

Continued

Table 2-8 Input data for twelve cases of exhaust cloud rise and growth to be predicted by a physical-numerical model - Continued

Case	Test No.	Raw Input (Engine and Exhaust Gas Data)					
		V (ft sec^{-1})	α (degree)	z^* (ft)	F^* (lb min^{-1} engine^{-1})	c_p (cal gm^{-1} °K^{-1})	θ' (°K)
TWF 026	2	9365	30	159	3×10^5	0.49	1769
TWF 027	3	9365	30	159	3×10^5	0.49	1769
TWF 031	5	9365	30	159	3×10^5	0.49	1766
TWF 033	6	9365	30	159	3×10^5	0.49	1773
TWF 034	9	9365	30	159	3×10^5	0.49	1782
TWF 035	10	9365	30	159	3×10^5	0.49	1782
TWF 037	11	9365	30	159	3×10^5	0.49	1782
TWF 050	12	9365	30	159	3×10^5	0.49	1783
TWF 052	13	9365	30	159	3×10^5	0.49	1789
S-IC 05	17	9365	10	232	3×10^5	0.49	1770
S-IC 06	18	9365	10	232	3×10^5	0.49	1771
TWF 056	19	9365	30	159	3×10^5	0.49	1768

Continued

Table 2-8 Input data for twelve cases of exhaust cloud rise and growth to be predicted by a physical-numerical model - Continued

Case	Test No.	Raw Input (Engine and Exhaust Gas Data)			
		P (lb/in^2)	T_{gas} ($^\circ$K)	M_o (gm mol^{-1})	R* (erg mol^{-1}$^\circ$K^{-1})
TWF 026	2	14.7	2080	23.7	8.3144×10^7
TWF 027	3	14.7	2080	23.7	8.3144×10^7
TWF 031	5	14.7	2080	23.7	8.3144×10^7
TWF 033	6	14.7	2080	23.7	8.3144×10^7
TWF 034	9	14.7	2080	23.7	8.3144×10^7
TWF 035	10	14.7	2080	23.7	8.3144×10^7
TWF 037	11	14.7	2080	23.7	8.3144×10^7
TWF 050	12	14.7	2080	23.7	8.3144×10^7
TWF 052	13	14.7	2080	23.7	8.3144×10^7
S-IC 05	17	14.7	2080	23.7	8.3144×10^7
S-IC 06	18	14.7	2080	23.7	8.3144×10^7
TWF 056	19	14.7	2080	23.7	8.3144×10^7

Continued

Table 2-8 Input data for twelve cases of exhaust cloud rise and growth to be predicted by a physical-numerical model - Continued

Case	Test No.	Model Input (Atm. Data)		
		k (sec^{-1})	$\overline{c}$ (-)	$\overline{\partial\theta_e/\partial z}$ (°K/km)
TWF 026	2	0.1462	0.6254	2.84
TWF 027	3	0.0963	0.6154	1.17
TWF 031	5	0.0830	0.5525	2.31
TWF 033	6	0.0552	0.6398	6.98
TWF 034	9	0.1109	0.6702	1.56
TWF 035	10	0.1010	0.6646	1.99
TWF 037	11	0.1561	0.6676	3.56
TWF 050	12	0.0776	0.5310	3.73
TWF 052	13	0.1041	0.6634	6.17
S-IC 05	17	0.0878	0.6588	-0.63
S-IC 06	18	0.0765	0.8069	1.16
TWF 056	19	0.1173	0.5085	-1.03

Continued

Table 2-8 Input data for twelve cases of exhaust cloud rise and growth to be predicted by a physical-numerical model - Concluded

Case	Test No.	Model Input (Atm. Data)	Raw Input (Atm. Data)
		$\overline{\theta}_e$ (° K)	$\bar{u}$ (m sec^{-1})
TWF 026	2	300.1	7.4
TWF 027	3	299.8	4.9
TWF 031	5	303.1	4.3
TWF 033	6	295.5	2.9
TWF 034	9	286.9	5.6
TWF 035	10	286.6	5.2
TWF 037	11	287.1	7.8
TWF 050	12	286.1	4.0
TWF 052	13	280.4	5.3
S-IC 05	17	298.5	4.5
S-IC 06	18	298.1	3.9
TWF 056	19	301.3	5.9

2.2.5.1 Computed Maximum Heights of Cloud Rise

Maximum heights of cloud rise for all twelve cases under neutral and non-neutral thermal stratification conditions were computed with the prediction model described in Section 2.2.2. The computed maximum heights under neutral conditions when thermal stability effects were neglected in the model and the observed maximum heights derived from film data are tabulated in Table 2-9.

In Table 2-9, columns one and two identify the test numbers and cases, column three lists the computed maximum height (z_m) with stability effects neglected for each case, column four gives the observed height (z'_m) corrected for cloud movements away or toward the camera, column five records the actual difference between the computed and observed maximum height for each case, and column six presents the percentage difference between the computed and observed maximum heights for each case. Note that there are three test numbers bearing an asterisk (*). These are the cases where the observed data were not corrected for cloud movements.

The averaged difference and averaged percentage difference in absolute values between the computed and observed maximum height for all twelve cases and for ten of the twelve cases (excluding Tests 5 and 6) were also computed and they are listed in Table 2-9.

Some observations on the comparisons between the computed and observed maximum heights of cloud rise can now be made. First of all, for the types of heat source strength employed, the computed maximum heights seem to fall into a range of reasonable values; the lowest predicted height being 866 meters and the highest being 1513 meters. Secondly, for a majority of the cases processed (seven out of the total twelve cases) the percentage

Table 2-9 Comparisons between the computed and observed maximum heights of cloud rise for twelve cases (Thermal stability effects not included in the computed heights. Observed heights are corrected for cloud movements away or toward the camera.)

Test No.	Case	z_m (meters) (computed max. height, neutral conditions)	z_m' (meters) (observed maximum height corrected)	$z_m - z_m'$ (meters)	$(z_m - z_m')/z_m'$ (%)
2	TWF 026	898	798	100	12.47
3	TWF 027	1,120	1,100	20	1.86
5	TWF 031	1,225	587	638	108.66
6	TWF 033	1,513	736	777	105.60
9	TWF 034	1,036	821	215	26.13
*10	TWF 035	1,089	1,010	79	7.79
11	TWF 037	866	926	- 60	- 6.50
*12	TWF 050	1,281	1,050	231	22.03
*13	TWF 052	1,072	1,160	- 88	- 7.56
17	S-IC 05	919	1,254	-335	-26.74
18	S-IC 06	960	1,105	-145	-13.16
19	TWF 056	1,022	1,039	- 17	- 1.61

*Observed maximum heights not corrected for cloud movements.

Averaged difference between the computed and observed maximum height for twelve cases

$$\frac{\Sigma\, |z_m - z_m'|}{12} = 225 \text{ meters}$$

Averaged difference between the computed and observed maximum height for ten cases (excluding Tests 5 and 6)

$$\frac{\Sigma\, |z_m - z_m'|}{10} = 129 \text{ meters}$$

Averaged percentage difference between the computed and observed maximum height for twelve cases

$$\Sigma\, \left|\frac{z_m - z_m'}{z_m'}\right| /12 = 28.34\%$$

Averaged percentage difference between the computed and observed maximum height for ten cases (excluding Tests 5 and 6)

$$\Sigma\, \left|\frac{z_m - z_m'}{z_m'}\right| /10 = 12.59\%$$

in absolute values between the computed and observed maximum heights is no greater than 13.16 percent (from 1.86 percent for Test 3 to -13.16 percent for Test 18). For the remaining five cases, three have percentage differences less than 27 percent (22.03 percent for Test 12, 26.13 percent for Test 9 and 26.74 percent for Test 17) and two of them have differences from 105.60 percent (Test 6) to 108.66 percent (Test 5). Thirdly, for one of the two cases (Test 6) where the percentage differences between the predicted and observed heights are the greatest, the observation was somewhat uncertain because the cloud was behind the tower for at least part of the observation period. For the other case (Test 5) which has a percentage difference of 108.66 percent, the static firing lasted for only 20 seconds. This duration of firing is very short as compared with that of 132 seconds for case 10, which has the longest firing time among all the cases processed. The extremely short duration of firing might have adversely affected the theoretical prediction for Test 5 because the model will yield the best prediction of cloud rise when the heat source is maintained long enough to be considered continuous. Finally, it is observed that the computed heights are greater than those observed in seven out of twelve cases and smaller in the remaining five cases. However, there is very little evidence to indicate a systematic bias on the part of the model to overestimate the height of the cloud rise.

It has been pointed out that there are two cases (Tests 5 and 6) where the differences between the computed and observed heights are unusually large (638 and 777 meters respectively). Attempts were made to explain the rather small maximum heights observed and the unusually large differences between the computed and observed maximum heights of cloud rise. In order to avoid bias which was possibly built-in to two cases of unusual circumstances, two sets of average differences between the computed and observed maximum heights were calculated. While the first takes all twelve cases into account, the second excludes Tests 5 and 6 in the computation. Clearly, the differences between the two sets of averages are substantial. With all twelve cases being considered, the averaged difference between the computed and observed is 225 meters, and the averaged percentage difference is 28.34 percent (the signs of the differences are disregarded). However, when Tests 5 and 6 are excluded in computing the averages, the averaged difference and averaged percentage difference are reduced to 129 meters and 12.59 percent respectively.

Table 2-10 presents comparisons between the computed maximum heights of cloud rise under non-neutral conditions (thermal stability effects included in the model) and the observed maximum cloud heights. In addition to the six columns listed in Table 2-9, two columns covering the mean values of diffusion parameters and thermal stability for each case are included in Table 2-10 for reference.

Interesting comparisons can be made between Table 2-9 and Table 2-10. The contrast is clearly demonstrated: When the stability effects are included, the averaged differences between the computed and observed maximum heights are 171 meters (twelve cases) and 116 meters (ten cases), as opposed to 225 meters (twelve cases) and 129 meters (ten cases) in Table 2-9; the averaged percentage differences are 20.76 percent vs. 28.34 percent (twelve cases) and 11.06 percent vs. 12.59 percent (ten cases).

Table 2-10 Comparisons between the computed and observed maximum heights of cloud rise for twelve cases (Thermal stability effects included in the computed heights. Observed heights are corrected for cloud movements away or toward the camera.)

Test No.	Case	z_m (meters) (computed max. height)	z_m' (meters) (Observed maximum height, corrected)	$z_m - z_m'$ (meters)	$(z_m - z_m')/z_m'$ (%)	$\bar{k}$ (sec^{-1})	$\overline{\partial\theta_e/\partial z}$ (°K/km)
2	TWF 026	895	798	97	12.16	0.1462	2.84
3	TWF 027	1,037	1,100	- 63	- 5.73	0.0963	1.17
5	TWF 031	1,085	587	498	84.84	0.0830	2.31
6	TWF 033	1,124	736	388	52.72	0.0552	6.98
9	TWF 034	995	821	174	21.19	0.1109	1.56
*10	TWF 035	1,027	1,010	17	1.68	0.1010	1.99
11	TWF 037	869	926	- 57	- 6.16	0.1561	3.56
*12	TWF 050	1,110	1,050	60	5.71	0.0776	3.73
*13	TWF 052	1,029	1,160	-131	-11.29	0.1041	6.17
17	S-IC 05	909	1,254	-345	-27.51	0.0878	-0.63
18	S-IC 06	932	1,105	-173	-15.66	0.0766	1.16
19	TWF 056	993	1,039	- 46	- 4.43	0.1173	-1.03

*Observed maximum heights not corrected for cloud movements.

Averaged difference between the computed and observed maximum height for twelve cases

$$\frac{\Sigma\, |z_m - z_m'|}{12} = 171 \text{ meters}$$

Averaged difference between the computed and observed maximum height for ten cases (excluding Tests 5 and 6)

$$\frac{\Sigma\, |z_m - z_m'|}{10} = 116 \text{ meters}$$

Averaged percentage difference between the computed and observed maximum height for twelve cases

$$\Sigma\, \left|\frac{z_m - z_m'}{z_m'}\right|/12 = 20.76\%$$

Averaged percentage difference between the computed and observed maximum height for ten cases (excluding Tests 5 and 6)

$$\Sigma\, \left|\frac{z_m - z_m'}{z_m'}\right|/10 = 11.06\%$$

Further comments on comparing the computational results in Table 2-10 with those in Table 2-9 can be made as follows: (1) The net effect of stability on the predicted maximum height is most obvious when the stability factor $(\overline{\partial\theta_e/\partial z})$ is substantial and k is relatively small. This is clearly illustrated in Test 6 where $\overline{\partial\theta_e/\partial z}$ is 6.98°K/km and k is only 0.0552 (light wind) and where consideration of stability reduces the difference between the computed and observed maximum heights from 777 meters to 388 meters, a reduction of 50 percent. (2) In general, stable conditions $(\overline{\partial\theta_e/\partial z}>0)$ tend to reduce the maximum heights and unstable conditions $(\overline{\partial\theta_e/\partial z}<0)$ have the opposite effect. (3) After the stability has been taken into account, the predicted height is now greater than the observed in six cases and less than the observed in the other six cases. It appears that the model, with or without thermal stability effects, had no bias to overestimate or underestimate the maximum height of cloud rise.

2.2.5.2 Computed Rise Rate and Temperature Excess of Cloud

Rise rate (or vertical velocity) and temperature excess of exhaust cloud, as a function of height or time after the initial formation of the cloud, were computed with the prediction model for all twelve cases.

The predicted profiles of rise rate (w) and temperature excess (θ') for one case (TWF 056, Test 19) are presented in Fig. 2-6. In Fig. 2-6 the solid line represents the predicted vertical profile of w under neutral conditions, whereas the dashed line is the observed. The computed temperature excess (θ') is plotted along the solid line. The transition level z_1 is computed at 489 meters above the ground. It is interesting to note that during the first phase, the predicted w decreases rapidly with height during the early stage and then lessens its pace of decrease as the

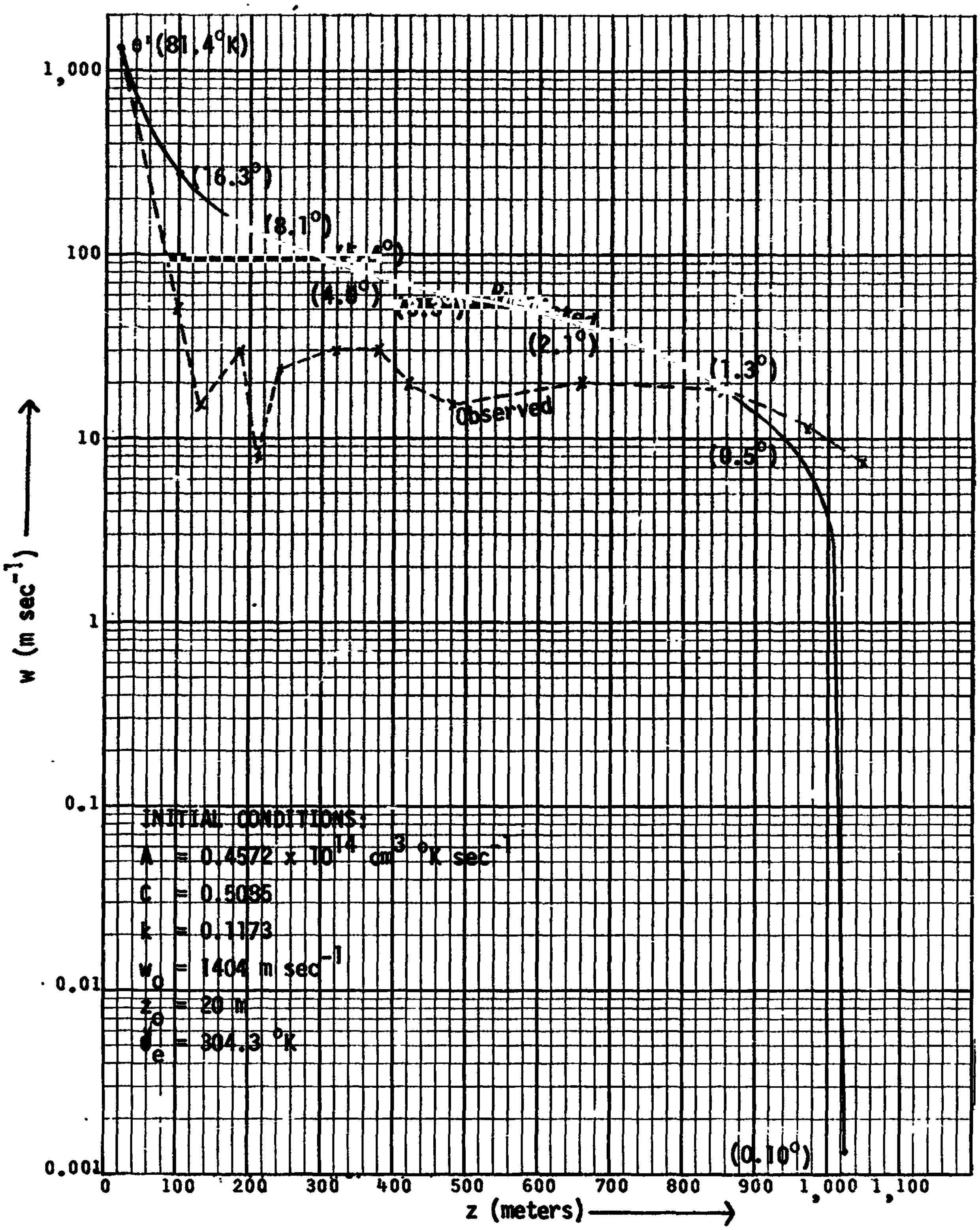

Figure 2-6 Computed vs. observed distribution of rise rate of exhaust cloud (w) with height (z), Test No. 19, Case TWF 056, 26 May 1965.

transition level is being approached. After the transition level has been reached, however, w resumes its rapid decrease in magnitude and eventually becomes negligible at the height of 1022 meters, which is the computed maximum height reached by the exhaust cloud in this case. Incidentally, this computed maximum height compares very favorably with the observed maximum height of 1039 meters. The predicted temperature excess, indicated by the numbers in parentheses in Fig. 2-6, decreases rapidly with height.

The observed rise rate or vertical velocity of the exhaust cloud also experienced rapid decrease in the early stage of cloud ascent. By the time the cloud reached the height of about 115 meters, its rise had already been reduced to about 15 m sec^{-1}, a much lower value than the computed 200 m sec^{-1} at the same height. However, the rise rate fluctuated in a narrow range from then on. By the time the cloud reached its observed maximum height at 1039 meters, it was still experiencing appreciable vertical velocity.

No comparison between the predicted and observed temperature excess of the exhaust cloud was made because the temperature excess of the cloud was not observed. However, it is interesting to observe that when the cloud reached its computed maximum height, temperature excess of the cloud was predicted to be 0.10°K only; an indication that the cloud had become environmentally stable in theory.

2.2.5.3 Sensitivity of Heights of Cloud Rise Prediction to Some Input Variables

Sensitivity of maximum height (z_m) and transition height (z_1) of cloud rise prediction to some input variables, both of engine and exhaust gas and of atmospheric categories, was investigated using Test 19 as a study case. The basic values of engine and atmospheric input variables used in the study were as follows: $w_0 = 1404$ m sec^{-1}, $z_0 = 20$ m, $A = 0.4568 \times 10^{14}$ cm^3 °K sec^{-1}, $\bar{k} = 0.1184$, $\bar{c} = 1.0$, $\overline{\partial\theta_e/\partial z} = 0.0$ °K km^{-1}, and $\theta_e = 304.3$ °K. Sensitivity of heights of cloud rise to a certain input variable was studied by varying the variable in question within a reasonable range of values, while holding all other input variables constant.

2.2.5.3.1 Effects of Initial Vertical Velocity of Cloud (w_0) on Predicted Heights of Cloud Rise

w_0 values ranging from 600 to 50,000 m sec^{-1} were used in model computations to evaluate the effects of w_0 on predicted heights of cloud rise. The results are plotted in Fig. 2-7. It is evident from Fig 2-7 that both maximum height (z_m) and transition height (z_1) of cloud rise vary rapidly and proportionally to initial vertical velocity (w_0) of the cloud. This is to be expected because momentum effect represented by w_0 plays a significant part in the plume rise, especially during the first (jet) phase of cloud rise.

2.2.5.3.2 Effects of Diffusion Parameter (k) on Predicted Heights of Cloud Rise

A wide-ranged value of k was used in the case study to assess the impact of k on z_1 and z_m while the other input variables were again held constant. The results shown in Fig. 2-8 indicate that both z_1 and z_m increase with the decreased value of k. For example, when k = 0.001, the computed z_1 and z_m are 6553 and 8604 meters respectively. However, when k = 1.0, z_1 and z_m have decreased to 168 and 335 meters respectively.

Although values of diffusion parameter k have no direct effects on the first phase (jet phase) of cloud rise, they help determine the

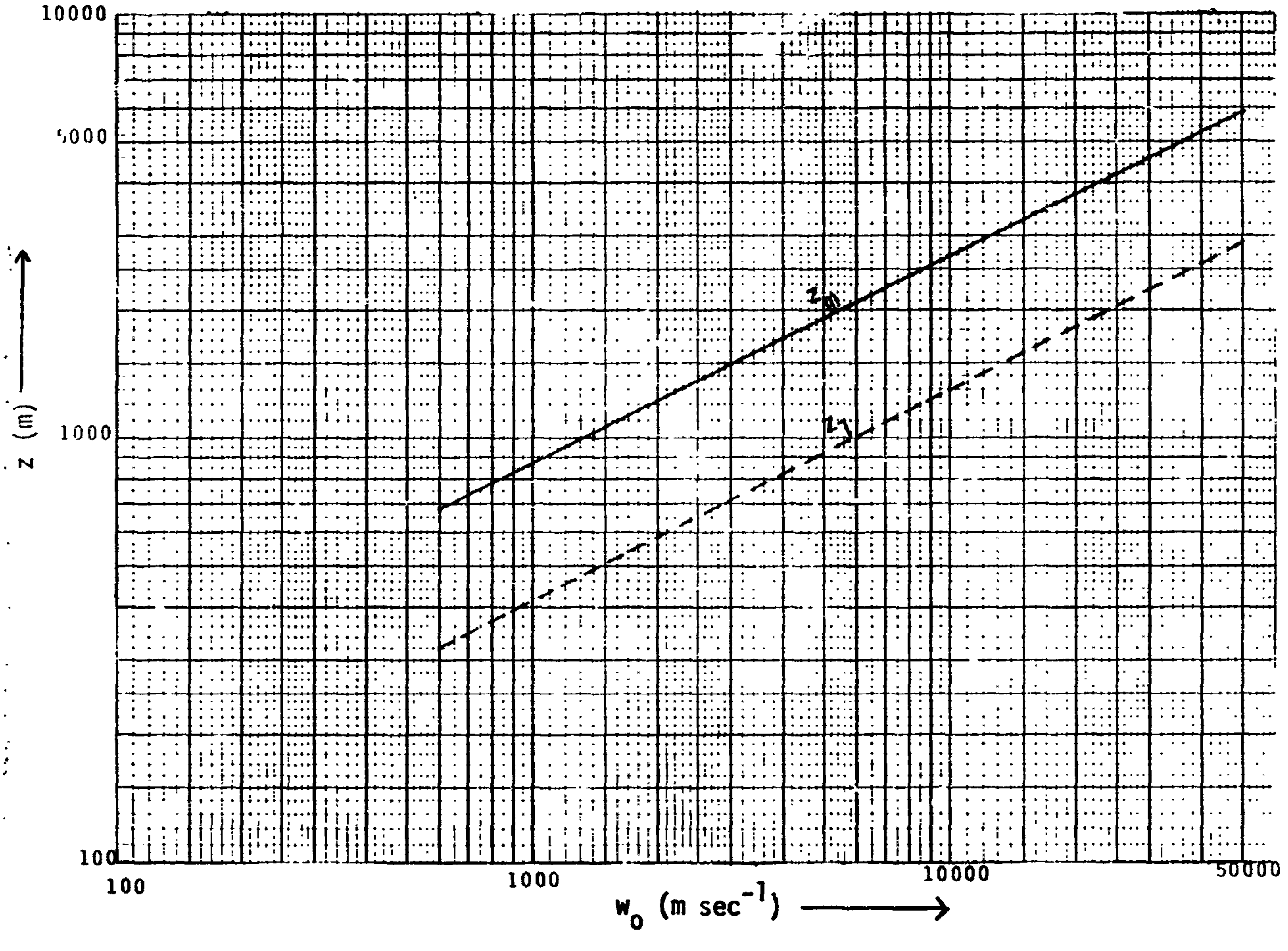

Figure 2-7 Variation of maximum height and transition height of exhaust cloud as a function of initial vertical velocity w_o, Test No. 19, Case TWF 056, 26 May 1965.

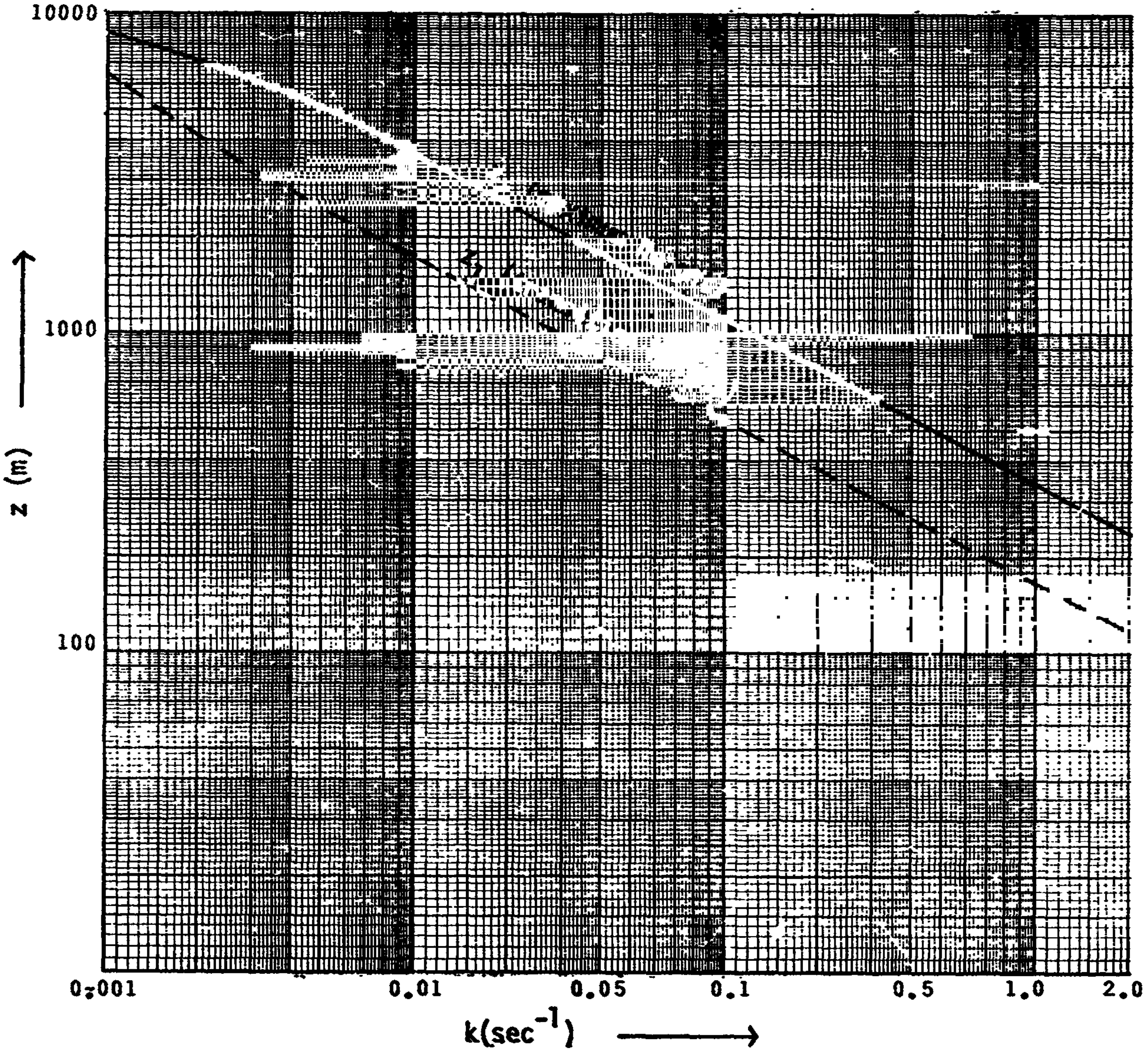

Figure 2-8. Variation of maximum height and transition height of exhaust cloud as a function of diffusion parameter k, Test No. 19, Case TWF 056, 26 May 1965.

transition height (z_1) through Equation (2-30). During the second phase, vertical velocity (w) of the cloud decreases exponentially with k as indicated in Equation (2-25), thus affecting maximum height of cloud rise through either Equation (2-27) or Equation (2-28).

2.2.5.3.3 Effects of Height of Heat Source (z_0) on Predicted Heights of Cloud Rise

Figure 2-9 shows the variations of transition height (z_1) and maximum height (z_m) as a function of z_0, the height of heat source. It is evident that both z_1 and z_m are sensitive to change in z_0. For example, when z_0 = 10 m, the computed z_m is about 740 m. When z_0 is increased to 50 meters, z_m is computed to be about 1540 meters. It is interesting to note that z_0 does not affect z_m directly in Equation (2-27) or (2-28), but that it exerts influence on z_m indirectly through variables such as w_1 and θ_1'. However, the effects of z_0 and z_1 are direct, as can be seen in Equation (2-30).

2.2.5.3.4 Effects of Heat Source Parameter (A) on Predicted Heights of Cloud Rise

Effects of heat source parameter (A) on predicted heights of cloud rise are given in Table 2-11. From this table, it can be seen that both z_1 and z_m vary only slightly with A, at least for Test 19 for which the sensitivity study was made.

2.2.5.3.5 Effects of Spreading Coefficient (c) on Predicted Heights of Cloud Rise

Variations of maximum height and transition height as a function of spreading coefficient (c) ranging from 0.5 to 10.0 are tabulated in Table 2-12.

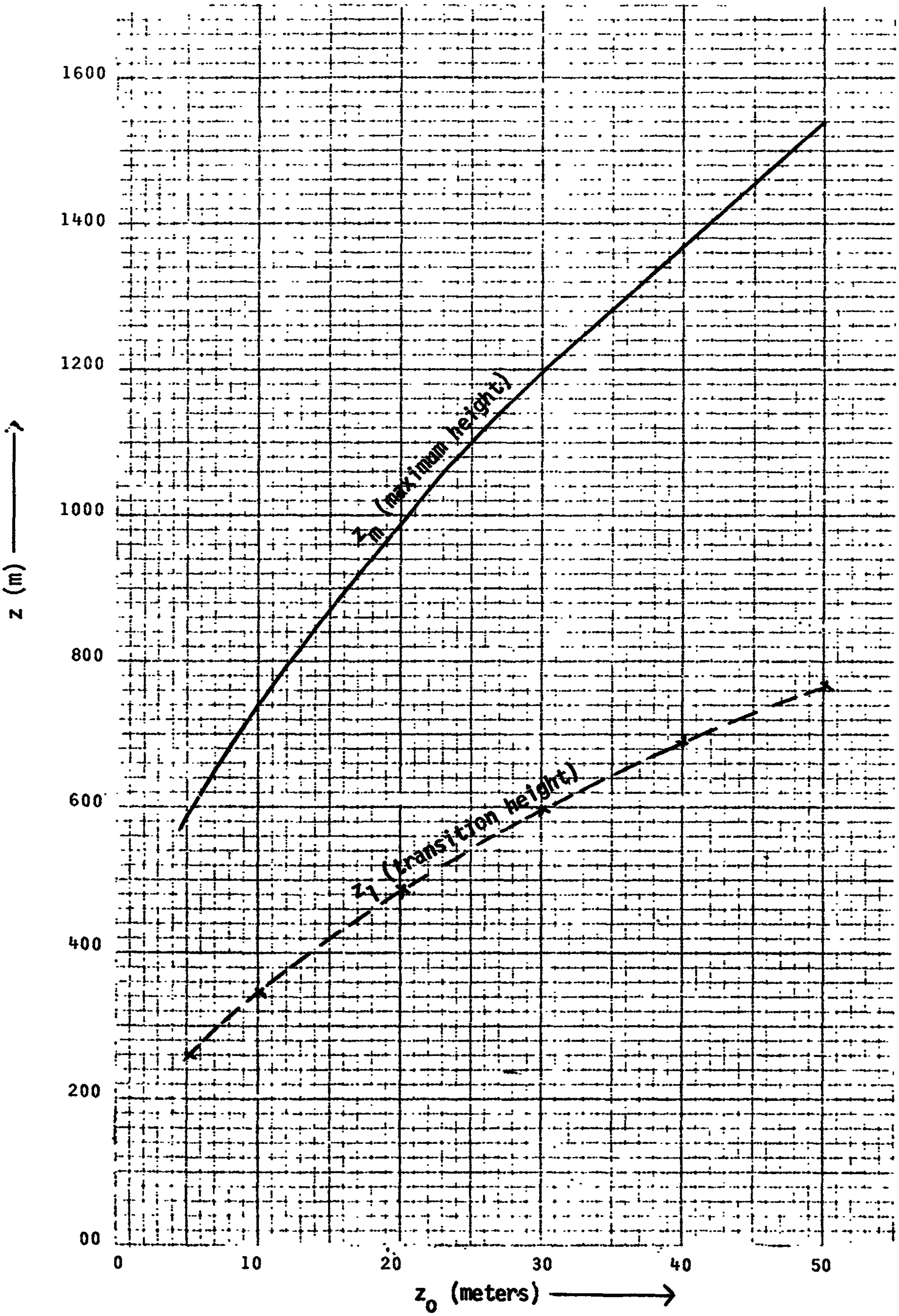

Figure 2-9 Variation of maximum height and transition height of exhaust cloud as a function of height of heat source z_o, Test No. 19, Case TWF 056

Table 2-11 Variations of maximum height (z_m) and transition height (z_1) of exhaust cloud as a function of heat source parameter, A, Test No. 19, Case TWF 056

A (cm^3 °K sec^{-1})	z_1 (meters)	z_m (meters)
0.9136 x 10^{13}	487.7	975.9
1.8272 x 10^{13}	487.7	978.2
2.7408 x 10^{13}	488.2	980.4
3.6544 x 10^{13}	488.6	982.7
4.5680 x 10^{13}	489.0	985.0
5.4816 x 10^{13}	489.4	987.2

Table 2-12 Variations of maximum height (z_m) and transition height (z_1) of exhaust cloud as a function of spreading coefficient, c, Test No. 19, Case TWF 056

c	z_1 (meters)	z_m (meters)
0.5	495	1018
1.0	489	985
2.0	488	976
3.0	488	975
5.0	488	974
10.0	488	974

It is clear from Table 2-12 that both z_1 and z_m are rather insensitive to changes in c, at least for Test 19.

2.2.6 Summary of Theoretical Study

In the theoretical study, a physical-numerical model simulating rocket engine exhaust cloud rise and growth was derived. The model was used to predict the maximum height of cloud rise for twelve cases, for which observed cloud rise data were available. Comparisons between the computed and observed maximum heights showed that the model is useful for prediction of exhaust cloud rise.

There are several advantages for using this model. First, this model simulates most of the significant physical processes involved in the rise and growth of exhaust clouds. Therefore, it has been constructed on a sound physical basis. Second, although the simulated processes and the differential equations describing them are rather complex and intricate, the solutions to the equations are mostly in algebraic form and can be easily obtained. In fact, the solutions are so straightforward that a computer program designed to obtain the solutions can be easily handled by those who are in need of the simulation data but are not necessarily familiar with the complicated processes involved. Third, the model formulations are very general in nature, applying to all types of buoyant clouds and various atmospheric conditions. The general nature of the model augments its utility and usefulness. Finally, in view of the lack of observation data on engine exhaust cloud rise, the theoretical model seems to offer a better choice over empirical prediction schemes derived on the basis of statistical analyses of observation data. It is true that the validity and usefulness of both theoretical and empirical schemes are subject to verification against more observation data to be accumulated in the future. The chances are, however, that empirical schemes will undergo frequent revisions and modifications in form as more observation data are being acquired in the future. A soundly constructed theoretical model, on the other hand, will stay more or less in its basic form, regardless of the future state of observations available.

It should be pointed out that engine exhaust cloud data are rather limited at the present time. For instance, for the twelve cases studied there were only two groups of engine and exhaust gas data with different initial vertical velocity and height of heat source. The heat source strength, represented by the parameter A, varied only slightly from case to case. More data with wide-ranged values for engine and exhaust gas parameters are needed in the future to continue the test of the model.

The potential of using the theoretical model for prediction of hot plume rise from industrial stacks is worth exploring. A recent survey showed that there were no less than thirty different stack plume rise formulas available (Briggs 1969). However, among these, the empirical formulas usually apply only to the observation data based on which the formulas were derived; the theoretically derived formulas, on the other hand, are often over-simplified so that they fail to account for most of the important physical processes and atmospheric conditions. The plume rise formulas contained in this model, although equally simple in form, take most of the physical and atmospheric processes into account. It is recommended that these formulas be tested in stack plume rise computations.

2.3 Multivariate Statistical Analysis

2.3.1 General Background

A stepwise linear regression technique was employed to develop statistical relationships between various dependent and independent variables involved in exhaust cloud rise and growth. Based on the regression analysis, predictive equations for cloud rise and growth parameters of interest were derived. Three types of data were used in the statistical analysis: (1) film observations of exhaust cloud rise and growth, (2) vehicle engine data, and (3) observed meteorological conditions.

2.3.2 Stepwise Linear Regression Technique

2.3.2.1 The Dependent and Independent Variables

This regression technique was used to relate dependent variables to independent variables involved in two phases of cloud rise and growth. Figure 2-10 illustrates the two phases: phase 1 is the layer from the height of the launching pad (z_o) to the transition height (z_1) within which jet effects are dominant, and phase 2 is the layer from the transition height to the maximum height of the cloud (z_m).

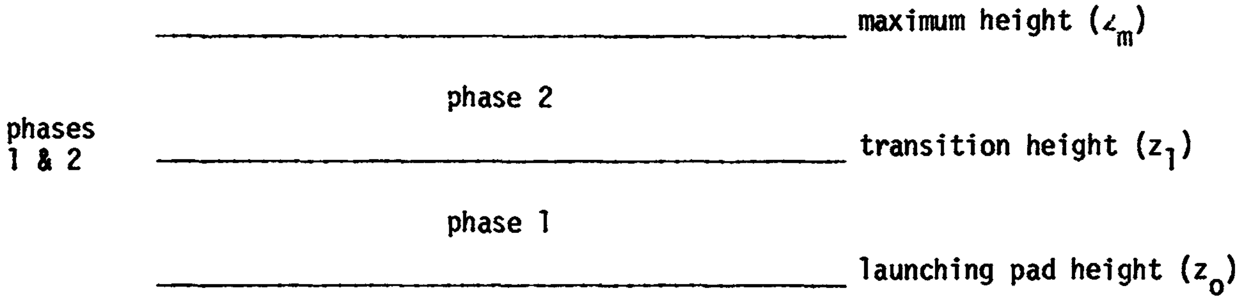

Figure 2-10 Two phases of exhaust cloud rise and growth

The dependent and independent variables used in the regression analysis are tabulated and described in Table 2-13. It can be seen that within each layer (phase 1, phase 2 and phase 1 plus phase 2) there are four dependent variables and a total of eleven independent variables, eight of which are meteorological in type and three rocket engine parameters.

2.3.2.2 Description of the Technique

A brief description of the stepwise linear regression technique will now be given. For this technique a stipulated variable (e.g., rise rate) called the predictand is the object of estimation. The variables used to make the estimation of the predictand are termed predictors. The number of plausible predictors that could be used to estimate rise rate is

Table 2-13 Description of dependent variables and independent variables used in the regression analysis

Dependent Variables	Description	Units
	Phase 1	
z_1	height of the top of phase 1 layer, or transition height	m
dz_1/dt	rate of change in z_1 with time	m/sec
A_1	average area of the cloud	m^2
dA_1/dt	rate of change in average cloud area with time	m^2/sec
	Phase 2	
z_2	depth of phase 2 layer, equal to $z_m - z_1$	m
dz_2/dt	rate of change in z_2 with time	m/sec
A_2	average area of the cloud	m^2
dA_2/dt	rate of change in average cloud area with time	m^2/sec
	Phase 1 Plus Phase 2	
z_m	depth of the total layer; i.e., maximum height of cloud	m
dz_m/dt	rate of change in z_m with time	m/sec
A^*	average area of the cloud	m^2
dA^*/dt	rate of change in average cloud area with time	m^2/sec
(meteorological)	Phase 1, 2 and Phase 1 Plus Phase 2	
$\overline{T}$	average temperature in the layer	°K
$\overline{u}$	average wind speed in the layer	m/sec
$\overline{RH}$	average relative humidity in the layer	%
dT/dz	rate of change in temperature with height	°K/m
$\overline{p}$	average pressure in the layer	mb
dp/dz	rate of change in pressure with height	mb/m
du/dz	rate of change in wind speed with height	1/sec
$\overline{\rho}$	average density in the layer	gm/cm^3
(vehicle engine)		
TH	engine thrust	lb
D	duration of firing	sec
F	fuel ratio	--

rather large. It is well known from statistical theory that the larger the number of predictors, the greater the "shrinkage in accuracy of estimation" when the procedure is applied to actual data. This situation imposes the practical necessity of selecting a manageable number of predictors. The stepwise regression technique makes a preferential selection of effective predictors from a large set of possible choices. Experiments comparing performance on independent data of estimation functions using large numbers of predictors with those using selectively chosen subsets of such variables have shown, as a rule, that whatever estimation accuracy resides in the large set is almost wholly contained in the much smaller subset. The objective selection of such a small subset is termed a stepwise procedure. After the procedure has been applied, the redundant or noncontrolling predictors are eliminated from subsequent analyses, and a multiple regression equation is developed using only the selected predictors.

In multiple regression, the predictand, Q, is expressed as a linear function of a number (P) of predictor variables:

$$Q = A_0 + A_1X_1 + A_2X_2 + \ldots + A_pX_p$$

where the coefficients $A_p(p=0,1,\ldots,P)$ are determined by least squares. To select the first predictor, the simple linear correlation is computed between the predictand and each predictor. Next, partial correlations between each of the remaining predictors and the predictand (holding the first selected predictor constant) are examined and the predictor associated with the best partial coefficient is then selected as a second predictor. Additional predictors are selected in a similar manner. Selection is halted on the basis of an F-test criterion.

2.3.2.3 Results of Regression Analysis

The stepwise regression technique was carried out for cloud rise data both uncorrected and corrected for cloud movements away or towards the camera. Table 2-14 shows the correlation coefficients for both data sets between the four dependent variables for each phase and the eleven independent variables. Note that there are two numbers in each box. The first number is the correlation coefficient applied to the uncorrected cloud rise data, while the second number is that for the corrected data. Also note that the two numbers in each box are generally in close agreement.

Tables 2-15 through 2-18 present some results from the stepwise technique for both data sets and show the order of selection of each independent variable and the corresponding reduction in variance for each phase and each dependent variable. Again note that analysis results for corrected and uncorrected data sets are very similar.

It should be pointed out that the stepwise regression technique requires a "stopping rule" so that not all variables will ultimately be selected. The stopping rule states that variables will continually be selected and reduction in variance computed until the level of significance determined by the "F ratio" drops below 90 percent. Computed results in Tables 2-15 through 2-18 show that in all cases the variable TH (thrust) was selected. Furthermore, Table 2-14 shows that in most cases the correlation coefficient for this variable is quite high (especially in the rates of change in height and area). Thus, for an order of magnitude in prediction of rate change of height and area, knowledge of thrust seems to be indispensable.

Table 2-14 Correlation coefficients between dependent and independent variables

	Height			Change in Height			Average Area			Change in Area		
	z_1	z_2	z_m	dz_1/dt	dz_2/dt	dz_m/dt	A_1	A_2	A^*	dA_1/dT	dA_2/dT	dA^*/dT
Temperature ($\overline{T}$)	0.80 0.80	-0.17 -0.26	0.04 -0.05	0.30 0.31	0.30 0.30	0.40 0.40	0.58 0.58	-0.09 -0.17	-0.11 -0.18	0.25 0.19	0.14 0.11	0.17 0.14
Wind Speed ($\overline{u}$)	-0.12 -0.11	0.27 0.27	0.39 0.49	-0.55 -0.55	0.10 0.11	-0.02 0.02	-0.44 -0.39	0.17 0.17	0.18 0.26	-0.50 -0.46	0.01 0.07	-0.04 0.03
Rel. Hum. ($\overline{RH}$)	-0.07 -0.06	0.07 -0.01	-0.09 -0.14	0.10 0.11	0.44 0.42	0.21 0.21	-0.07 -0.07	-0.10 0.04	-0.12 -0.16	-0.01 -0.02	0.43 0.32	0.11 0.09
Duration of Launch (D)	-0.55 -0.53	0.06 0.13	-0.08 0.01	-0.33 -0.33	-0.38 -0.35	-0.42 -0.42	-0.41 -0.43	0.18 0.24	0.21 0.30	-0.28 -0.22	-0.25 -0.14	-0.18 -0.16
Fuel Ratio (F)	-0.11 -0.14	-0.10 -0.17	-0.14 -0.21	-0.07 -0.09	-0.10 -0.13	-0.10 -0.14	-0.19 -0.22	-0.22 -0.27	-0.21 -0.27	-0.14 -0.13	-0.12 -0.19	-0.16 -0.16
dT/dz	-0.00 -0.17	0.70 0.68	0.17 0.16	0.14 0.13	0.14 0.14	-0.19 -0.19	-0.10 -0.13	0.40 0.40	0.16 0.16	-0.04 -0.03	0.23 0.25	-0.03 -0.03
Pressure ($\overline{p}$)	-0.73 -0.73	-0.61 -0.51	-0.90 -0.90	-0.16 -0.17	-0.60 -0.62	-0.61 -0.65	-0.44 -0.42	-0.51 -0.49	-0.66 -0.65	-0.10 -0.06	-0.39 -0.53	-0.61 -0.63
Thrust (TH)	0.19 0.16	0.66 0.61	0.74 0.67	0.97 0.97	0.93 0.92	0.92 0.92	0.77 0.79	0.82 0.76	0.80 0.73	0.99 0.98	0.97 0.95	0.97 0.96
Wind Shear du/dz	-0.46 -0.47	-0.00 -0.01	0.03 0.06	-0.32 -0.34	0.16 0.15	0.24 0.23	-0.47 -0.46	-0.05 -0.06	0.17 0.18	-0.28 -0.24	0.14 0.09	0.24 0.27

Continued

Table 2-14 Correlation coefficients between dependent and independent variables - Concluded

	Height			Change in Height			Average Area			Change in Area		
	z_1	z_2	z_m	dz_1/dt	dz_2/dt	dz_m/dt	A_1	A_2	A^*	dA_1/dT	dA_2/dT	dA^*/dT
Press. Grad.	0.82	0.15	0.28	0.33	0.52	0.11	0.62	0.22	0.43	0.28	0.35	0.18
$(\frac{dp}{dz})$	0.81	0.05	0.32	0.35	0.53	0.13	0.60	0.14	0.48	0.21	0.35	0.20
Density	-0.80	-0.20	-0.42	-0.28	-0.52	-0.61	-0.56	-0.20	-0.21	-0.23	-0.30	-0.42
(ρ)	-0.80	-0.13	-0.34	-0.30	-0.53	-0.63	-0.55	-0.14	-0.14	-0.16	-0.35	-0.42

Table 2-15 Stepwise regression results, height

Corrected Data						
Dependent Variable						
	z_1		z_2		z_m	
Order of Selection	Variable Selected	Reduction in Variance	Variable Selected	Reduction in Variance	Variable Selected	Reduction in Variance
1	dp/dz	0.67	dT/dz	0.47	$\overline{p}$	0.81
2	$\overline{RH}$	0.80	$\overline{p}$	0.74	$\overline{T}$	0.89
3	$\overline{\rho}$	0.87	TH	0.85	TH	0.93
4	TH	0.90			D	0.97

Uncorrected Data						
Dependent Variable						
	z_1		z_2		z_m	
Order of Selection	Variable Selected	Reduction in Variance	Variable Selected	Reduction in Variance	Variable Selected	Reduction in Variance
1	dp/dz	0.67	dT/dz	0.49	$\overline{p}$	0.81
2	$\overline{RH}$	0.81	TH	0.81	TH	0.90
3	$\overline{\rho}$	0.89	$\overline{p}$	0.92	dT/dz	0.95

Table 2-16 Stepwise regression results, change in height

Corrected Data						
	Dependent Variable					
	dz_1/dt		dz_2/dt		dz_m/dt	
Order of Selection	Variable Selected	Reduction in Variance	Variable Selected	Reduction in Variance	Variable Selected	Reduction in Variance
1	TH	0.95	TH	0.85	TH	0.85
2	dT/dz	0.97	[illegible]	0.95	[illegible]	0.97
3			du/dz	0.97	du/dz	0.99

Uncorrected Data						
	Dependent Variable					
	dz_1/dt		dz_2/dt		dz_m/dt	
Order of Selection	Variable Selected	Reduction in Variance	Variable Selected	Reduction in Variance	Variable Selected	Reduction in Variance
1	TH	0.95	TH	0.87	TH	0.85
2	dT/dz	0.97	[illegible]	0.96	[illegible]	0.96
3			du/dz		du/dz	0.98

Table 2-17 Stepwise regression results, area

Corrected Data						
Dependent Variable						
Order of Selection	A_1		A_2		A*	
	Variable Selected	Reduction in Variance	Variable Selected	Reduction in Variance	Variable Selected	Reduction in Variance
1	TH	0.63	TH	0.59	TH	0.54
2	dp/dz	0.82	D	0.81	D	0.81
3	dT/dz	0.91	$\bar{p}$	0.93	$\bar{p}$	0.95
Uncorrected Data						
Dependent Variable						
Order of Selection	A_1		A_2		A*	
	Variable Selected	Reduction in Variance	Variable Selected	Reduction in Variance	Variable Selected	Reduction in Variance
1	TH	0.60	TH	0.68	TH	0.63
2	dp/dz	0.80	D	0.84	D	0.83
3	dT/dz	0.88	$\bar{p}$	0.93	$\bar{p}$	0.95

Table 2-18 Stepwise regression results, rate of change in area

Corrected Data

Dependent Variable

Order of Selection	dA_1/dt		dA_2/dt		dA^*/dt	
	Variable Selected	Reduction in Variance	Variable Selected	Reduction in Variance	Variable Selected	Reduction in Variance
1	TH	0.97	TH	0.91	TH	0.93
2	$\overline{RH}$	0.98	$\bar{p}$	0.94	$\bar{p}$	0.96
3			D	0.97		

Uncorrected Data

Dependent Variable

Order of Selection	dA_1/dt		dA_2/dt		dA^*/dt	
	Variable Selected	Reduction in Variance	Variable Selected	Reduction in Variance	Variable Selected	Reduction in Variance
1	TH	0.98	TH	0.94	TH	0.94
2	$\bar{p}$	0.97				

2.3.3 Regression Equations

2.3.3.1 Thrust-Dominant Regression Equations

Based on the results of the regression analysis presented earlier (Section 2.3.2.3), a series of regression equations relating time rates of change in heights and area with engine thrust was derived. Tables 2-19 through 2-24 list these thrust-dominant regression equations and corresponding residuals computed for ten cases. It appears that a fairly good prediction of time rates of change in heights and area can be achieved using the derived regression equations.

2.3.3.2 Regression Equations Dominated by Meteorological Variables

It may be recalled from Table 2-6 that there are only three values of thrust for all ten cases considered: TH = 1,504,000 lbs. for seven cases, TH = 1,600,000 lbs. for one case, and TH = 7,500,000 lbs. for the remaining two cases. Consequently, the eight cases where TH had a value ranging from 1,504,000 to 1,600,000 lbs. were used to derive regression equations relating dependent variables to independent variables that were meteorological in nature.

Table 2-25 shows the correlation coefficients for both data sets between the four dependent variables for the total (phase 1 plus phase 2) layer and the eight meteorological variables. Again, there is gererally little difference between the coefficients derived for corrected and uncorrected data. Tables 2-26 and 2-27 list the results of the stepwise technique for parameters in various layers and show the order of selection of each independent variable and the corresponding reduction in variance. The "stopping rule" was the same as that used for developing thrust-dominant regression equations.

Table 2-19 Phase 1 - dz_1/dt (m sec $^{-1}$)
$dz_1/dt = 3.2 \times 10^{-4}(TH) + 18.0$

Table of Residuals			
Case	Actual	Predicted	Residuals (Actual-Predicted)
TWF034	21.5	22.8	- 1.3
TWF033	23.8	22.8	1.0
TWF031	23.3	22.8	0.5
TWF056	24.8	22.8	2.0
TWF037	19.5	22.8	- 3.3
TWF027	23.3	22.8	0.5
TWF026	22.3	22.8	- 0.5
No. 23	24.4	23.1	1.3
SIC05	39.6	42.1	- 2.5
SIC06	44.5	42.1	2.4

Table 2-20 Phase 2 - dz_2/dt (m sec^{-1})
$dz_2/dt = 3.1 \times 10^{-4}(TH) + 7.1$

Table of Residuals			
Case	Actual	Predicted	Residuals (Actual-Predicted)
TWF034	6.4	11.7	-5.3
TWF033	14.0	11.7	2.3
TWF031	11.8	11.7	0.1
TWF056	17.0	11.7	5.3
TWF037	7.4	11.7	-4.3
TWF027	13.9	11.7	2.2
TWF026	11.9	11.7	0.2
No. 23	12.0	12.1	-0.1
SIC05	33.0	30.4	2.6
SIC06	27.8	30.4	-2.6

Table 2-21 Phase 1 plus phase 2 - dz_m/dt (m sec $^{-1}$)

$$dz_m/dt = 3.1 \times 10^{-4}(TH) + 8.9$$

Table of Residuals			
Case	Actual	Predicted	Residuals (Actual-Predicted)
TWF034	8.4	13.4	-5.0
TWF033	15.0	13.4	1.6
TWF031	15.8	13.4	2.4
TWF056	18.2	13.4	4.8
TWF037	8.2	13.4	-5.2
TWF027	15.1	13.4	1.7
TWF026	14.0	13.4	0.6
No. 23	13.5	13.7	-0.2
SIC05	33.8	31.7	1.1
SIC06	29.8	31.7	-1.9

Table 2-22 Phase 1 - dA_1/dt (m^2 sec $^{-1}$)

$$dA_1/dt = 9.9 \times 10^{-2}(TH) + 6.54 \times 10^2$$

Table of Residuals			
Case	Actual	Predicted	Residuals (Actual-Predicted)
TWF034	2045	2138	-93
TWF033	1707	2138	-431
TWF031	1270	2138	-868
TWF056	2319	2138	281
TWF037	2320	2138	182
TWF027	2948	2138	810
TWF026	2227	2138	89
No. 23	2370	2233	137
SIC05	8106	8059	47
SIC06	8010	8059	-49

Table 2-23 Phase 2 - dA_2/dt (m^2 sec^{-1})

$dA_2/dt = 1.4 \times 10^{-3}(TH) + 7.51 \times 10^2$

Table of Residuals

Case	Actual	Predicted	Residuals (Actual-Predicted)
TWF034	1534	2862	-1328
TWF033	3003	2862	141
TWF031	1594	2862	-1268
TWF056	4631	2862	1769
TWF037	3104	2862	242
TWF027	4256	2862	1394
TWF026	2414	2862	-448
No. 23	2488	2996	-508
SIC05	10330	11270	-940
SIC06	12220	11270	950

Table 2-24 Phase 1 plus phase 2 - dA^*/dt (m^2 sec^{-1})

$dA^*/dt = 1.2 \times 10^{-3}(TH) + 9.65 \times 10^2$

Table of Residuals

Case	Actual	Predicted	Residuals (Actual-Predicted)
TWF034	1571	2918	-1347
TWF033	3311	2918	393
TWF031	1926	2918	-992
TWF056	4266	2918	1348
TWF037	3055	2918	137
TWF027	4095	2918	1177
TWF026	2429	2918	-489
No. 23	2818	3043	-225
SIC05	10300	10700	-400
SIC06	11110	10700	410

Table 2-25 Correlation coefficients for the four dependent variables and eight meteorological variables for the phase 1 and 2 layer for both corrected and uncorrected data sets

Independent Variables	Dependent Variables							
	z_m		dz_m/dt		A*		dA*/dt	
	Corrected	Uncorrected	Corrected	Uncorrected	Corrected	Uncorrected	Corrected	Uncorrected
$\overline{T}$	-0.14	-0.02	0.90	0.88	-0.37	-0.31	0.25	0.36
$\overline{u}$	0.76	0.66	-0.23	-0.29	0.72	0.70	0.37	0.29
$\overline{RH}$	-0.24	-0.19	0.44	0.41	-0.34	-0.33	0.03	0.10
dT/dz	0.36	0.41	-0.21	-0.21	0.36	0.41	0.33	0.34
$\overline{p}$	-0.87	-0.90	-0.42	-0.33	-0.55	-0.60	-0.72	-0.74
du/dz	-0.32	-0.40	-0.33	-0.26	-0.07	-0.14	-0.20	-0.37
dp/dz	0.35	0.30	0.94	0.03	0.63	0.63	0.46	0.43
$\overline{\rho}$	-0.15	-0.27	-0.91	-0.87	0.15	-0.08	-0.44	-0.55
Mean	-0.031	-0.051	0.023	-0.080	0.066	0.035	0.010	-0.009
Variance	0.26	0.29	0.42	0.37	0.48	0.48	0.42	0.46

Table 2-26 Relationships derived using regression analysis based on the corrected data set showing order of selection and reduction in variance, height

Height

Dependent Variable

Order of Selection	z_1		z_2		z_m	
	Variable Selected	Reduction in Variance	Variable Selected	Reduction in Variance	Variable Selected	Reduction in Variance
1	dp/dz	0.66	dT/dz	0.62	du/dz	0.28
2	$\overline{RH}$	0.81			$\bar{u}$	0.59
3	$\bar{p}$	0.93			$\bar{T}$	0.70
4	$\bar{u}$	0.99			dp/dz	0.90
5	$\bar{T}$	0.99				

Rate of Change in Height

Dependent Variable

Order of Selection	dz_1/dt		dz_2/dt		dz_m/dt	
	Variable Selected	Reduction in Variance	Variable Selected	Reduction in Variance	Variable Selected	Reduction in Variance
1	$\bar{p}$	0.58	$\bar{\rho}$	0.74	$\bar{\rho}$	0.82
2			du/dz	0.88	du/dz	0.90
3			$\overline{RH}$	0.96	dT/dz	0.98
4			dT/dz	0.99		

Table 2-27 Relationships derived using regression analysis based on the corrected data set showing order of selection and reduction in variance, area

Area						
Dependent Variable						
Order of Selection	A_1		A_2		A^*	
	Variable Selected	Reduction in Variance	Variable Selected	Reduction in Variance	Variable Selected	Reduction in Variance
1	dp/dz	0.50	No Significant Relationships		$\bar{u}$	0.52
2	dT/dz	0.76			dT/dz	0.68
3					dp/dz	0.88
Change in Area						
Dependent Variable						
Order of Selection	dA_1/dt		dA_2/dt		dA^*/dt	
	Variable Selected	Reduction in Variance	Variable Selected	Reduction in Variance	Variable Selected	Reduction in Variance
1	No Significant Relationships		$\bar{p}$	0.52	$\bar{p}$	0.52

Based on the results of analysis, predictive equations relating dependent variables with independent variables of a meteorological nature were derived. The predictive equations and corresponding residuals computed for all eight cases are tabulated in Tables 2-28 through 2-37. The actual values of dependent variables used in residual computations are observed cloud data corrected for cloud movements away or toward the camera.

Table 2-28 Predictive equation with corresponding table of residuals for dependent variable z_1 (m)

$$z_1 = -3.05 \times 10^3\ dp/dz + 1.78 \times 10^4\ \bar{\rho} - 5.65 \times 10^1\ \bar{p}$$
$$-7.54 \times 10^{-1}\ \bar{u} + 2.12 \times 10^2\ \bar{T} - 6.67 \times 10^4$$

Table of Residuals			
Case	Actual	Predicted	Residual
TWF026	201	206	-5
TWF027	210	217	-7
TWF031	303	279	24
TWF033	119	158	-39
TWF034	151	123	28
TWF037	137	157	-20
TWF056	222	231	-9
No. 23	171	141	-30

Table 2-29 Predictive equation with corresponding table of residuals f
dependent variable z_2 (m)

$$z_2 = -3.39 \times 10^4\ dT/dz + 3.87 \times 10^2$$

Table of Residuals			
Case	Actual	Predicted	Residual
TWF026	597	651	-54
TWF027	890	668	222
TWF031	284	600	-316
TWF033	617	491	126
TWF034	670	709	-39
TWF037	789	685	104
TWF056	817	739	78
No. 23	601	719	-118

Table 2-30 Predictive equation with corresponding table of residuals for dependent variable z_m (m)

$$z_m = 2.71 \times 10^5\, dp/dz + 1.76 \times 10^2\, \bar{u} - 4.61 \times 10^4\, du/dz - 1.23 \times 10^2\, \bar{T} + 6.59 \times 10^4$$

Table of Residuals

Case	Actual	Predicted	Residual
TWF026	798	786	12
TWF027	1100	1055	45
TWF031	587	638	-51
TWF033	736	721	15
TWF034	821	904	-83
TWF037	926	887	39
TWF056	1039	1061	-22
No. 23	772	724	48

Table 2-31 Predictive equation with corresponding table of residuals for dependent variable dz_1/dt (m sec^{-1})

$$dz_1/dt = -2.55 \times 10^{-1}\, \bar{p} + 2.75 \times 10^2$$

Table of Residuals

Case	Actual	Predicted	Residual
TWF026	22.3	23.9	-1.6
TWF027	23.3	23.4	-0.1
TWF031	23.3	23.2	0.1
TWF033	23.8	22.5	1.3
TWF034	21.5	22.0	-0.5
TWF037	19.5	22.8	-3.3
TWF056	24.8	24.7	0.1
No. 23	24.4	22.3	2.1

Table 2-32 Predictive equation with corresponding table of residuals for dependent variable dz_2/dt (m sec $^{-1}$)

$$dz_2/dt = -3.39 \times 10^2 \bar{\rho} + 2.50 \times 10^2 \, du/dz + 1.78 \times 10^{-2} \overline{RH} - 2.15 \times 10^2 \, dT/dz + 1.17 \times 10^2$$

Table of Residuals			
Case	Actual	Predicted	Residual
TWF026	11.9	12.6	-0.7
TWF027	13.9	13.6	0.3
TWF031	11.8	15.1	-3.3
TWF033	14.0	11.9	2.1
TWF034	6.4	8.1	-1.7
TWF037	7.4	7.4	0
TWF056	17.0	15.1	1.9
No. 23	12.0	10.6	1.4

Table 2-33 Predictive equation with corresponding table of residuals for dependent variable dz_m/dt (m sec $^{-1}$)

$$dz_m/dt = -40 \rho + 95.9 \, du/dz + 19.7 \, dT/dz + 13.5$$

Table of Residuals			
Case	Actual	Predicted	Residual
TWF026	14.0	15.7	-1.7
TWF027	15.1	15.1	0
TWF031	15.8	17.2	-1.4
TWF033	15.0	13.6	1.4
TWF034	8.4	9.0	-0.6
TWF037	8.2	8.7	-0.5
TWF056	18.2	16.5	1.7
No. 23	13.5	12.2	1.3

Table 2-34 Predictive equation with corresponding table of residuals for dependent variable A_1 ($m2$)

$$A_1 = 4.63 \times 10^5\ dp/dz - 3.73 \times 10^5\ dT/dz + 5\ 96 \times 10^4$$

Table of Residuals			
Case	Actual	Predicted	Residual
TWF026	10022	9363	659
TWF027	13265	11927	1338
TWF031	16510	14485	2025
TWF033	4269	7228	-2959
TWF034	7157	8402	-1245
TWF037	8120	6075	2045
TWF056	10436	13418	-2982
No. 23	8261	7137	1124

Table 2-35 Predictive equation with corresponding table of residuals for dependent variable A* (m^2)

$$A^* = -1.13 \times 10^4\ \bar{u} - 7.72 \times 10^6\ dT/dz + 5.53 \times 10^6\ dp/dz + 6.81 \times 10^5$$

Table of Residuals			
Case	Actual	Predicted	Residual
TWF026	74095	99729	-24634
TWF027	149475	90696	58779
TWF031	35640	92123	-56483
TWF033	78355	52486	25869
TWF034	76205	71151	5054
TWF037	17265	37897	-20632
TWF056	121600	103108	18492
No. 23	70470	75910	-5440

Table 2-36 Predictive equation with corresponding table of residuals for dependent variable dA_2/dt (m^2 sec^{-1})

$dA_2/dt = -1.37 \times 10^2 \bar{p} + 1.31 \times 10^5$

Table of Residuals			
Case	Actual	Predicted	Residual
TWF026	2414	3271	-857
TWF027	4256	3079	1176
TWF031	1594	2847	-1253
TWF033	3003	2628	375
TWF034	1534	2737	-1203
TWF037	3104	2080	1024
TWF056	4631	3696	935
No. 23	2488	2682	-194

Table 2-37 Predictive equation with corresponding table of residuals for dependent variable dA^*/dt (m^2 sec^{-1})

$dA^*/dt = -9.28 \times 10^1 \bar{p} + 9.05 \times 10^4$

Table of Residuals			
Case	Actual	Predicted	Residual
TWF026	2429	3228	-799
TWF027	4095	3089	1006
TWF031	1926	2940	-1014
TWF033	3311	2764	547
TWF034	1571	2801	-1230
TWF037	3055	2347	708
TWF056	4266	3506	760
No. 23	2818	2792	26

2.3.3.5 Corrected and Uncorrected Data

Two sets of cloud observation data were available for use in the multivariate regression analysis. One set consisted of those data uncorrected for cloud movements away or toward the camera while the other set included those data for which such corrections had been made. An analysis was then carried out to see whether different regression equations should be derived for corrected and uncorrected data.

The first step of the analysis was to compute a series of standard deviations for the dependent parameters. Take, for the present time, z_m for example. A series of standard deviations was computed as follows: σ_A, the standard deviation for corrected z_m; σ_B, the standard deviation for uncorrected z_m; and σ_D, the standard deviation for the difference between corrected and uncorrected z_m. The computed standard deviations for all ten cases are listed in the first half of Table 2-38. The computational results show that there is only a slight difference between σ_A (206) and σ_B (195), and that σ_D (37.6) is much smaller than either σ_A or σ_B. This indicates that statistically there is very little difference between the corrected and uncorrected z_m, at least for the ten cases analyzed.

The same analysis was carried out for dz_m/dt, the time rate of change of z_m. The computed standard deviations are listed in the second half of Table 2-38. The computational results again show that there is little difference between σ_A (8.3) and σ_B (8.2), and that σ_D (0.49) is much smaller than either σ_A or σ_B. Again, the indication is that statistically there is only a slight difference between the corrected and uncorrected data of dz_m/dt. This analysis was later extended to cover all other dependent variables as well. Results show invariably that statistically there is very little difference between the corrected and uncorrected data.

Table 2-38 Computed standard deviations for both uncorrected and corrected data and their difference for z_m and dz_m/dt

Case	z_m (m)			dz_m/dt (m sec^{-1})		
	Corrected	Uncorrected	Difference	Corrected	Uncorrected	Difference
TWF034	821	743	78	8.4	7.6	0.8
TWF033	736	717	19	15.0	14.6	0.4
TWF031	587	563	24	15.8	15.2	0.6
TWF056	1039	974	65	18.2	17.0	1.2
TWF037	926	827	99	8.2	7.3	0.9
TWF027	1100	1037	63	15.1	14.0	1.1
TWF026	798	799	-1	14.0	13.1	0.9
No. 23	772	786	-14	13.5	13.8	-0.3
SIC05	1254	1197	57	33.8	32.3	1.5
SIC06	1105	1098	7	29.8	29.4	0.4
Standard Deviation	$\sigma_A = 206$	$\sigma_B = 195$	$\sigma_D = 37.6$	$\sigma_A = 8.3$	$\sigma_B = 8.2$	$\sigma_D = 0.49$

Conclusions drawn from the preceding analysis, that there is little difference statistically between the corrected and uncorrected data of cloud parameters, were supported by comparisons of correlation coefficients tabulated in Table 2-14. It may be recalled that for each pair of dependent and independent variables, the correlation coefficients computed for corrected and uncorrected data were generally in close agreement. Consequently, regression equations were developed for and verified against corrected data only.

2.3.4 Summary of Multivariate Statistical Analysis

Multivariate regression analysis was carried out to correlate the dependent variables such as observed cloud heights and areas and their time rates of change with the independent variables such as vehicle engine parameters and meteorological variables.

Two types of regression equations were derived: (1) thrust-dominated regression equations, and (2) regression equations dominated by meteorological variables. Both types of equations were employed to yield predictions of cloud parameters. The predicted cloud parameters were then compared with those actually observed. Results of the comparisons are represented by the residual values between the predicted and the observed parameters computed for all cases available from observations.

Results of the comparisons show that, generally speaking, cloud heights and their rates of change with time can be adequately predicted with either type of regression equation and predictions of cloud areas and their rates of change with time are less satisfactory. However, it should be recognized that the number of data samples available to the analysis was limited, and that the derivation of regression equations was based on a limited number of data samples only.

2.4 Conclusions and Recommendations

2.4.1 Summary

In Section 2.1, a new and unique body of data on hot plume rise has been evolved, based on information generated by the George C. Marshall Space Flight Center in the course of its test firings of large rocket engines. Since other information in the field of hot plume rise characterizes plume rises from industrial stacks with relatively low temperatures and velocities, these data are unique in this field because they represent unusually high values of exhaust temperature and exit velocity. While the data have been employed extensively in the present study (both the theoretical and the empirical studies), their potential has by no means been exhausted, and investigators studying plume behavior from any source now have available and should use this fund of information.

2.4.2 Theoretical Treatment

The theory developed in Section 2.2 represents an expansion of concepts beyond that previously considered for hot plume rise from industrial stacks in order to allow for the extremes of exit velocity and temperature involved in the basic experimental data. As a result, the theory is applicable not only to this case, but also represents a more powerful and explicit treatment of the stack case and should be given attention in that field.

2.4.3 Statistical Treatment

The empirical treatment described in Section 2.3 was undertaken, both as an exploratory move to seek out significant parametric dependencies implicit in the data and to provide insurance that predictive methodologies, of some sort, could be generated in the event that the theoretical development was unable to adequately describe this unusual case. Since, however, the theoretical development was so successful, the statistical treatment has thus assumed a secondary role contributing primarily in the vein of identification of the significant parameters and providing predictions of some of the dependent variables to which the theory has not yet been applied.

2.4.4 Conclusions

From the Task I study, it is concluded that:

- A new body of hot plume rise data has been generated which extends into the realm of high temperatures and velocities not heretofore available;
- theoretical developments have been evolved which extend the capability of previous theoretical and empirical models for hot plume rise from industrial stacks to cover the high velocities and temperatures of rocket engine exhausts and also strengthen the stack's predictive capability; and
- empirical statistical analyses have been carried out which have identified significant controlling parameters in the hot plume rise.

2.4.5 Recommendations

- That the theoretical development be employed as the predicted model for the rise and growth of hot plumes from rocket engine exhausts, both for the prediction per se, and for application into diffusion and deposition expressions, as required for future rocket fuel program planning;
- that this model be made available for use by the scientific community concerned with hot plume rise from industrial stacks (primarily air pollution meteorologists) as a significant improvement in the state-of-the-art;
- that detailed meteorological data (such as wind, temperature, pressure, etc.) for the layer within which exhaust cloud rise takes place be used in future model calculations (heretofore, values of meteorological parameters averaged for the layer of cloud rise have been used);
- that more observation data on exhaust cloud rise be accumulated in the future, and that observed data with wider ranges of engine and exhaust gas parameters, and data on water injection onto the flame deflector be used to verify both the theoretical and empirical expressions for exhaust cloud rise prediction;
- that consideration be given to the incorporation of the effects of sprayed water on the exhaust cloud rise into the theoretical model as a further refinement; and
- that the new body of plume rise data generated from the MSFC test firings and presented in this report also be made available to the scientific community concerned with development and validation of hot plume rise models.

2.5 References

Briggs, G. A. 1969. Plume Rise. U. S. Atomic Energy Commission Critical Review Series, 81 pages.

Hage, K. D. and Bowne, N. E. 1965. Preliminary Estimates of Environmental Exposure for Fuel and Exhaust Products. National Aeronautics and Space Administration Report CR-61056.

Machta, L. 1950. "Entrainment and the Maximum Height of an Atomic Cloud." Bulletin of American Meteorological Society. Vol. 31. No. 6.

Morton, B. R., Taylor, G. and Turner, J. S. 1956. "Turbulent Gravitational Convection from Maintained and Instantaneous Sources." Proceedings of Royal Society of London.

Priestley, C. H. B. 1953. Buoyant Motion in a Turbulent Environment." Australian Journal of Physics. 6. pp. 279-290.

Priestley, C. H. B. 1956. "A Working Theory of the Bent-Over Plume of Hot Gas." Quarterly Journal of Royal Meteorological Society. 82. pp. 165-176.

Priestley, C. H. B. and Ball, F. K. 1955. "Continuous Convection from an Isolated Source of Heat." Quarterly Journal of Royal Meteorological Society. 81. pp. 144-157.

Railston, W. 1954. "The Temperature Decay Law of a Naturally Convected Airstream." Proceedings of Physics Society. Series B 67. pp. 42-51.

Rouse, H., Yih, C. S. and Humphreys, H. W. 1952. "Gravitational Convection from a Boundary Source." Tellus 4. pp. 201-210.

Spurr, G. 1957. "The Bent-Over Plume of Hot Gas." Quarterly Journal of Royal Meteorological Society. 83. p. 269.

Sutton, O. G. 1950. "Note on 'Entrainment and the Maximum Height of an Atomic Cloud,' by L. Machta." Bulletin of American Meteorological Society. Vol. 31. No. 6.

3.0 TASK II - DEBRIS FALLBACK AND FALLOUT MODEL FOR THE KSC LAUNCH AREA

3.1 Introduction

Task II of this contract addresses itself to the development of a computerized model describing the dispersion of material originating from normal or abnormal operations in the layer bounded from 5-30 km.

The development of models for atmospheric fallback and fallout is dependent upon the degree to which the atmospheric structure may be resolved. In the past, such models were based upon relatively low resolution measurement techniques. As the state-of-the-art advances, more sophisticated measurement techniques become available and the existing models become outdated. The development of the FPS-16 Radar-Jimsphere system, now in use at the KSC complex, is such a technique. The modification and/or development of new predictive models to match the advances of the measurement technology is dependent upon the real need for higher resolution models. The development of more powerful fuels, which are of a toxic nature, for use in NASA's propulsion systems has provided the need for the development of more refined predictive models. Of particular interest, is the dispersion of material after an abort at some point in the atmosphere.

The remainder of Section 3.0 is divided into three major parts: model formulation, programming, and documentation. The section on model formulation presents the equations used in the model with documentation on their origin, meaning, and justification. The Programming Guide includes a description of how the GEOMET formulation was incorporated with the existing 0-5 km program* and provides step by step instructions for use. The section on documentation of the program includes a description of required inputs and their calculation and program use.

---

* Developed by GCA for the Marshall Space Flight Center under Contracts NAS8-30503 and NAS8-21453.

3.2 Formulation of Models

The task of formulation has been broken down into component parts, each of which correspond to a definite physical situation. These parts, in turn, have been classified under the headings of diffusion models or deposition models according to their nature. A diffusion model involves the prediction of nonsettling material, while a deposition model predicts the ground pattern resulting from the settling of material which can be assigned a terminal velocity. The diffusion formulation involves the consideration of environmental problems such as effects of wind speed and directional shears on diffusion, transitions from one meteorological regime to another and the effects of washout, as well as source problems such as the effect of a missile's trajectory on subsequent diffusion and the effects of source decay as a function of time. The deposition formulation considers the same source problems and selected environmental problems. There is, however, one fundamental difference in the formulations. The diffusion formulation permits the investigation of the outputs as a function of time from release while the deposition models do not have this option.

3.2.1 Diffusion Models

Before discussing individual models and their origins, it is necessary to set up a preliminary framework. This involves the definition of the basic quantities which the diffusion models predict, the system of notation used, the definition of relevant coordinate systems, and the explanation of the model structure and the inputs necessary to define this structure.

The diffusion problem amounts to the prediction of concentration and dosage fields resulting from a source characterized by a known strength and geometry. The dimensions of source strength are dependent upon the source-geometry and are shown in Table 3-1 for future reference.

Table 3-1 Source strength dimensions

Geometry	Designation	Source Strength Dimension	Notation	Source Strength Units
point	P	M	Q_P	gm
line	L	M/L	Q_L	gm/meter
area	A	M/L^2	Q_A	$gm/meter^2$
volume	V	M/L^3	Q_V	$gm/meter^3$

The concentration field is generally a function of spatial and time coordinates with the dimensions of M/L^3 and units* of $gm/meter^3$. The notation for concentration is dependent upon the source-geometry and will be denoted by the Greek letter Chi (χ) followed by an appropriate source-geometry designation as a subscript (if no subscript appears the equation holds for all geometries). Dosage is defined as the time integral concentration

$$D = \int_0^t \chi dt \tag{3-1}$$

with dimensions of MT/L^3 and units of $gm\ sec/meter^3$. The same notation system which applies to concentration also applies to dosage. If the upper limit of integration in Equation (3-1) is set to ∞, the dosage obtained is termed total dosage; if $t<\infty$, the dosage obtained is termed partial dosage and is a function of time.

The structure of the model is based upon layers which are defined by the thermal stratification of the real atmosphere. The layer boundaries

---

*The units of mass in the model inputs are at the option of the user.

are assumed to be total reflectors of the diffusing material, which correspond to the inversions and stable regions found in the atmosphere.

Two coordinate systems have been used in developing the diffusion models. The first is a grid system in which a point is given by (X_G, Y_G, Z_G) with the positive X_G direction being east, the positive Y_G direction being north and with Z_G being the vertical coordinate as defined by the right-hand rule. The second is the standard meteorological system for diffusion calculations, which is defined independently for each layer in the 5-30 km region. In any layer of this region, the origin of the system is given by the intersection of the vehicle's trajectory with the bottom boundary of that layer. Since the wind is not restricted to be constant with height within a layer, the X (alongwind) direction is defined to be along the mean wind in the layer, the Z (vertical) direction corresponds to that used in the grid system, and the Y (lateral) direction is defined by the right-hand rule. The wind direction (θ_k) and speed (U_k) at both boundaries of a layer are required as inputs and are used to calculate the mean wind by taking a vector average. Thus, if the additional subscripts T and B signify the top and boundary respectively, the mean wind speed ($\overline{U}_k$) and direction ($\overline{\theta}_k$) are given by

$$\overline{U}_k = \frac{1}{2} (k_1{}^2 + k_2{}^2)^{1/2} \tag{3-2}$$

$$\overline{\theta}_k = \arctan \left[\frac{k_1}{k_2} \right] \tag{3-3}$$

where

$$k_1 = U_{kT} \sin (270-\theta_{kT}) + U_{kB} \sin (270-\theta_{kB}) \tag{3-4}$$

and

$$k_2 = U_{kT} \cos (270-\theta_{kT}) + U_{kB} \cos (270-\theta_{kB}) \tag{3-5}$$

where k_1 and k_2 are the components of the vector sum on the Y_G and X_G axis respectively. Figure 3-1 illustrates the relationship of the meteorological coordinate system of the k^{th} layer to the grid system.

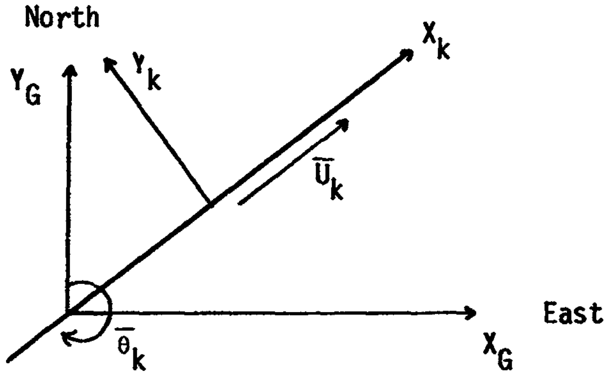

Figure 3-1 The relationship between the grid and meteorological coordinate systems

3.2.1.1 Inclined Line Models for the k^{th} Layer

3.2.1.1.1 Concentration and Dosage

These models account for the effect of the vehicle's trajectory on the subsequent dosage and concentration fields within a specified layer. The model for the 0-5 km region assumes that the vehicle's trajectory is vertical. Rough data on the planned trajectories of Apollo missions indicate that for 0-5 km this assumption is justified; however, in terms of the 5-30 km region, this assumption becomes tenuous. At a height of 30 km the vehicle is on the order of 25 km downrange. Integration of a point source model along the trajectory within a layer was used to obtain an analytical solution under the assumptions that the trajectory within the layer is defined by a straight inclined line and that diffusion is a Gaussian process. Figure 3-2 illustrates the vehicle trajectory with reference to the meteorological coordinate system.

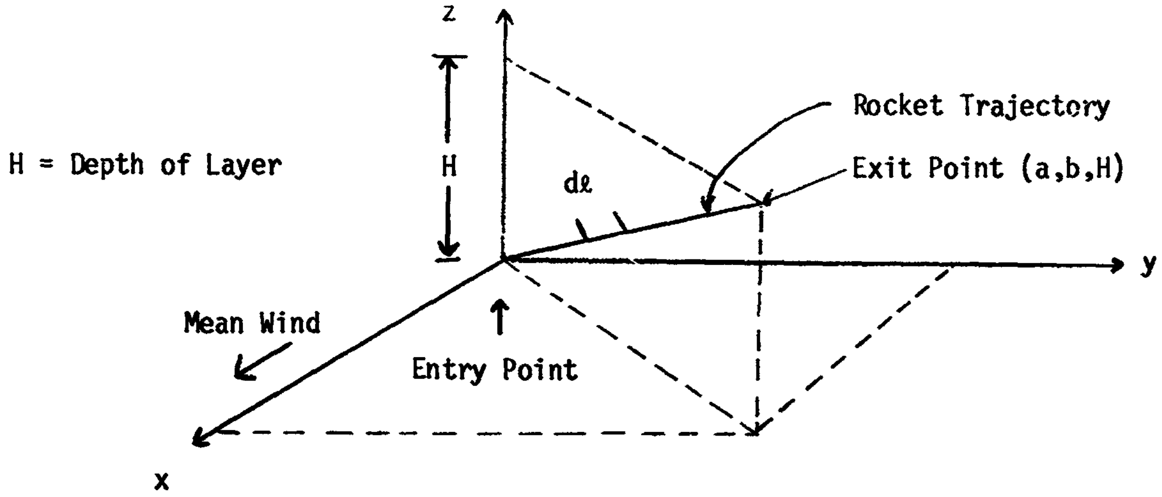

Figure 3-2 Rocket trajectory in k^{th} layer

The trajectory is defined by the rocket's exit point from the k^{th} layer and its equation is given by

$$\frac{x_1}{a} = \frac{y_1}{b} = \frac{z_1}{H} \tag{3-6}$$

where the point (a,b,H) is the exit point of the trajectory from the layer in the meteorological system; H is, therefore, the thickness of the layer. The required integration is given by

$$x_L = \int_0^{k_1} x_p \, d\ell \tag{3-7}$$

where the upper limit of integration is given by

$$k_1 = (a^2 + b^2 + H^2)^{1/2} . \tag{3-8}$$

Using the assumption that diffusion is Gaussian, we may express χ_p as

$$\chi_p = \frac{Q_p}{(2\pi)^{3/2}\,\sigma_x\sigma_y\sigma_z} \exp - \frac{1}{2}\left\{\left(\frac{x-\bar{u}_k t-x_1}{\sigma_x}\right)^2 + \left(\frac{y-y_1}{\sigma_y}\right)^2\right\}(\text{vertical term}) \tag{3-9}$$

where

t = time of evaluation,

Q_p = source strength,

$\sigma_x,\sigma_y,\sigma_z$ = standard deviations of cloud material in the x,y and z direction (see Section 3.2.1.2 for formulation), and

(x,y,z) = the coordinates of the receptor point in the meteorological system.

The vertical term is derived from the assumption made about total reflection at the layer boundaries:

$$\text{vertical term} = \sum_{m=0}^{\infty} \exp - \frac{1}{2}\left\{\left(\frac{2mH+z_1-z}{\sigma_z}\right)^2 + \exp - \frac{1}{2}\left(\frac{-2mH+z+z_1}{\sigma_z}\right)^2 + \exp - \frac{1}{2}\left(\frac{-2(m+1)H+z_1-z}{\sigma_z}\right)^2 + \exp - \frac{1}{2}\left(\frac{2(m+1)H+z_1+z}{\sigma_z}\right)^2\right\}. \tag{3-10}$$

This expression is obtained by modeling each reflection by placing a virtual point source on a vertical line through the original source. Four terms are necessary because of the asymmetry caused by placing the release point closer to one boundary. The second and third terms describe subsequent reflections (off of the upper and lower boundary respectively) resulting from the first reflection from the upper boundary. The first and fourth terms describe subsequent reflections (off of the upper and lower boundary respectively) resulting from the first reflection from the lower boundary. Equation (3-10) is a basic extension of the vertical term given by Slade (1968, p.348) for the capping inversion and eliminates the requirement that the bottom boundary coincide with the ground.

The integration indicated in (3-7) may be done with respect to either x_1, y_1, z_1, or ℓ since

$$\ell^2 = x_1{}^2 + y_1{}^2 + z_1{}^2. \tag{3-11}$$

The height of the point source z_1, was selected as the variable of integration. Eliminating x_1 and y_1 from (3-11) by the use of (3-6) yields

$$\ell = \left(\frac{a^2}{H^2} + \frac{b^2}{H^2} + 1\right)^{1/2} z_1 \tag{3-12}$$

and (3-7) becomes

$$x_L = \int_0^H x_p \alpha dz_1 \tag{3-13}$$

where

$$\alpha = \left(\frac{a^2}{H^2} + \frac{b^2}{H^2} + 1\right)^{1/2}. \tag{3-14}$$

The vertical term (3-10) may be written more concisely by letting

$$w_1 = -2mH+z \tag{3-15}$$

$$w_2 = -w_1 \tag{3-16}$$

$$w_3 = 2(m+1)H+z \tag{3-17}$$

$$w_4 = -w_3 \tag{3-18}$$

thus

$$\text{vertical term} = \sum_{m=o}^{\infty} \sum_{j=1}^{4} \exp - \frac{1}{2} \left(\frac{z_1 - w_j}{\sigma_z}\right)^2. \tag{3-19}$$

Placing this in (3-13) yields

$$\chi_L = \int_o^H \frac{Q_p}{(2\pi)^{3/2}\,\sigma_x\sigma_y\sigma_z} \exp -\frac{1}{2}\left\{\left(\frac{x-u_k t-\eta z_1}{\sigma_x}\right)^2 + \left(\frac{y-\tau z_1}{\sigma_y}\right)^2\right\}$$

$$\sum_{m=o}^{\infty}\ \sum_{j=1}^{4} \exp -\frac{1}{2}\left(\frac{z_1-w_j}{\sigma_z}\right)^2 \alpha\, dz_1 \qquad (3\text{-}20)$$

where

$$\eta = \frac{a}{H} \qquad (3\text{-}21)$$

and

$$\tau = \frac{b}{H}\,. \qquad (3\text{-}22)$$

Removing constant terms and interchanging the integral and summation yields

$$\chi_L = \frac{Q_L\alpha}{(2\pi)^{3/2}\,\sigma_x\sigma_y\sigma_z} \sum_{m=o}^{\infty}\ \sum_{j=1}^{4} \int_o^H \exp -\frac{1}{2}\left[\left(\frac{\bar{x}-\eta z_1}{\sigma_x}\right)^2\right.$$

$$\left. + \left(\frac{y-\tau z_1}{\sigma_y}\right)^2 + \left(\frac{z_1-w_j}{\sigma_z}\right)^2\right] dz_1 \qquad (3\text{-}23)$$

where

$$\bar{x} = x - \bar{u}_k t. \qquad (3\text{-}24)$$

The exponent is expanded in terms of z_1 resulting in a second degree polynominal. After completing the square and removing constants from the integral we have

$$\chi_L = \frac{Q_L\alpha}{(2\pi)^{3/2}\,\sigma_x\sigma_y\sigma_z} \sum_{m=o}^{\infty}\ \sum_{j=1}^{4} \left\{\exp -\frac{1}{2}\left(\frac{\bar{x}^2}{\sigma_x^{\,2}} + \frac{y^2}{\sigma_y^{\,2}} + \frac{w_j^{\,2}}{\sigma_z^{\,2}} - \frac{B^2}{A^2}\right)\right.$$

$$\left.\int_o^H \exp -\frac{1}{2}\left(z_1 A - \frac{B}{A}\right)^2 dz_1\right\} \qquad (3\text{-}25)$$

where

$$A^2 = \frac{\eta^2}{\sigma_x{}^2} + \frac{\tau^2}{\sigma_y{}^2} + \frac{1}{\sigma_z{}^2} \tag{3-26}$$

$$B = \frac{\eta\bar{x}}{\sigma_x{}^2} + \frac{\tau y}{\sigma_y{}^2} + \frac{w_j}{\sigma_z{}^2} . \tag{3-27}$$

By means of the substitution

$$\psi = \left(z_1 A - \frac{B}{A}\right) 2^{-1/2}. \tag{3-28}$$

The integral in (3-25) may be expressed in terms of the error function:

$$\chi_L = \frac{Q_L \alpha}{(2\pi)^{3/2}\,\sigma_x \sigma_y \sigma_z} \sum_{m=o}^{\infty} \sum_{j=1}^{4} \left\{ \frac{\sqrt{.5\pi}}{A} \exp - \frac{1}{2}\left(\frac{\bar{x}^2}{\sigma_x{}^2} + \frac{y^2}{\sigma_y{}^2} + \frac{w_j{}^2}{\sigma_z{}^2} - \frac{A^2}{B^2}\right) \right.$$

$$\left. \left[\operatorname{erf}\left(\frac{HA^2-B}{\sqrt{2}\,A}\right) + \operatorname{erf}\left(\frac{B}{\sqrt{2}\,A}\right)\right] \right\} \tag{3-29}$$

where

$$\operatorname{erf}(x) = \frac{2}{\sqrt{\pi}} \int_0^x e^{-t^2} dt. \tag{3-30}$$

Equation (3-29) represents the formulation for an inclined line extending completely through the k^{th} layer. This equation may be simplified by removing a factor of $\sqrt{.5\pi}/A$ from the infinite series, however, (3-29) represents the manner in which the model was programmed with the infinite series being evaluated independently of the multiplicative factor involving Q_L. Equation (3-29) represents diffusion from a normal launch through the layer.

Abortive launches are modeled by superposition of a line source and a point source. In this case, the line may end anywhere in the k^{th} layer, and Equation (3-29) must be modified to account for this. The upper limit in Equation (3-23) is changed to H_a, the height of the abort after stabilization (no connective motion in cloud) relative to the meteorological origin in the k^{th} layer. Thus,

$$H_a < H \tag{3-31}$$

and the first error function in (3-29) becomes

$$\mathrm{erf}\left(\frac{H_a A^2 - B}{\sqrt{2}\, A}\right). \tag{3-32}$$

The formulation for dosage corresponding to an inclined line source is derived in a similar manner. A straightforward approach is to apply Equation (3-1):

$$D_L = \int_0^t \chi_L \, dt. \tag{3-33}$$

To obtain an analytic solution, integrals of the form,

$$\int_0^t \exp - (At + B)^2 \; \mathrm{erf}\,(c + Dt)\, dt \tag{3-34}$$

must be evaluated. Since no analytic solution of (3-34) was known to the authors, another approach was used. This entailed rewriting (3-33) as

$$D_L = \int_0^t \int_0^H \chi_p \, \alpha dz_1 \, dt. \tag{3-35}$$

Since the variables of integration are independent, the order of integration may be interchanged. In doing this, we find

$$D_L = \int_0^H \alpha D_p \, dz_1 . \tag{3-36}$$

By using the same methods as those mentioned previously, D_p may be shown to be

$$D_p = \frac{Q_p}{2^2 \pi \sigma_y \sigma_z \bar{u}_k} \exp - \frac{1}{2}\left(\frac{y-\tau z_1}{\sigma_y}\right)^2 \left[\operatorname{erf}\left(\frac{x-\eta z_1}{\sqrt{2}\,\sigma_x}\right) - \operatorname{erf}\left(\frac{x-\bar{u}_k t-\eta z_1}{\sqrt{2}\,\sigma_x}\right)\right]$$

$$\sum_{m=o}^{\infty} \sum_{j=1}^{4} \exp - \frac{1}{2}\left(\frac{z_1-w_j}{\sigma_z}\right)^2 . \qquad (3\text{-}37)$$

Even though the evaluation of (3-36) still involves integrals in the form given in (3-34), some simplifying assumptions may now be made. If we restrict ourselves to looking at total dosage, $t \to \infty$ and

$$-\operatorname{erf}\left(\frac{x-\bar{u}_k t-\eta z_1}{\sqrt{2}\,\sigma_x}\right) = 1 \qquad (3\text{-}38)$$

and if $\quad x \gg \sqrt{2}\,\sigma_x + \eta z_1 + \bar{u}_k t \qquad (3\text{-}39)$

then $\quad \operatorname{erf}\left(\frac{x-\bar{u}_k t-\eta z_1}{\sqrt{2}\,\sigma_x}\right) \approx 1. \qquad (3\text{-}40)$

The evaluation of (3-36) is now straightforward and we find that

$$D_L = \left[\frac{\alpha Q_L}{2\pi \sigma_y \sigma_z \bar{u}_k}\right] \sum_{m=o}^{\infty} \sum_{j=1}^{4} \left[\frac{\sqrt{.5\pi}}{F} \exp - \frac{1}{2}\left(\frac{(y+w_j\tau)^2}{\sigma_z^2\tau^2+\sigma_y^2}\right)\right.$$

$$\left.\operatorname{erf}\left(\left[\frac{HF^2+G}{\sqrt{2}\,F}\right] - \operatorname{erf}\left[\frac{G}{\sqrt{2}\,F}\right]\right)\right] \qquad (3\text{-}41)$$

where

$$F^2 = \frac{\tau^2}{\sigma_y^2} + \frac{1}{\sigma_z^2} \qquad (3\text{-}42)$$

$$G = \frac{w_j}{\sigma_z^2} - \frac{\tau y}{\sigma_y^2} . \qquad (3\text{-}43)$$

In the case of a vertical line through the layer (a=o, b=o), the restriction given by (3-39) may be dropped because the argument of the error function is no longer a function of z_1 (η=o). For this special case, (3-36) becomes D_L^* where

$$D_L^* = \frac{D_L}{2}\left[1 + \text{erf}\left[\frac{x-\bar{u}_k t}{\sqrt{2}\,\sigma_x}\right]\right] . \qquad (3\text{-}44)$$

This indicates, and is confirmed by numerical results, that Equation (3-41) is too large by a factor of two when $x = \bar{u}_k t$ and greater amounts when $x<\bar{u}_k t$. This suggests that better estimates of dosage for small values of x can be obtained by multiplying (3-41) by a factor similar to that found in (3-44).

$$v = .5\left[1 + \text{erf}\left[\frac{x-\bar{u}_k t-\eta\bar{z}_1}{\sqrt{2}\,\sigma_x}\right]\right] . \qquad (3\text{-}45)$$

The mean value theorem indicates that an appropriate factor is given by Equation (3-45), where $o \leq \bar{z}_1 \leq H$. For the purpose of testing, the correction, $\bar{z}_1$, was set equal to the height of the receptor. While giving exact results for η=o, in the more general case ($\eta \neq$ o), the correction factor gave anomalous values in certain special regions where the definition for $\bar{z}_1$ was apparently not consistent with the geometry of the line source. Because of this, it was not possible to incorporate the correction factor into the operational model. Equation (3-45), however, can be used with various estimates of $\bar{z}_1$ to estimate the error in the dosage in regions where Equation (3-39) is not satisfied.

The equations for the point source to be used in conjunction with the limited inclined source equations have already been cited or derived. The equations for concentration and dosage are given by (3-9) and (3-37). The total concentration and dosage for an alert are given by

$$\chi_{AT} = \chi_L + \chi_p \tag{3-46}$$

and

$$D_{AT} = D_L + D_p . \tag{3-47}$$

3.2.1.1.2 Source Strength

The variable speed of the vehicle along its trajectory presents the interesting problem of defining the source strength Q_L. If the engine is operating in a steady-state mode, then Q_L is an inverse function of speed. This is seen from

$$\dot{m} = \frac{dm}{dt} = \frac{dm}{d\ell}\frac{d\ell}{dt} = \text{constant} \tag{3-48}$$

where $\dot{m}$ is the mass flow rate, $\frac{d\ell}{dt}$ is the speed of the vehicle along its trajectory and $\frac{dm}{d\ell} = Q_L$. In terms of input to the model, Q_L must be an average value of $\frac{dm}{d\ell}$ over the entire layer; thus

$$Q_L = \frac{1}{H}\int_0 \frac{dm}{d\ell}\, dz \tag{3-49}$$

$$Q_L = \frac{1}{H}\int_0^H \frac{\dot{m}}{H}\frac{dz}{v(z)} \tag{3-50}$$

Transforming this to the vertical coordinates of the grid system, we have

$$Q_L = \int_{z_{k_B}}^{z_{k_t}} \frac{\dot{m}}{H}\frac{dz}{v(z)} \tag{3-51}$$

where $v(z)$ is the velocity of the vehicle along its trajectory and z_{k_t} and z_{k_B} are the vertical positions of the top and bottom of the k^{th} layer respectively. It is suggested that the user calculate values of Q_L for each layer by use of (3-51) (see Section 3.3.4).

3.2.1.1.3 Output Parameters

The output parameters for the preceding models are concentration, peak concentration, and dosage. Peak concentration is calculated from the model for concentration at time t_p, which is calculated internally by the program and is given by

$$t_p = \frac{\overline{x}}{\overline{u}_k}. \tag{3-52}$$

Physically, this is equivalent to saying that the peak or maximum concentration occurs when the centroid of the cloud is closest the assessment point. Concentration can be calculated at times specified by the user. All these outputs can be calculated at points in space specified by the user. For detailed instructions on inputs, outputs, and program options, the reader is referred to Sections 3.3 and the Programming Guide.

3.2.1.2 The Calculation of σ_x, σ_y and σ_z in Shear Flow

The effects of velocity shear on diffusion were first noted by Taylor (1953, 1954) for both laminar and turbulent pipe flow. He observed an accelerated rate of diffusion of material in regions of shear and showed that the diffusivity needed to bring about this effect (termed effective diffusivity) was much greater than turbulent or molecular diffusivities. Taylor estimated this effective diffusivity by imposing a constant concentration gradient in the direction of the mean flow and by calculating the resulting flux of material. Aris (1956), a chemical engineer, developed another approach for the calculation of effective diffusivity called the product moment method. Saffman (1962) applied this method to the prediction of atmospheric diffusion in shear flows. Hogstrom (1964) and Smith (1965), using statistical methods, have confirmed Saffman's results. More recently, Tyldesley and Wallington (1965), Gee (1967) and Csanady (1969) have used this method to describe the effects of shear flow on diffusion.

The concentration moment method is based on reducing the diffusion equation to a series of simplified differential equations involving the moments of the concentration distribution. Saffman has obtained asymptotic solutions for both bounded and unbounded flows. Following Saffman, the basic results of this method are reviewed below. The moments of the concentration field are defined by

$$\theta_{nm}(z,t) = \int_{-\infty}^{\infty}\int_{-\infty}^{\infty} x^n y^m \chi dxdy \quad (n\geq o,\ m\geq o) \tag{3-53}$$

and as the notation indicates, are functions of height and time. Differential equations involving these moments are obtained from the diffusion equation:

$$\frac{\partial\chi}{\partial t} + u_k \frac{\partial\chi}{\partial x} + v_k \frac{\partial\chi}{\partial y} = \frac{\partial\chi}{\partial x}(k_x \frac{\partial\chi}{\partial x}) + \frac{\partial\chi}{\partial y}(k_y \frac{\partial\chi}{\partial y}) + \frac{\partial\chi}{\partial z}(k_z \frac{\partial\chi}{\partial z}) \tag{3-54}$$

with boundary conditions of

$$\frac{\partial\chi}{\partial z} = o \text{ at } z=o \text{ and } H \tag{3-55}$$

and $\chi \to o$ as $x\to\infty$, $y\to\infty$ (3-56)

with the assumptions that the eddy diffusivities k_x, k_y and k_z are independent of x, y, and t, and that the mean wind is parallel to the ground and a function of height only. The multiplication of (3-54) by $x^n y^m$ and integration over the xy plane results in differential equations for the moments θ_{nm}. If the concentration is normalized in such a way that the source strength within a layer is unity, it follows that

$$\int_{0}^{H}\int_{-\infty}^{\infty}\int_{-\infty}^{\infty} \chi dxdydz = 1. \tag{3-57}$$

This allows the total variance of the cloud in the x and y directions to be defined in terms of moments for the total cloud (Θ_{nm}) as follows:

$$\sigma_x^2 = \Theta_{20} - \Theta_{10}^2 \tag{3-58}$$

and

$$\sigma_y^2 = \Theta_{02} - \Theta_{01}^2 \quad . \tag{3-59}$$

where in general

$$\Theta_{nm} = \int_o^H \theta_{nm} \, dz. \tag{3-60}$$

The differential equations for θ_{oo}, θ_{10} and θ_{20} can be found by multiplying the diffusion equation by 1, x and x^2 respectively and integrating over the xy plane. This procedure in conjunction with the boundary condition given by (3-55) results in

$$\frac{\partial \theta_{oo}}{\partial t} = \frac{\partial}{\partial z} (k_z \frac{\partial \theta_{oo}}{\partial z}) \tag{3-61}$$

$$\frac{\partial \theta_{10}}{\partial t} - u_k \theta_{on} = \frac{\partial}{\partial z} (k_z \frac{\partial \theta_{10}}{\partial z}) \tag{3-62}$$

$$\frac{\partial \theta_{20}}{\partial t} - 2u_k \theta_{10} = 2k_x \theta_{oo} + \frac{\partial}{\partial z} (k_z \frac{\partial \theta_{20}}{\partial z}) \tag{3-63}$$

with boundary conditions that

$$\frac{\partial \theta_{no}}{\partial z} = o, \ z = o, \ z = H \ (n = 0, 1, 2). \tag{3-64}$$

This system of equations with suitable initial conditions determines σ_x and σ_y. The initial conditions for this system are determined when concentration is specified at time t=o

$$x \Big|_{t=o} = f(x, y, z) \tag{3-65}$$

where f(x, y, z) is a function describing the initial character of the source. From (3-65) and (3-53) it follows that

$$\theta_{no}\Big|_{t=o} = \int_{-\infty}^{\infty}\int_{-\infty}^{\infty} x^n \ f(x,\ y,\ z)\ dxdy. \tag{3-66}$$

The second step in the analysis is the specification of f(x, y, z). In particular, this function must account for reflection from the layer boundaries and edge effects if the source is a line. Since the system of equations is independent of x and y, the inclination of the line source with respect to the vertical will not enter into the solution and the assumption of a vertical line source will not reduce the generality of the solution. It is assumed, therefore, that the initial distribution of mass within the cloud is uniformly distributed along a vertical line. It then follows that f(x, y, z) is given by

$$f(x,\ y,\ z) = \sum_{m=o}^{\infty} \sum_{j=1}^{4} \left\{ \frac{\sqrt{.5\pi}}{A} \exp - \frac{1}{2}\left[\left[\frac{x}{\sigma_{xs}}\right]^2 + \left[\frac{y}{\sigma_{ys}}\right]^2\right] \right.$$

$$\left. \left[\operatorname{erf}\left[\frac{HA^2-B}{\sqrt{2}\ A}\right] + \operatorname{erf}\left[\frac{B}{\sqrt{2}\ A}\right]\right] \right\} \frac{1/H}{(2\pi)^{3/2}\ \sigma_{xs}\sigma_{ys}\sigma_{zs}} \tag{3-67}$$

where

σ_{xs} = standard deviation of source along x direction,

σ_{ys} = standard deviation of source along y direction,

σ_{zs} = standard deviation of source along z direction,

$A = 1/\sigma_{zs}$,

$B = \frac{w_j}{\sigma_{zs}^2}$, and

w_j = see Equations (3-15) - (3-18).

The expansion of (3-67) results in the following equation for f(x, y, z):

$$f(x, y, z) = \frac{1/H}{2\pi\sigma_{xs}\sigma_{ys}} \exp - \frac{1}{2}\left[\left[\frac{x}{\sigma_{xs}}\right]^2 + \left[\frac{y}{\sigma_{ys}}\right]^2\right] \tag{3-68}$$

which indicates that a vertical line source in a bounded layer is theoretically equivalent to an infinite line in an unbounded region. Using this result, the initial conditions for the system of equations can be shown to be

$$\theta_{oo}\Big|_{t=o} = 1/H \tag{3-69}$$

$$\theta_{10}\Big|_{t=o} = o \tag{3-70}$$

$$\theta_{20}\Big|_{t=o} = \frac{\sigma_{xs}{}^2}{H} \tag{3-71}$$

where $\sigma_{xs}{}^2$ is the initial variance of the cloud in the x direction.

The third and final step of the analysis is the solution of the system of equations for the boundary and initial conditions derived above. The logical procedure is to begin with the lower moments and work through to the higher moments. For a constant $k_z = k$ and the use of the finite cosine transform, it follows that

$$\theta_{oo} = \frac{1}{H} + \frac{2}{H}\sum_{n=1}^{\infty}\hat{\theta}_{oo} \exp\left(-\frac{n^2\pi^2kt}{H^2}\right) \cos\frac{n\pi z}{H} \tag{3-72}$$

where $\hat{\theta}_{oo}$ is the finite cosine transform of $\theta_{oo}\Big|_{t=o}$, i.e.,

$$\hat{\theta}_{oo} = \int_0^H \theta_{oo}\Big|_{t=o} \cos\frac{n\pi z}{H}\, dz. \tag{3-73}$$

Saffman suggests that for arbitrary initial conditions, θ_{oo} asymptotically approaches the solution given by

$$\theta_{oo} \sim \frac{1}{H} \tag{3-74}$$

and is subject to the condition that

$$t >> H^2/2k. \tag{3-75}$$

The result given by (3-74) is easily verified by letting t approach infinity in Equation (3-72). The condition for asymptoticity stems from an analysis of the value of the exponential term in the infinite series. While (3-75) is a good rule of thumb, it is not applicable to the results of the present analysis. This follows directly from the initial condition (3-69) and its finite cosine transformation which is identically zero for all n greater than zero. Placing this result in (3-72) yields

$$\theta_{oo} = \frac{1}{H} \tag{3-76}$$

which is valid for all t greater than or equal to zero regardless of the implications of Equation (3-75). This result, however, does not assure that Saffman's asymptotic solutions to (3-62) and (3-63) are valid for small t. During the term of the contract, considerable effort was put forth in an attempt to find solutions for all t using methods of the Laplace transform. While workable with suitable assumptions about the variation of u_k and v_k with height, this method requires that the inverse transform of untabulated functions be found. In this case, use of the finite cosine transformation provides an easy and straightforward solution for the total cloud variance. The method of solution and major results are outlined below:

1. Equation (3-62) is integrated over the diffusing layer and the resulting differential equation is solved for θ_{10} which results in

$$\theta_{10} = \overline{u}_k t = \int_0^H \theta_{10}\, dz \tag{3-77}$$

indicating that the centroid of the cloud moves with mean velocity of the layer.

2. Equation (3-76) is substituted in (3-62), k_z* is assumed to be independent of height and the finite cosine transform is applied. The resulting ordinary first-order differential equation is solved for the transform of θ_{10} ($F_c(\theta_{10})$), which results in

$$F_c(\theta_{10}) = \frac{H^2}{n^2\pi^2 k_z} F_c\left(\frac{u_k}{H}\right). \tag{3-78}$$

3. The inversion formula for the finite cosine transform is applied to Equation (3-78) yielding a solution for θ_{10}:

$$\theta_{10} = \frac{\overline{u}_k t}{H} + \frac{2}{\pi^2 k_z} \sum_{n=1}^{\infty} \frac{F_c(u_k)}{n^2} \cos \frac{n\pi z}{H}. \tag{3-79}$$

4. The variation of u is assumed to be linear within the diffusing layer, i.e.,

$$u_k = \hat{a}_k z + \hat{b}_k \tag{3-80}$$

so that

$$F_c(u) = \frac{\hat{a}_k H^2}{n^2\pi^2} [\cos n\pi - 1]. \tag{3-81}$$

5. Integration of (3-26) over the diffusing layer yields

$$\frac{d\theta_{20}}{dt} = 2\hat{a}_k \int_0^H u_k \theta_{10} dz + 2\hat{b}_k \overline{u}_k t + 2k_x\,. \tag{3-82}$$

---

* k_z is assumed to be equal to 10^5 and 10^3 cm²/sec for the troposphere and stratosphere respectively.

The integral is easily evaluated by use of (3-79), (3-80) and (3-81) which results in

$$\frac{d\Theta_{20}}{dt} = \hat{a}_k\bar{u}_k tH + \frac{4\hat{a}_k{}^2H^4}{\pi^6 k}\sum_{n=1}^{\infty}\frac{1}{(2n-1)^6} + 2\hat{b}_k\bar{u}_k t + 2k_x. \qquad (3\text{-}83)$$

6. Equation (3-83) is solved for Θ_{20} and the infinite series is evaluated in terms of Bernoulli numbers by use of the identity:

$$\sum_{n=1}^{\infty}\frac{1}{(2n-1)^6} = \frac{B_3\pi^6(2^6-1)}{2\cdot 6!} \qquad (3\text{-}84)$$

where B_3 is the third Bernoulli number. Thus,

$$\Theta_{20} = \Theta_{20}\Big|_{t=o} + \frac{\hat{a}_k\bar{u}_k t^2 H}{2} + \frac{\hat{a}^2H^2t}{171.42\ k_z} + \hat{b}\bar{u}_k t^2 + 2k_x t \qquad (3\text{-}85)$$

from which it follows that (see Equation (3-58))

$$\sigma_x{}^2 = \Theta_{20}\Big|_{t=o} + \frac{\hat{a}_k{}^2H^2t}{171.42\ k_z} + 2k_x t. \qquad (3\text{-}86)$$

If $v_k = c_k z + d$, then by analogy we have

$$\sigma_y{}^2 = \Theta_{02}\Big|_{t=o} + \frac{c_k{}^2H^2t}{171.42\ k_z} + 2k_y t. \qquad (3\text{-}87)$$

From Equation (3-71) it follows that

$$\Theta_{20}\Big|_{t=o} = \sigma_{xs}{}^2 \qquad (3\text{-}88)$$

and by analogy that

$$\Theta_{02}\Big|_{t=o} = \sigma_{ys}{}^2. \qquad (3\text{-}89)$$

Equations (3-86) and (3-87) provide the basis for the treatment of the effects of wind shear on diffusion and have been derived in the meteorological coordinate system. These equations may be related to the grid system by use of the following:

$$\hat{a}_k = u_{kT} \cos (\bar{\theta}_k - \theta_{kT}) - u_{kB} \cos (\bar{\theta}_k - \theta_{kB}) \qquad (3\text{-}90)$$

and

$$c_k = u_{kT} \sin (\bar{\theta}_k - \theta_{kT}) - u_{kB} \sin (\bar{\theta}_k - \theta_{kB}) \qquad (3\text{-}91)$$

where the notation is defined in Section 3.2.1.

In practice, the term $2k_x t$ may be equated to the variance of a point source (${}_p\sigma_x{}^2$) by use of the k theory:

$${}_p\sigma_x{}^2 = 2k_x t. \qquad (3\text{-}92)$$

In the operational model the sum given by

$${}_p\sigma_x{}^2 + \sigma_{xs}{}^2 \qquad (3\text{-}93)$$

has been replaced by a single virtual point source term given by

$$\sigma_y{}^2 = \sigma_{yr}{}^2 \left[\frac{x + x_y}{r_y}\right]^{2\alpha} \qquad (3\text{-}94)$$

where

$$x_y = r_y \left[\frac{\sigma_{ys}}{\sigma_{yr}}\right]^{1/\alpha} \qquad (3\text{-}95)$$

r_x, r_y, r_z = reference distances,

x_x, x_y, x_z = virtual distances,

$\sigma_{xr}, \sigma_{yr}, \sigma_{zr}$ = diffusion parameters,

$\sigma_{xs}{}^2, \sigma_{ys}{}^2, \sigma_{zs}{}^2$ = source variance at time t=o, and

α, β, γ = power law exponents.

Analogous substitutions have been made in Equation (3-87). Since vertical wind shear does not effect the vertical variance of the cloud, σ_z is given by

$$\sigma_z = \sigma_{zr} \left[\frac{x + x_z}{r_z}\right]^{\beta} \tag{3-96}$$

where

$$x_z = r_z \left[\frac{\sigma_{zs}}{\sigma_{zr}}\right]^{1/\beta} . \tag{3-97}$$

The program requires inputs of σ_{xs}, σ_{ys}, α, and β in each layer for both the line and point source formulation. The reference distances and diffusion parameters are set within the program as follows:

$$r_x = 100 \tag{3-98}$$

$$r_y = 20 \tag{3-99}$$

$$r_z = 20 \tag{3-100}$$

$$\sigma_{y,r_y} = 3.41 \tag{3-101}$$

$$\sigma_{z,r_z} = 1.35 \tag{3-102}$$

$$\sigma_{x,r_x} = \begin{cases} 238.57 \exp(-3.5878\,\beta) & .88 \leq \beta \leq .909 \\ 371.99 \exp(-4.0925\,\beta) & .851 \leq \beta \leq .88 . \end{cases} \tag{3-103}$$

β and α are functions of atmospheric stability and may be estimated from the following relationship

$$\alpha = \beta = .88 - 1.08\,\overline{\frac{dT}{dz}} \tag{3-104}$$

where

$\overline{\frac{dT}{dz}}$ = average temperature gradient in degrees centigrade for the k^{th} layer.

In the case of the inclined line source, $\sigma_{z,s}$ obviously cannot be measured, but because of the mechanics of the model, it is still needed as an input. The integration physically corresponds to moving a point source with source standard deviations $\sigma_{x,s}$, $\sigma_{y,s}$ and $\sigma_{z,s}$ along the line and summing the effects of each point source. In the special case of a vertical line source, the formulation reduces to a set of equations which are independent of $\sigma_{z,s}$. This, however, does not hold for the general case. $\sigma_{z,s}$ then must be defined in terms of $\sigma_{x,s}$ and $\sigma_{y,s}$. Through arguments of symmetry one would expect

$$\sigma_{x,s} \simeq \sigma_{y,s}. \tag{3-105}$$

A suitable definition would then be

$$\sigma_{z,s} = \frac{\sigma_{x,s} + \sigma_{y,s}}{2}. \tag{3-106}$$

3.2.1.3 The Effects of Washout and Decay

The effects of washout and decay are modeled as an exponential damping term which indicates the expected reduction due to these depletion processes as a function of time :

$$\hat{\chi} = \begin{cases} \chi \exp\,(-\,\gamma_D t - \gamma_W (t-t_1)) & t > t_1 \\ \chi \exp\,(-\,\gamma_D t) & t \le t_1 \end{cases} \tag{3-107}$$

where

t = travel time of cloud in seconds,

t_1 = time in seconds that precipitation begins,

γ_D = decay coefficient in %/sec,

γ_W = washout coefficient in %/sec,

χ = expected concentration without decay and washout, and

$\hat{\chi}$ = expected concentration with decay and washout.

Dosage is treated in an analogous manner using the same exponential damping term as concentration. For information regarding the specifications of the inputs required (t_1,γ_D and γ_W), the reader is referred to Section 3.3.6.

3.2.1.4 Meteorological Transition Model

In essence, this model is built upon a reapplication of the techniques used in the 0-5 km model to the case of diffusion from an inclined line source. The model considers the case of full transition and is thus valid for all times after transition. Since this model approaches the standard box model for large t, there is no need to consider a box model separately.

The transition is characterized by a change in layer structure, wind velocity and thermal gradient at time t*. For times after t*, the cloud is not assumed to be adjusted to the meteorological transition. In the following material, grid system coordinates will be used.

Let the points (x_{rk}, y_{rk}, z_{Bk}) and (x_i, y_i, z_i) represent the coordinates of the missile's entry point to the k^{th} layer and coordinates of the receptor respectively.

The center of mass of the cloud at time t* is given by (x_{sk}, y_{sk}), and the mean velocity in the k^{th} layer is given by $\bar{u}_k$ and $\bar{\theta}_k$. At time t*, the layer structure changes as indicated in Fig. 3-3.

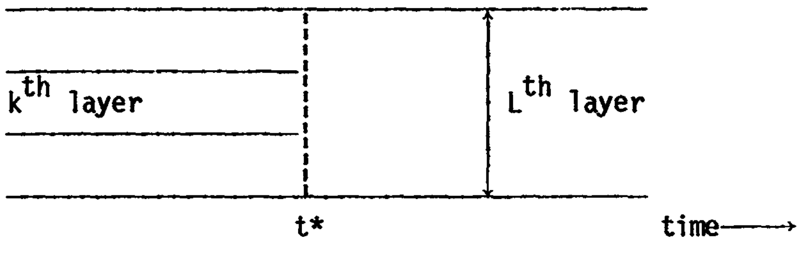

Figure 3-3 Layer structure before and after transition

The number of layers which combine to form the L^{th} layer is arbitrary, however, the upper and lower boundaries are required to coincide with existing boundaries prior to time t*. The L^{th} layer has a mean velocity denoted by $(\bar{u}_L, \bar{\theta}_L)$. Figure 3-4 shows the transition and relevant variables in the xy plane.

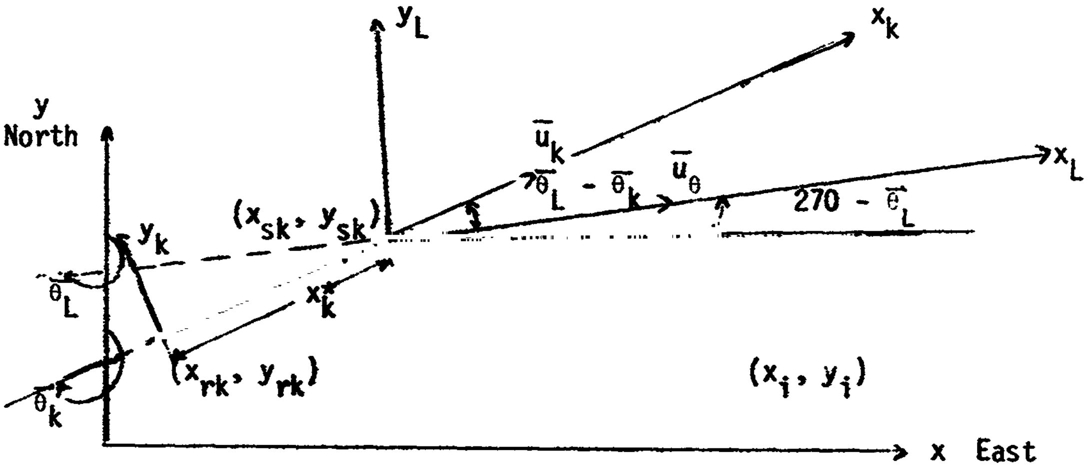

Figure 3-4 Horizontal section of transition

The transition problem includes relating the (x_k, y_k) and (x_L, y_L) coordinate systems, transforming the diffusion formulation from the k to L coordinate system and evaluation at specified receptor points. Since

$$x_k^* = \bar{u}_k t^* \tag{3-108}$$

it follows from Fig. 3-4 that

$$y_{sk} = y_{rk} - x_k^* \cos(\bar{\theta}_k) \tag{3-109}$$

and

$$x_{sk} = y_{rk} - x_r^* \sin(\bar{\theta}_k). \tag{3-110}$$

The point (x_{sk}, y_{sk}) may be thought of as being the grid system coordinates of the origin of the meteorological coordinate system after t*. The grid system and the L system are related by

$$x_L = -(x - x_{sk}) \sin(\bar{\theta}_L) - (y - y_{sk}) \cos(\bar{\theta}_L) \qquad (3\text{-}111)$$

and

$$y_L = (x - x_{sk}) \cos(\bar{\theta}_L) - (y - y_{sk}) (\bar{\theta}_L) \qquad (3\text{-}112)$$

$$z_L = z - z_{BL}$$

where z_{BL} is the vertical coordinate of the bottom boundary of the L^{th} layer. This set of equations is used to convert the coordinates of the receptor for use in the diffusion formulation. The cloud at time t* can be represented in the L system by variances along the x_L, y_L and z_L directions, which are respectively,

$$\sigma_{xL}^2 = \sigma_{xk}^2 \cos^2(\bar{\theta}_L - \bar{\theta}_k) + \sigma_{yk}^2 \sin^2(\bar{\theta}_L - \bar{\theta}_k) \qquad (3\text{-}113)$$

$$\sigma_{yL}^2 = \sigma_{xk}^2 \sin^2(\bar{\theta}_L - \bar{\theta}_k) + \sigma_{yk}^2 \cos^2(\bar{\theta}_L - \bar{\theta}_k) \qquad (3\text{-}114)$$

$$\sigma_{zL}^2 = \sigma_{zk}^2 \qquad (3\text{-}115)$$

where σ_{xk}^2, σ_{yk}^2 and σ_{zk}^2 are variances of the cloud with respect to the k system at t* and are calculated as outlined in Section 3.2.1.2.

To model the transition of the cloud at time t*, the cloud is imagined to be an instantaneous source in the L^{th} layer with σ_{xL}, σ_{yL}, and σ_{zL} representing the initial variances of the source. The program converts these variances to virtual distances using the equations given in Section 3.2.1.2. As this "new" cloud proceeds after transition, its variances are calculated from the inputs for the new layer as before with the substitution of t - t* for t in Equations (3-86) and (3-87).

For the purposes of evaluation of concentration and dosage, the new source is assumed to be a finite vertical line somewhere within the new layer. With some modifications, the models developed in Section 3.2.1.1

can be used. The integration indicated (3-13) now must take on the upper and lower limits of H_2 and H_1 respectively, where H_2 and H_1 are the heights of the upper and lower boundaries of the k^{th} layer relative to the base of the L^{th} layer. This changes the error functions in Equation (3-29) to

$$\operatorname{erf} \frac{H_2A^2-B}{\sqrt{2}\,A} - \operatorname{erf} \frac{H_1A^2-B}{\sqrt{2}\,A} . \tag{3-116}$$

For calculations after t*, $\overline{x}$ is given by

$$\overline{x} = x_L - \overline{u}_L(t - t^*) \tag{3-117}$$

and the height of the receptor is

$$z = z_i - z_{LB}. \tag{3-118}$$

The layer depth after t* is the depth of the L^{th} layer. The dosage modifications are analogous, and the resulting formulation is used when the along wind distance to the receptor is greater than x_k^*.

3.2.2 Deposition Model

The merging of the 0-5 km and 5-30 km diffusion models was relatively simple as there was no need to provide a linkage at the interface. The 5-30 km model thus runs independently of the 0-5 km model using different inputs and computational procedures. The case of general deposition is considerably more complex because the linkage between the two regions is now imperative. It is apparent, that to predict fallout from, for example, 10 km, one must also be able to predict fallout in the 0-5 km region. If two interfacing models are to be used in predicting fallout, then mass continuity must prevail at the interface. This implies that the model for the lower region must have provisions for dealing with the mass distributions generated by the model for the upper region. The present 0-5 km has no such provision, which is a consequence of the chronology of its development rather than its shortcomings. Three options were available: (1) to modify the existing 0-5 km model to accommodate the interface requirement, (2) to develop a new 0-30 km fallout which is independent of the existing 0-5 km model, or (3) to investigate the possibilities of extending the 0-5 km fallout model to 0-30 km. In consideration of the time and resources available, the third alternative was selected as being the most promising because it eliminates the interface problem completely.

A falling plume model is used for the prediction of fallout in the 0-5 km region. This permits the effects of diffusion to be included in the calculation of contamination density. The use of the same layer structure as that used in the diffusion calculations, permits the effects of wind shear to be included in the calculation. While vertical line sources are simulated by placing a number of area sources at equal distances along the line, there is no provision for inclined line sources. Thus, for the fallout calculations in the 0-30 km region, the missile trajectory must be simulated by a series of nonconnecting vertical line sources as illustrated in Fig. 3-5.

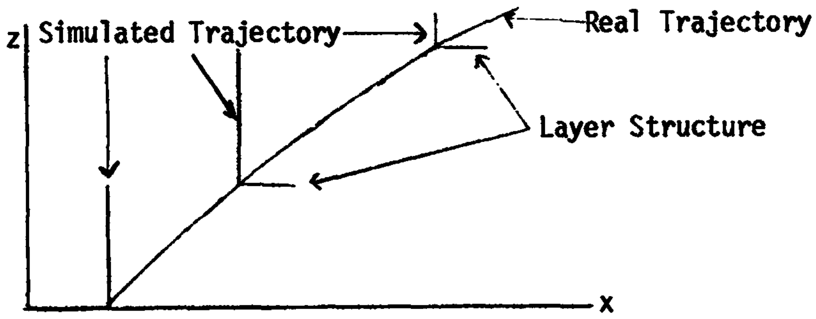

Figure 3-5 Trajectory simulation for the fallout calculation in the 0-30 km region

Quite clearly, this form of trajectory simulation is less desirable than the inclined line simulation used for the diffusion calculation in the 5-30 km region; however, the mechanics of allowing for the effects of wind shear more than make up for this drawback. The effects of density on terminal velocity have not been included, but in the case of an abort, this can be accounted for by adjusting the input values of terminal velocity. Technically speaking, the 0-5 km model can be applied in 5-30 km with some minor changes in the determination of inputs (see Section 3.3.7). For the technical documentation regarding this model, the reader is referred to Dumbauld et al. (1970).

3.3 Inputs for the 0-30 km Model

3.3.1 Introduction

The 0-30 km model requires that the user provide inputs describing the layer structure, missile trajectory, source strength, diffusion parameters and the distribution of both particle size and terminal velocity. This section is concerned with providing some criteria for the selection of meaningful inputs.

3.3.2 Criteria for Layer Selection

The single most important set of inputs is that which describes the layer structure. To be meaningful, they must provide an adequate description of the atmospheric state and at the same time reflect the major assumptions made in deriving the models which will operate within the structure. In terms of priority these assumptions are:

1. That there is no diffusion between layers; and
2. That the eastward and the northward components of the wind vary linearly with height within a layer.

The first relates to the form of the vertical term used in Equation (3-9), while the second relates to the calculation of shear. While no physical situation will satisfy either assumption exactly, approximate physical analogs to these assumptions do exist. The inversion characterized by its damping effect on vertical exchange provides a good criteria for the specification of layer structure. The second assumption is approximately satisfied in regions where wind speed and direction are monotonic and have single valued inverses. Fig. 3-6 illustrates these criteria.

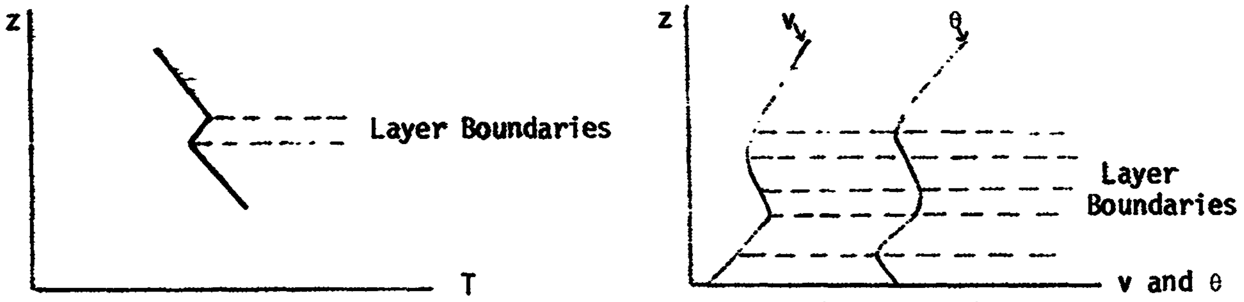

a. Thermal criteria

b. Wind speed and direction criteria

Figure 3-6 Criteria of determining layer structure

The need for the speed and direction criteria arises from the nature of the wind shear calculation. Figure 3-7 illustrates a hypothetical case where use of the thermal criteria above produces input values which lead to erroneous calculations of the effects of shear.

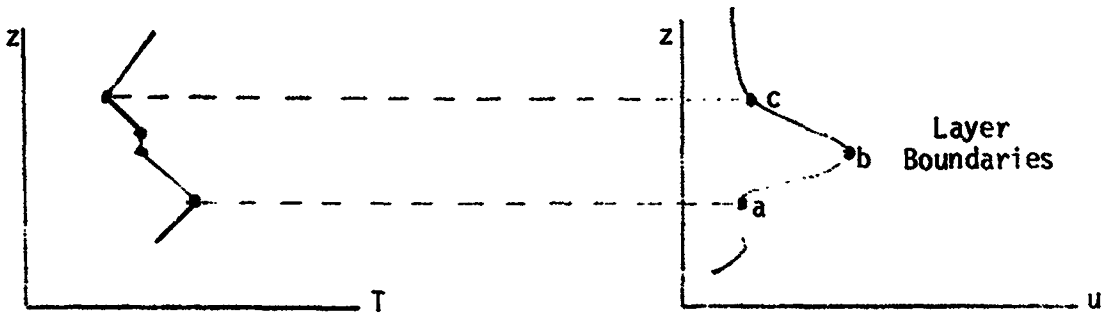

a. Thermal structure

b. Speed structure

Figure 3-7 Hypothetical case showing layer structure which leads to erroneous estimation of shear effects

Part (a) of Figure 3-7 shows the thermal structure and part (b) shows the profile of the along wind component of the wind. Use of the thermal criteria yields the layer boundaries indicated. The calculation of the shear effect requires that $\frac{du}{dz}$ be estimated over the layer. This is done by Equation (3-119):

$$\frac{\Delta u}{\Delta z} = \frac{u_c - u_a}{z_c - z_a} \tag{3-119}$$

where the subscripts indicate the point of evaluation. From the diagram, it is obvious that this estimate is rather poor. In fact, this example could represent the jet stream with the tropopause at point c, with $u_b - u_a$ being on the order of 40 m/sec. In cases like this, the layer should be subdivided at the jet axis (region of peak velocity). It is desirable that this division be justifiable in terms of the thermal structure (see region of greater stability in Fig. 3-7a). If this type of a justification can be made, the division does not necessarily have to coincide with the axis, although it must be near it. In the case that the division cannot be made on a thermal basis, it may be argued that the exclusion of the jet stream and its effects is not justifiable because it is a major structural form in the atmosphere.

The above discussion indicates that thermal criterion may be extended to isothermal regions as well as those which fall between adiabatic and isothermal, as indicated in Fig. 3-8. With these two additional criteria, the degree to which the first assumption is fulfilled becomes less as the layer considered to create the boundaries becomes less stable. Thus, in determining the layer structure, use inversions first, isothermal regions second, and then if the need arises, stable regions as indicated in

Fig. 3-8b. The mechanics of the model also require that layer boundaries coincide with the height of the tropopause and the 5 km level.

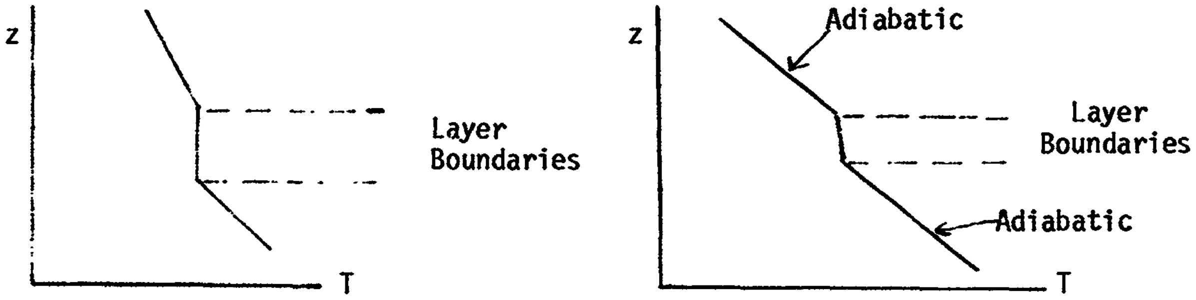

a. Isothermal

b. Stable but less than isothermal

Figure 3-8 Extension of layer division criterion

3.3.3 Use of Soundings

In terms of the criteria discussed above, the sounding data used to determine the layer structure are at the users option. In specifying the inputs for the trial case which is presented in Section 3.4, an AN/GMD-4 sounding was used. The resolution (values every 1000 feet) of these data was found to be sufficient to break up the 0-30 km region into an excess of twenty layers which is the limit of the present model. Data which are more accurate and of a higher resolution, while not necessary for the model's operation, will most certainly improve its prediction.

3.3.4 Missile Trajectory and Source Strength

The second most important set of inputs is that which describes the missile trajectory and source strength. In the trial case, three different methods (two graphical and one computational) of calculation of source strength within a layer were compared. These methods stem from the relationship given in Equation (3-47). It is necessary to have detailed data on the trajectory which gives altitude, velocity (along the trajectory), range and azimuth angle of the vehicle. The resolution necessary is dependent on the method of calculation used. For the graphical methods, the resolution requirements are given in Table 3-2.

Table 3-2 Resolution requirements for graphical procedure for finding source strength

Height Interval (m)	Resolution
0 - 100	not used
100 - 1000	100 meters
1000 - 14000	1000 meters
14000 - 30000	2000 meters

For the computational procedure, a resolution of 0.5 second for the entire trajectory is adequate, however, for small layers at great heights this causes some error because the vehicle's residence time in the layer is on the order of the resolution.

The computational procedure is a straightforward finite difference approximation to Equation (3-47):

$$\frac{dm}{d\ell} = Q_L \approx \frac{\dot{m}\Delta t}{\Delta \ell} \qquad (3\text{-}120)$$

where Δt is the residence time of the vehicle in the layer and $\Delta \ell$ is the length of the trajectory in the layer. The residence time can be approximated from the layer structure and the trajectory data. $\Delta \ell$ may be found as follows:

$$\Delta \ell = (\Delta x^2 + \Delta y^2 + \Delta z^2)^{1/2} \qquad (3\text{-}121)$$

where

$\Delta x = R_T \cos\theta_T - R_B \cos\theta_B$,

$\Delta y = R_T \sin\theta_T - R_B \sin\theta_B$,

Δz = layer thickness,

with

(R,θ) = polar coordinates of vehicle (range, azimuth) with the subscripts T and B indicating evaluation at the top and bottom of the layer respectively.

For hand calculation, this method is tedious, especially when several layers are being considered. The estimated value for Q_L is likely to be erroneous when Δt has the same magnitude as the resolution for the data. Interpolation will to some degree reduce this error and could easily be incorporated into a machine program for calculation of Q_L. This method, however, requires that $\dot{m}$ be constant over the layer, and it is desirable that this be at the option of the user.

The graphical methods, on the other hand, are faster and allow the user to specify $\dot{m}$ as a function of height. The fastest method is to plot z as the ordinate and the instantaneous value of $Q_L(\frac{\dot{m}}{v})$ as the abscissa on log-log paper. The mean value of Q_L for the layer is estimated by taking the value of Q which corresponds to the midpoint on the curve between the two heights which define the layer. For small layers with short residence times, this method will give very accurate results because as the size of the layer decreases, the mean value of Q_L approaches the instantaneous value at the center of the layer. This method is limited to layers which begin above the 1000 meter level, and the first method must be used to calculate Q_L in this region.

The third method is graphical and is intermediate in terms of the amount of calculation necessary. This method is in essence a stepwise numerical integration of the equation

$$Q_L = \frac{1}{z_T - z_B} \int_{z_B}^{z_T} \frac{\dot{m}}{v(z)}\, dz \tag{3-122}$$

which may be rewritten as

$$Q_L = \frac{1}{z_T - z_B} \int_{\ln z_B}^{\ln z_T} \frac{\dot{m}z}{v(z)}\, d\, \ln z \tag{3-123}$$

where z_T and z_B are the top and bottom of the layer respectively. This indicates that integration can be done on semilog paper by plotting z on the logarithmic axis and $\dot{m}z/v(z)$ on the linear axis. The integral is evaluated by a trapezoidal approximation so that

$$Q_L \approx \frac{.5}{z_T - z_B} \left[+ \frac{\dot{m}_B z_B}{v(z_B)} + \frac{\dot{m}_T z_T}{v(z_T)} \right] \ln\,(z_T/z_B) \tag{3-124}$$

as indicated in Fig. 3-9.

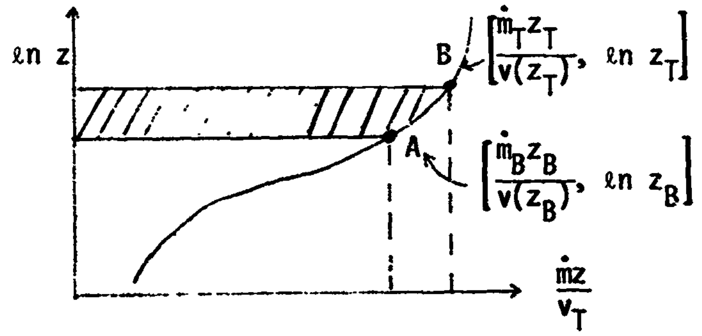

The quantity $Q_L(z_T-z_B)$ is given by the shaded area.

Figure 3-9 Single trapezoidal approximation for graphical estimation of Q_L

The accuracy of this method is dependent upon the shape of the $\ln\,(z_T)$ vs. $\dot{m}z/v(z)$ plot. In applying this method in estimating Q_L for the trial case, it became apparent that the method will have the largest error in the 1 to 1000 meter region; above this, the results were acceptable. However, if line AB in Fig. 3-9 has too much curvature to permit a linear approximation, the layer may, for the purpose of Q_L calculation, be broken up into several trapezoids as indicated in Fig. 3-10. In practical use, probably not more than two trapezoids will be needed, with one being satisfactory in most cases.

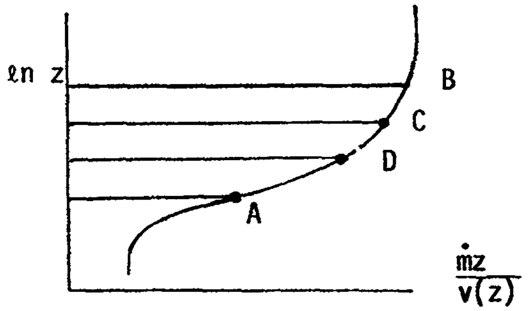

Figure 3-10 Three-step trapezoidal approximation for graphical estimation of Q_L

3.3.5 Diffusion Parameters

3.3.5.1 0-5 km Region

The 0-5 km model remains unchanged from the version developed by the GCA and is documented extensively in Dumbauld, et al. (1970) and Record, et al. (1970). Therefore, it is recommended that users consult these documents for instructions on the calculation of the various parameters required and for program use.

3.3.5.2 5-30 km Region

The essential diffusion parameters in this region are the initial standard deviations of the source and the lateral, alongwind, and vertical power law exponents. The reader is referred to Section 3.2.1.2 for discussion of the power law coefficients and their calculation from the average temperature gradient in the layer. The visual diameter of the exhaust plume just after emission can be estimated by assuming that it corresponds to a ten-fold reduction in all concentration at the plume axis (Slade 1968). Thus,

$$\sigma_i = \frac{R_i}{2.14} \quad (i = x,y) \tag{3-125}$$

where

σ_i = the standard deviation, and

R_i = the radius of the plume.

3.3.6 Specification of Depletion Parameters

As explained in Section 3.2.1.3, the required inputs for the washout and decay model are t_1, the time precipitation starts, and λ_W and λ_D, the coefficients of washout and decay respectively.

While it is relatively easy to predict, on a synoptic basis, the occurrence of precipitation over a specified period, it is not possible to predict the exact time at which the precipitation will begin. For this reason, it is suggested that t_1 be assigned several values for each run in which precipitation is predicted. The results obtained in this fashion will indicate the sensitivity of the diffusion and fallout patterns to t_1.

Considerably more has been done in connection with the estimation of the washout coefficient which is primarily a function of precipitation type and rate. It is suggested that this coefficient be estimated by the following formulas:

$$\lambda_W = \frac{\Lambda}{60} \cdot Dm \text{ for gases} \qquad (3\text{-}126)$$

$$\lambda_W = \frac{\Lambda}{60} \qquad \text{for precipitation} \qquad (3\text{-}127)$$

where Dm is the molecular diffusivity of the gas in units of cm^2/min, and Λ is given in Table 3-3 for various precipitation types.

The decay coefficient λ_D is dependent upon the material under consideration and to some degree the environment. If no coefficient is available, and it is thought that there is no sensible decay on a time scale of five hours, then the coefficient should be set to zero. If the coefficient is unknown and it is thought that there is appreciable decay, then it is suggested that a sensitivity analysis similar to that done for t_1 be performed.

Table 3-3 Parameters for precipitation removal models

		Λ Parameter Value		
			Particle Diameter (microns)	
Precipitation Type	Precipitation Rate (inches hr^{-1})	Gas	5	>20
Drizzle	0.01	2.0×10^{-1}	0.004	0.006
Light rain	0.10	1.35×10^{-2}	0.024	0.041
Moderate rain	0.30	2.59×10^{-2}	0.049	0.075
Heavy rain	0.70	3.88×10^{-2}	0.070	0.106

3.3.7 Inputs for the Deposition Model

3.3.7.1 Standard Deviations of the Wind Elevation and Azimuth Angles

The parameters of major importance are the standard deviations of the wind azimuth and elevation angles, σ_a and σ_e respectively. Measurements of these parameters in the surface layer are readily available in sufficient quantity so that they can be empirically related to wind speed and stability. However, in the free atmosphere, estimates of these and other diffusion-related parameters are rather difficult, if not impossible to obtain, and for this reason, analogous empirical studies are apparently nonexistent. Kao and others have contributed much to the study of the large scale dispersion in the free atmosphere. However, these studies are generally on a much larger time scale than the present study, therefore, they do not aid in the estimation of σ_a and σ_e.

The fact that diffusion does take place in the free atmosphere indicates that σ_e and σ_a are most certainly not zero except in very stable regions. Kellogg (1955) has observed that the mass growth of a diffusing cloud in the free atmosphere is correlated with stability. This result indicates that, as in the boundary layer, σ_a and σ_e are dependent upon stability. From estimates of the vertical and horizontal diffusivities, it can be argued that σ_e is probably more dependent upon stability than σ_a.

For the purposes of crude estimation, the criteria for the surface layer can be applied to the free atmosphere, however, this is very tenuous. Due to the extreme differences in wind speed in the surface layer and free atmosphere, it is probably better not to use this as an indicator.

3.3.7.2 Calculation of Terminal Velocity

The usual equation (Koch et al. 1968) for droplet diameter as a function of still air terminal velocity is given by

$$D = \sqrt{KV^{2.4} + CV} \tag{3-128}$$

where

D = droplet diameter, cm,

$K = \dfrac{(2.225 \times 10^{-2})\ \rho^{1.24}}{g(\rho_s - \rho)^{1.475}}$,

V = still air terminal velocity, cm/sec,

$C = \dfrac{18\eta}{g(\rho_s - \rho)}$, cm sec,

ρ_s = droplet density, gm/cm^3,

ρ = density of air, gm/cm^3,

g = 980 cm/sec^2, and

η = viscosity of air, dyne sec/cm^2.

While this equation must be solved iteratively, it provides a good means for estimating effects of density variation with height on terminal velocity. The viscosity of air as a function of temperature is given by the equation

$$\eta = .0001702\ (1 + .00329\ T + .000007\ T^2)\ \text{dyne sec/cm}^2. \qquad (3\text{-}129)$$

With sounding data giving air temperature (T°C) and density as a function of height, the numerical application of this set of equations yields terminal velocity as a function of height and particle size. If this function is given by v(z,D) and the burst height is given by H, then an average terminal velocity over the layer can be found from :

$$\bar{v}(D) = \frac{H}{\int_0^H \frac{dz}{v(z,D)}},\ D = \text{particle diameter} \qquad (3\text{-}130)$$

where the integral is the fall time from height H. If no abort occurs, H should be set equal to the vertical coordinate of the centroid of source strength distribution. This value of H is given by

$$H = \frac{\int_0^{30000} zQ_L(z)\ dz}{\int_0^{30000} Q_L(z)\ dz} = \frac{\int_0^{30000} zQ_L(z)\ dz}{\dot{m}t_R} \qquad (3\text{-}131)$$

where Q(z) is the source strength as a function of height, $\dot{m}$ is the mass flow rate from the missile, and t_R is the time required for the vehicle to reach an altitude of 30 km. While this method of correction is approximate, it is thought to be better than not correcting for the effects of density variation or setting arbitrary values for H.

For a more detailed analysis of the calculation of terminal velocity in the atmosphere, the reader is referred to Hage et al. (1966).

3.4 Trial Case - February 7, 1966

3.4.1 Synoptic Situation and Sounding Data

Figure 3-11 illustrates the surface map for February 7, 1966. The weather prior to this date had been dominated by the high pressure system off the southeastern coast of the United States. The eastward movement of this system caused surface wind shifts from east to southeast. On the synoptic scale, there was little chance of precipitation in the KSC area. There was, however, a distinct possibility that low level convergence connected with the eastward motion of the high pressure system and the subsequent low level advection of moist air from the south and east may have caused localized convective storms during the afternoon of the seventh.

The sounding used to determine the layer structure was taken from the 1815Z AN/GMD-4 rawinsonde run, ascent Number 5022. The sounding data was converted to standard meteorological units plotted as shown in Fig. 3-12. The temperature profile indicates that there are more than enough inversions and first order discontinuities to permit division of the 0-30 km region into an excess of twenty layers. Along the vertical line corresponding to 190° are horizontal line segments indicating the layer divisions based upon the criteria developed in Section 3.3.2. The segments at 5 and 18 kilometers represent the mandatory divisions, corresponding to the region modeled by the GCA and the tropopause respectively. This trial case is quite interesting due to the presence of the jet stream (peak) at 13.4 kilometers. The sensitivity of the model to wind shear could be tested by assuming various layer structures which in effect neglect some or all of the wind variation with height in this region. The layer structure and other input parameters derived from the sounding are listed in Table 3-4.

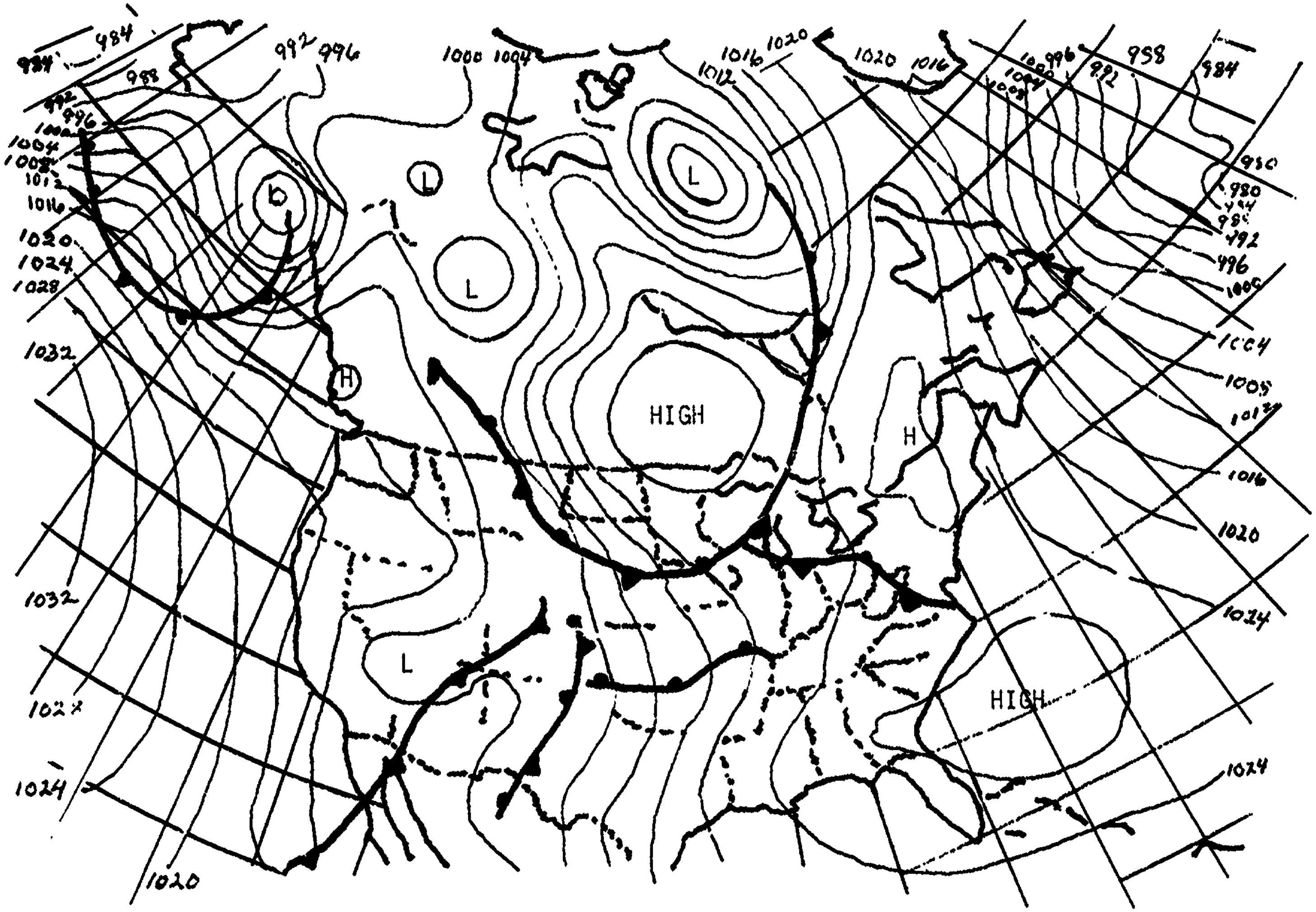

Figure 3-11 Synoptic surface map for February 7, 1966

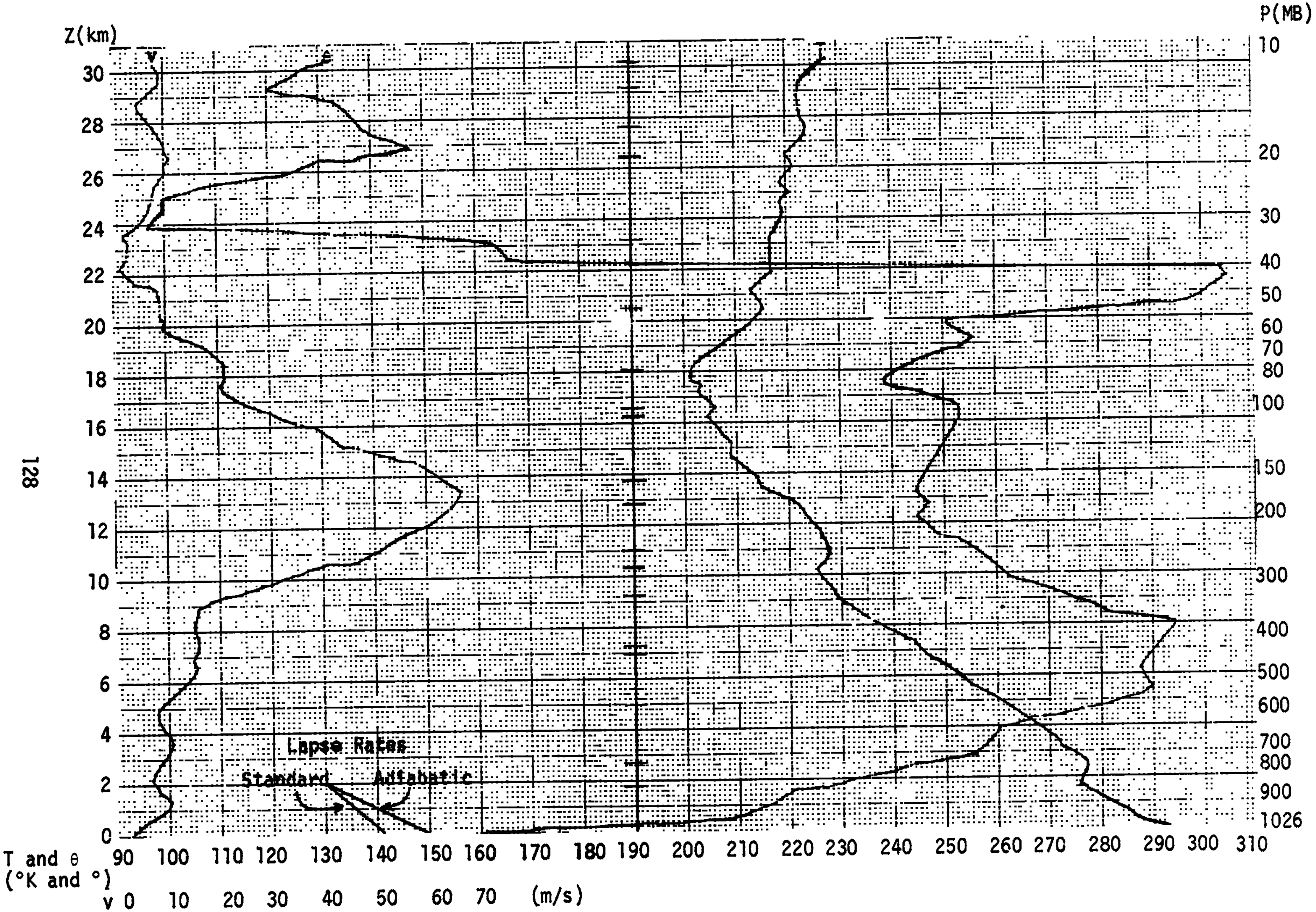

Figure 3-12 Sounding for February 7, 1966 1815Z

Table 3-4 Layer structure for test case

Layer	Top (meters)	Wind Direction (°)	Speed (meters/sec)	Thermal Gradient (°/km)	$\beta = .88 - 1.08 \frac{\Delta T}{\Delta z} \times 10^{-}$
0	0	160	3.0		
1	1828	226	7.7	-9.375	.3901
2	2743	258	8.2	2.185	.8798
3	5000	284	8.0	-6.735	.8873
4	7010	291	15.4	-7.958	.8886
5	7315	294	15.9	-3.608	.8839
6	9144	272	19.0	-7.983	.8886
7	10363	260	38.6	-3.034	.8833
8	10972	256	50.4	+3.280	.8264
9	12801	247	65.3	-3.772	.8841
10	13716	245	64.3	-7.5	.8879
11	16154	253	32.9	-3.731	.8840
12	16459	253	28.8	+3.280	.8764
13	17983	240	21.6	-2.362	.8825
14	20421	287	9.2	5.331	.8742
15	23165	156	3.0	.729	.8792
16	26517	138	10.8	1.342	.8786
17	27432	140	9.2	2.187	.8776
18	29261	120	8.2	-.273	.8803
19	30175	132	8.2	4.811	.8748

3.4.2 Trajectory Data

Both the diffusion and fallout models require inputs giving the point of intersection of the trajectory with each layer boundary and the source strength in each layer. The calculation of these inputs requires that a prior knowledge of the trajectory be known. For the trial case presented here, these data were obtained from a program listing found in "Apollo Saturn V Post Flight Trajectory AS508," D5-15560-8, Boeing Huntsville, June 10, 1970. Because these data satisfied the resolution requirements discussed in Section 3.3.4 and the program is available to NASA personnel, it is recommended that it be used in the case studies of actual launches. The data required for calculating the intersections and source strengths (the time after launch of intersection, range, azimuth angle and speed along the trajectory) are listed in Table 3-5. The x and y grid system coordinates of the points of intersection are calculated from the range (R) and azimuth angles by Equation (3-132) and (3-133) (see Table 3-6 for tabulated values for trial case):

$$x = R \sin\theta \tag{3-132}$$

$$y = R \cos\theta \; . \tag{3-133}$$

The calculation of source strength, as discussed in Sections 3.2.1.1 (briefly) and 3.3.4 (in full detail) requires a knowledge of the mass flow rate ($\dot{m}$) for the vehicle as a function of time or height. Since no data on this variation were immediately available, a steady state was assumed. The S-1C stage of the Saturn V contains five F-1 engines with a mass flow rate of 3×10^5 lb/min yielding an $\dot{m}$ for the vehicle of 25,000 lbs/sec. The graphical methods require the preparation of plots of $\ell n(\dot{m}/v(z))$ vs. $\ell n(z)$ and $\ell n(z)$ vs. $\dot{m}z/v(z)$ for the first and second graphical

Table 3-5 Trajectory data corresponding to layer intersections

Layer	Time after Launch (sec)	Range (m)	Azimuth (°)	Speed Along Trajectory (m/s)
1	36.5	98.7	79.1	114.9
2	43.5	263.8	75.3	150.3
3	56.5	949.6	73.6	230
4	64.5	1853.6	73.2	298
5	65.5	1989.8	73.2	307
6	71.5	2871.1	73.1	365
7	75.5	3779.4	72.99	405
8	77.5	4243.7	72.96	424
9	82.0	5438.1	72.91	467
10	84.5	6197.6	72.88	513
11	90.5	8330.6	72.83	589
12	91.0	8529.5	72.82	604
13	94.5	9797.6	72.80	653
14	99.0	12479.8	72.75	733
15	104.5	15363.7	72.70	829
16	110.5	19447.2	72.64	945
17	112.0	20582.4	72.6	946
18	115.0	22998.4	72.6	[illegible]
19	116.5	24281.4	72.6	[illegible]

Table 3-6 Coordinates of intersection of layer boundaries and trajectory in grid system

Layer	Grid System Coordinates of Intersection (m)		
	x	y	z
1	96.9	18.7	1828
2	255.2	66.9	2743
3	911.0	269.0	5000
4	1774	535.7	790
5	1905	575.1	7315
6	2747	834.6	9144
7	3614	1105	10363
8	4058	1240	10972
9	5102	1570	12801
10	5924	1822	1371
11	7958	2463	16154
12	8148	2522	16459
13	9359	2897	17983
14	11921	3690	20421
15	14668	4569	23165
16	18557	5815	26517
17	19641	6155	27432
18	21946	6877	29261
19	23170	7261	30176

methods respectively. In the trial, since a steady state assumption is made concerning $\dot{m}$, it is permissible in the second case to plot $\ell n(z)$ vs. $z/v(z)$ and pick up the multiplication later. Table 3-7 presents tabulated values for the graphs shown in Figs. 3-13 and 3-14. The data necessary for use of the computational method and the resulting estimate of Q_L, as well as the estimates obtained from the graphical methods, are shown in Table 3-8. These results indicate that:

1. The computational method works best in layers with large residence times;
2. Resolution problems in the computational method cause anomalous estimates (see, for example, layers 12, 14 and 17 of Table 3-8);
3. Except for surface layers the results of the graphical methods are reasonably close.

Because of its nature, the second graphical method is probably most accurate in layers above 1000 meters and is, therefore, recommended above the other methods.

3.5 Limitations of the Present Model and Recommendations

There are a number of areas in which more effort will undoubtedly bring about an enhancement of the present model's predictive capability. In order to facilitate a point by point discussion, these areas have been categorized in terms of the nature of each limitation and its potential solutions. Included in these discussions are recommendations as to how the potential solutions can be implemented.

Table 3-7 Tabulated values of $\dot{m}/v$ and z/v, as calculated from trajectory data taken from Boeing Huntsville Report referenced in text

Time after Launch (sec)	Height above Ground (m)	$\dot{m}/v(\bar{z})$ (lb/m)	$z/v(z)$ (sec^{-1})
1.5	.5	13812	.276
7.0	44.0	1745	3.07
12.0	147.0	9228	5.42
15.0	240.0	706	6.78
17.5	338.0	584	7.91
20.0	454.0	495	8.99
21.5	534.0	451	9.63
23.5	651.0	401	10.45
25.0	749.0	368.5	11.04
26.5	854.0	341.6	11.66
28.0	968.0	317	12.27
33.0	1460.0	246.6	14.40
38.0	1957.0	204.9	16.04
42.0	2477.0	175.8	17.42
45.5	2955.0	154.8	18.34
51.0	3938.0	128.0	20.16
56.0	4940.0	108.7	21.48
60.5	5968.0	94.5	22.55
64.5	6986.0	83.8	23.41
68.0	7960.0	75.7	24.12
71.5	9014.0	68.7	24.78
74.5	9981.0	63.3	25.29

Continued

Table 3-7 Tabulated values of $\dot{m}/v$ and z/v, as calculated from trajectory data taken from Boeing Huntsville Report referenced in text - Concluded

Time after Launch (sec)	Height above Ground (m)	$\dot{m}/v(\bar{z})$ (lb/m)	$z/v(z)$ (sec^{-1})
77.5	11009.0	58.5	25.74
80.0	11912.0	54.7	26.08
82.5	11851.0	51.3	26.37
85.5	14055.0	47.5	26.69
90.0	15973.0	42.42	27.11
94.5	18044.0	38.02	27.44
98.5	20009.0	34.6	27.66
102.5	22090.0	31.5	27.82
106.0	24005.0	29.1	27.92
109.5	26007.0	26.9	27.98
113.0	28095.0	24.9	28.01
116.0	29953.0	23.4	28.00

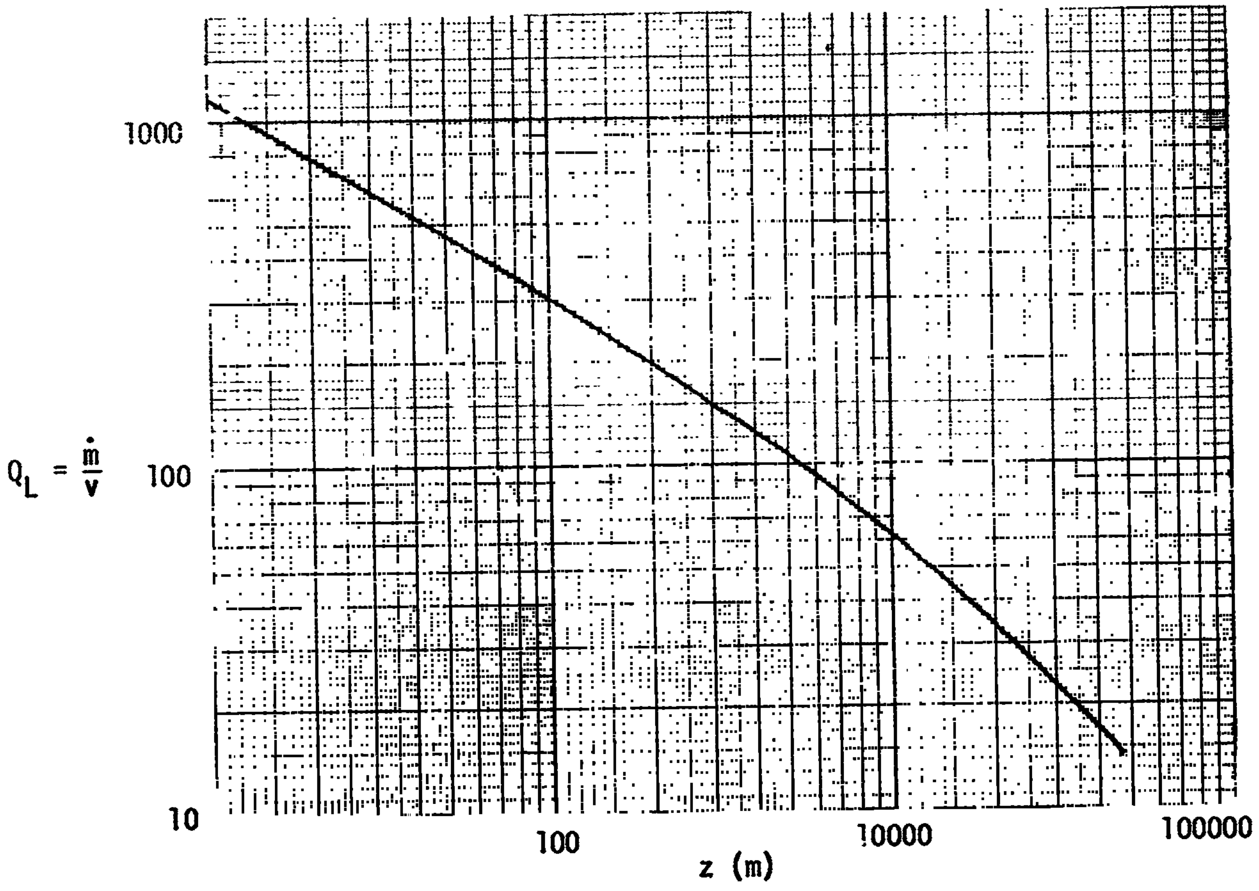

Figure 3-13 Plot for first graphical procedure for estimation of Q_L

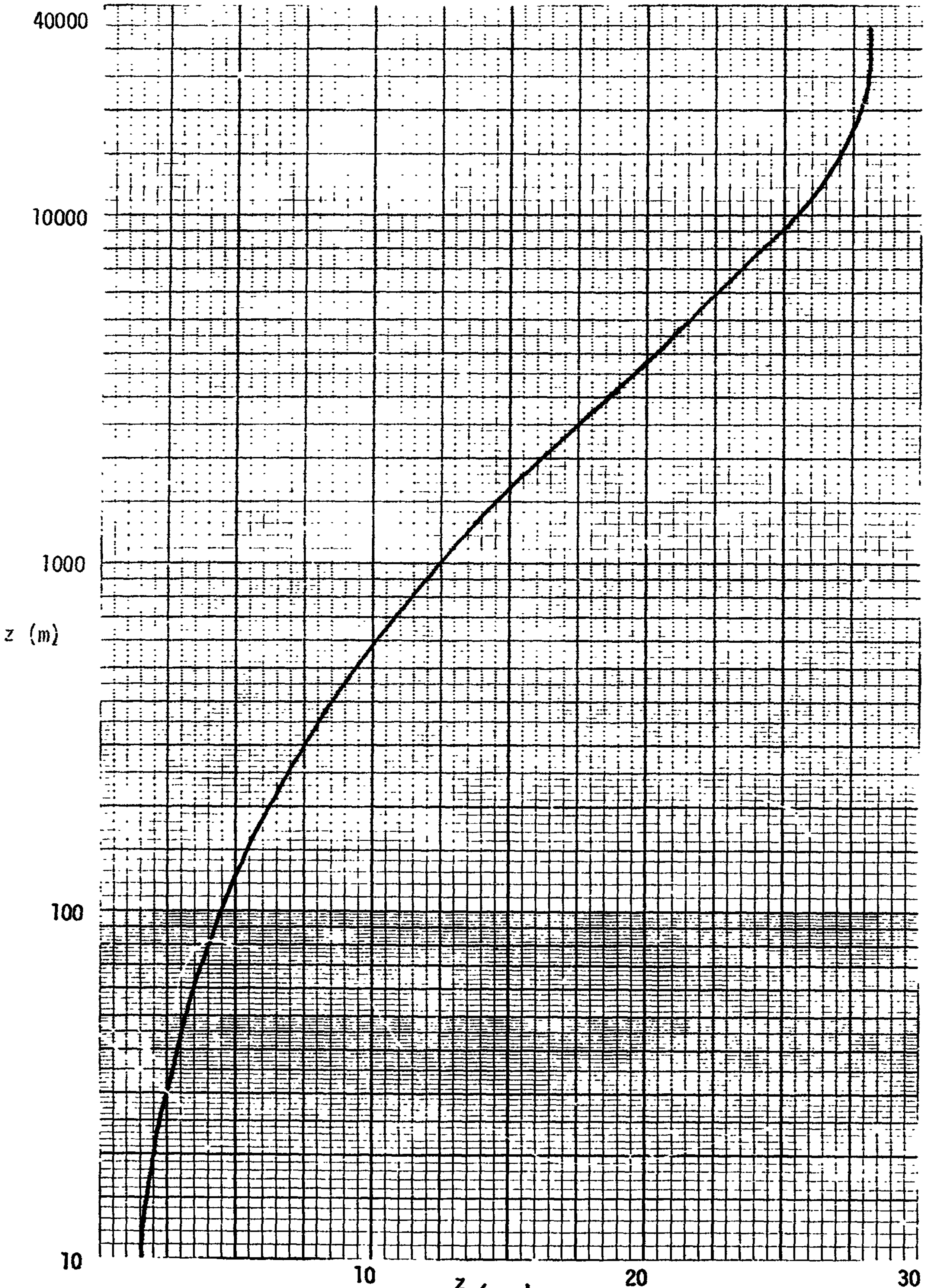

Figure 3-14 Plot for second graphical estimation of Q_L

Table 3-8 Calculation of source strength

Layer	Length of Trajectory in Layer $\Delta\ell$ (m)	Residence Time (R_T) (sec)	Computational Method $Q_L = \frac{R_T \cdot \dot{m}}{\Delta\ell}$ (lb/m)	Graphical Methods	
				First Q_L	Second Q_L
1	1830	36.5	498.6	465	896.4
2	929.8	7	188.2	185	186.8
3	2359	12.5	132.5	135	131.3
4	2203	8.5	96.5	95	94.3
5	334	1.0	74.9	82	82.2
6	2030	6.0	73.9	74	74.3
7	1520	4.0	65.8	64	64.8
8	765	2.0	65.4	60	60.0
9	2132	4.5	52.8	55	54.9
10	1256	2.5	49.8	51	50.0
11	3239	6.0	46.3	47	44.3
12	364	.5	34.3	45	41.6
13	1982	3.5	44.1	41.5	39.7
14	3624	4.5	31.0	37	36.0
15	3987	5.5	34.5	32.5	32.0
16	5283	6.0	28.4	28.5	28.2
17	1459	2.5	42.8	26	26.0
18	3030	3.0	24.8	24.5	24.7
19	1576	1.5	23.8	23.5	23.6

3.5.1 Shear

There are a number of refinements possible in the present shear model. The most evident is the requirement for linearity in u and v throughout a layer. It is probable that this drawback can be overcome by running a regression analysis on u and v within a layer resulting in two poloynomials, which can then be substituted into the system of differential equations for the cloud moments. The solution of the resulting equation can probably be obtained by either Laplace or finite cosine transform techniques (as previously applied). As in the present model, this procedure would lead to expressions for the variances of the cloud. The application of these variances would, however, present another problem since with non-linear velocity profiles there is no guarantee that the initial cloud distribution will subsequently remain Gaussian. This, of course, implies the need for the calculation of higher moments including covariances. The problem of finding a closed form for the resulting distribution is probably best handled by statistical methods including a consideration of the distribution's moment-generating function.

This discussion readily leads to another potential improvement of the present shear model. In deriving the inclined line model, the covariances or correlation coefficients in the xz and xy direction were assumed to be zero, which will suffice as a first step in the modeling process. A more exact representation of shear will probably result from the inclusion of a non-zero covariance. This is directly indicated by the fact that in a shear field the cloud axes rotate.

A third element of the shear analysis regards the specification of values for k_z. While average values for the troposphere and stratosphere can easily be found in the literature, little can be said about the variation of k_z with height. However, for the results of the shear analysis to provide an improvement over those of the k theory, k_z should be specified as an analytic function of height within each layer.

3.5.2 Diffusion Parameters in the Free Atmosphere

Hand in hand with the problem of specifying k_z as a function of height, is the problem of determining a set of diffusion parameters for the free atmosphere in terms of readily measurable quantities. As indicated in Section 3.3.7, the application of empirical laws derived in the boundary layer to the free atmosphere is questionable. In fact, the present criteria for determining the power-law coefficient appears to be to some degree insensitive to changes in stability. A greater variation in the coefficient with temperature gradient is indicated on the grounds of both sensitivity and the thermal structure near the ground (intense gradients) where the present criteria were developed. A theoretical basis for modification of the present criteria may be possible by using statistical models of diffusion. An extensive data base will be necessary to develop similar criteria for the free atmosphere.

3.5.3 The Nature of the Diffusion Process at the Layer Interfaces

In deriving the present model, the interface between layers has been assumed to be a reflecting surface. A logical extension to this is the consideration of partial reflection and partial diffusion through the interface as a function of stability. The incorporation of the work done by Hilst (1967) and Priestley (1953) would provide a starting point for such consideration.

3.5.4 Layer Structure and Meteorological Inputs for the Fallout Model

Modifications to improve the fallout model are based upon the use of numerical integration to determine the trajectory of the center of mass of area sources used to simulate the source. Specifically this would include:

1. The addition of air density as an input;
2. The inclusion of the calculation of terminal velocity in the program;
3. The provision for a layer structure which will allow each point on the sounding to be used as an input; and
4. The addition of the synoptic scale vertical velocity of the air in the region of interest to allow for air flow along isentropic surfaces.

More sophisticated improvements can be made by studying the effect of turbulence on the dispersion of the cloud as it falls. These modifications would primarily effect the calculation of the horizontal cloud variances. In developing an operation model, these effects should be related to a parameter which is easily measured, such as the thermal gradient studies done by Csanady (1963) and Katz (1965). These studies, concerning the effects of turbulence on falling particles, are a logical starting point for this type of modification.

3.6 References

Aris, R. 1956. "On the Dispersion of a Solute in a Fluid Flowing Through a Tube." Proceedings of the Royal Society. A235:67-77.

Csandy, G. T. 1969. "Diffusion in an Ekman Layer.' Journal of the Atmospheric Sciences. Vol 26. May 1969.

Dumbauld, R. K., J. R. Bjorkland, H. E. Cramer and F. A. Record. 1970. "Handbook for Estimating Toxic Fuel Hazards." GCA Corporation. Bedford, Mass. NASA Contractor Report. NASA CR-61326.

Gee, J. H. 1967. "A Note of the Effect of Directional Wind Shear on Medium-Scale Atmospheric Diffusion." Quarterly Journal of the Royal Meteorological Society. No. 88:382-393.

Hage, K. D., et al. 1966. "Particle Fallout and Dispersion in the Atmosphere." Final Report. Sandia Corporation. SC-CR-66-2031.

Hilst, G. R. 1967. "Environmental Hazard Study." The Travelers Research Center, Inc. 250 Constitution Plaza. Hartford, Conn. NASA Contractor Report. NASA CR-61163.

Hogstrom, V. 1964. "An Experimental Study on Atmospheric Diffusion." Tellus. 16:205-251.

Katz, J. E. 1966. "Atmospheric Diffusion of Settling Particles with Sluggish Response." Journal of Applied Meteorology. No. 23:159-166.

Kellogg, W. W. 1956. "Diffusion of Smoke in the Stratosphere." Journal of Applied Meteorology. No. 13:241.

Koch, R. C., et al. 1968. Chemical and Biological Weapons and Defense Technical Data Source Book. Supporting Study Number 3: VX Models and Parameters. Report Number 7301-7. GEOMET, Incorporated. Rockville, Maryland.

Priestley, C. H. B. 1953. "Buoyant Motion in a Turbulent Environment." Austrailian Journal of Physics. Vol. 6. pp.279-290.

Record, F. A.,et al. 1970. "Analysis of Lower Atmospheric Data for Diffusion Studies." GCA Corporation. Bedford, Mass. Report No. TR-69-15N.

Saffman, P. G. 1962. "The Effect of Wind Shear on Horizontal Spread from an Instantaneous Ground Source." Quarterly Journal of the Royal Meteorological Society. No. 88:382-393.

Slade, D. H. 1968. "Meteorology and Atomic Energy." U. S. Atomic Energy Commission/Division of Technical Information.

Smith, F. B. 1965. "The Role of Wind Shear in Horizontal Diffusion of Ambient Particles." Quarterly Journal of the Royal Meteorological Society. No. 91:318-329.

Taylor, G. I. 1954. "The Dispersion of Matter in Turbulent Flow Through a Pipe." Proceedings of the Royal Society. A233:446-467.

Taylor, G. I. 1953. Proceedings of the Royal Society. A219:186.

Tyldesley, I. G. and C. E. Wallington. 1965. "The Effect of Wind Shear and Vertical Diffusion of Horizontal Dispersion." Quarterly Journal of the Royal Meteorological Society. No. 91:158-174.

APPENDIX A: CORRECTION OF THE MSFC FILM DATA

Allowance must be made for wind transport of the cloud toward or away from the camera. The following procedure divided the total test firing period into two regions: a region where jet effects are dominant, i.e., $V_T >> V_A$ where V_T is the velocity of the jet and V_A is atmospheric wind velocity and a region where atmospheric effects are dominant, i.e., $V_T \approx 0$.

Region 1: $V_T >> V_A$

Figure A-1 illustrates the geometry of the conditions that exist when jet effects are dominant. The equations for lin [illegible] D and CED are given in equations (A-1) and (A-2) respectively.

$$\frac{X}{\cos \theta} = \frac{Y}{\sin \theta} = \frac{Z}{\tan \alpha} \qquad \text{(A-1)}$$

$$\frac{X}{X_m} = \frac{Y + L}{L} = \frac{Z}{Z_m} \qquad \text{(A-2)}$$

where

X = horizontal distance (meters)

Y = distance cloud moves toward or away from camera plane (meters)

Z = vertical distance (meters)

α = deflector angle measured from horizontal (degrees)

θ = $90-\beta$ = azimuth angle measured from true north (degrees)

X_m, Z_m = the converted coordinate data measured by analyzer.

L = distance from camera to test stand (meters)

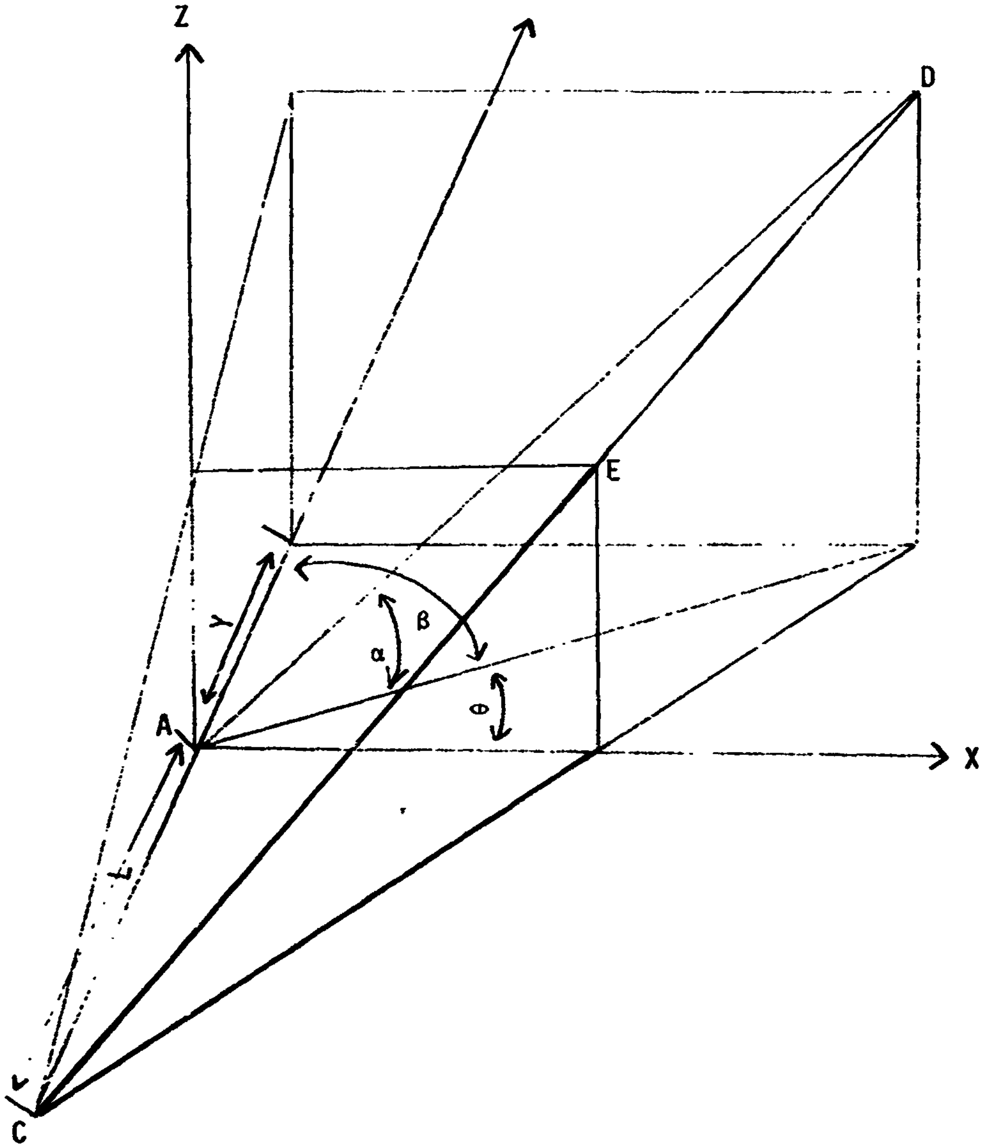

where

α = deflector angle measured from the horizontal

θ = 270-(azimuth angle measured from the north)

A = cloud origination point

C = camera position

D = point of interest on cloud

E = point of interest as measured by analyzer

Y = distance cloud moves toward or away from camera plane.

Figure A-1 Geometry of conditions that exist when jet effects are dominant

Solving for X and Z in terms of Y in (A-1) yields

$$X = Y \cot \theta \qquad \text{(A-3)}$$

and

$$Z = Y \tan \alpha / \sin \theta . \qquad \text{(A-4)}$$

Solving for X and Z in terms of Y in (A-2) yields

$$X = \frac{X_m Y}{L} + X_m \qquad \text{(A-5)}$$

and

$$Z = \frac{Z_m Y}{L} + Z_m \qquad \text{(A-6)}$$

If X_m and Z_m were known precisely, then (A-3), (A-4), (A-5) and (A-6) could be solved simultaneously for Y which could be used to correct the data. However, since they are not known exactly (differing by a ΔX_m and ΔZ_m, respectively), lines AD and CED may not intersect. In the XZ plane the distance between these lines is given by equation (A-7).

$$B = \left(\left(Y \cot \theta - \frac{X_m Y}{L} - X_m \right)^2 + \left(Y \tan \alpha / \sin \theta - \frac{Z_m Y}{L} - Z_m \right)^2 \right)^{1/2} \qquad \text{(A-7)}$$

In the case that lines AD and CED do not intersect, the value of Y for which B is minimized is used to calculate the correction factor. This value is found by setting the derivative of B (with respect to Y) equal to zero and solving for Y. This procedure yields:

$$Y = \frac{kX_m + cZ_m}{k^2 + c^2} \qquad \text{(A-8)}$$

where

$$k = \cot \theta - X_m / L \qquad \text{(A-9)}$$

and

$$c = \tan \alpha / \sin \theta - Z_m / L . \qquad \text{(A-10)}$$

Substituting this value of Y into (A-2), one obtains the "real" coordinates X_R and Z_R, where X_R is the corrected horizontal distance as measured from the firing point in meters and Z_R is the corrected vertical distance as measured from the firing point in meters. The comparison of the results from (A-1) and (A-2) yields an estimate of the error in Y.

Representative values of X_m and Z_m, taken from Case TWF 037 for a time after firing equal to three seconds, were used to check the above procedure. Reader 1 had values of 133.12 m and 91.20 m for X_m and Z_m respectively, while reader 2 had values of 117.25 m and 81.68 m. These were averaged to yield $\overline{X_m}$ = 125.18 m and $\overline{Z_m}$ = 86.43 m. Using equation (A-8) for $\theta = 48°$ and $\alpha = 30°$ one obtains Y = 112.13 m. Substituting this value into (A-3) and (A-4) yields X_1 = 124.53 m and Z_1 = 96.75 m; substitution into (A-5) and (A-6) yields X_2 = 128.59 m and Z_2 = 88.78 m. The difference between X_1 and X_2 is -4.06 m and $Z_1 - Z_2$ is 7.97 m which is well within the variability of X_m and Z_m.

Region 2: $V_T \approx 0$

For the correction of the film data when $V_T \approx 0$ an estimate of the height where jet effects become negligible is needed. At this height both Z_R and Y will be known. It is now assumed that at any height above Z_R atmospheric winds will dominate. The data given for each case give wind speed and direction for selected heights. It will be assumed that there is a linear variation of wind speed and direction between measured values. It will also be assumed that the vector wind in a layer between a measured height Z_{m1} and a higher measured height Z_{m2} will be approximated by the vector wind at Z_{m1}. Using these assumptions, the value of Y at any measured height Z_{m_1} will be given by (A-11) and (A-12).

$$Y(Z_{m_i}) = Y_{t_{i-1}} + V_a(Z_{m_i})\,(t_i - t_{i-1}) \qquad i > 0 \qquad \text{(A-11)}$$

$$t_i - t_{i-1} = 0 \qquad i = 0 \qquad \text{(A-12)}$$

where

$Y(Z_{m_i})$ = value of Y at height measured Z_{m_i}

t_i = time at which Y is being measured, and

V_a = atmospheric wind velocity at height Z_{m_i}.

For the case i = 0, the initial value of Y at Z_{m_o} is used, where Z_{m_o} is the height where jet effects become negligible. Generally, the time at which the height of a point on the cloud is equal to Z_{m_o}, is bracketed by two consecutive times, t_p and t_R, at which measurements are made. In the case i = 1, the value of t_{i-1} is defined as t_p where $t_p < t_R$.

APPENDIX B: VERIFICATION OF CORRECTION TECHNIQUE

B.1 Introduction

In lieu of having real data upon which the correction technique can be verified, a procedure, using synthesized (and hence known) trajectories was developed to test the mathematical validity of this technique. The testing procedure may be outlined as follows:

1. Trajectories simulating the movement of points on the cloud were generated mathematically. These trajectories then correspond to the "real values" discussed in Appendix A.
2. From the trajectories, values representing the film measurements are generated.
3. The correction technique is applied to the "measured values" generated in step (2) to obtain estimates of the trajectory generated in step (1).
4. The last step involves a comparison of the "measured values" with the "real values" as a function of the parameters used in generating the trajectory.

B.2 Accuracy Limits of the Phase 1 Correction Procedure

A basic question of the validity of the first phase correction is that of the uniqueness of a particular set of measured values taken from the film analysis. A set of measured values is termed unique if it corresponds to one and only one real trajectory in three-dimensional space. The physical character of the correction problem indicates that uniqueness is the exception rather than the rule. Consider two independent trajectories given by radial lines extending from the origin (cloud source):

$$\left.\begin{aligned} X_R &= \cos\theta \cot\alpha\, Z_R \\ Y_R &= \sin\theta \cot\alpha\, Z_R \\ Z_R &= Z(t) \end{aligned}\right\}\text{Trajectory 1}\qquad \begin{aligned}&\text{(B-1)}\\&\text{(B-2)}\\&\text{(B-3)}\end{aligned}$$

and

$$\left.\begin{aligned} X_{R1} &= \cos\theta_1 \cot\alpha_1\, Z_{R1} \\ Y_{R1} &= \sin\theta_1 \cot\alpha_1\, Z_{R1} \\ Z_{R1} &= Z_1(t) \end{aligned}\right\}\text{Trajectory 2}\qquad \begin{aligned}&\text{(B-4)}\\&\text{(B-5)}\\&\text{(B-6)}\end{aligned}$$

where

θ = azimuth angle,

α = elevation angle, and

X_R, Y_R, Z_R = coordinates of a point on the "real" trajectory.

The corresponding sets of "measured values" are given by

$$\left.\begin{aligned} X_m &= \frac{L\, X_R}{L + Y_R} \\ Z_m &= \frac{L\, Z_R}{L + Y_R} \end{aligned}\right\}\text{Trajectory 1}\qquad \begin{aligned}&\text{(B-7)}\\&\text{(B-8)}\end{aligned}$$

and

$$\left.\begin{aligned} X_{m1} &= \frac{L\, X_{R1}}{L + Y_{R1}} \\ Z_{m1} &= \frac{L\, Z_{R1}}{L + Y_{R1}} \end{aligned}\right\}\text{Trajectory 2}\ .\qquad \begin{aligned}&\text{(B-9)}\\&\text{(B-10)}\end{aligned}$$

If the sets of measured values are unique and X_m and Z_m are set equal to X_{m1} and Z_{m1} respectively, then it follows that θ, α and $Z(t)$ must equal θ_1, α_1 and $Z_1(t)$ respectively. Since it is assumed that

$$X_{m1} = X_m \tag{B-11}$$

$$Z_{m1} = Z_m \tag{B-12}$$

then it follows that

$$\frac{X_{m1}}{Z_{m1}} = \frac{X_m}{Z_m} \qquad Z_{m1} \neq o, \; Z_m \neq o. \tag{B-13}$$

From (B-13) and the equations defining the measured values for both trajectories we have

$$\frac{X_R}{Z_R} = \frac{X_{R1}}{Z_{R1}}. \tag{B-14}$$

From (B-14) and the equations defining the trajectories it follows that

$$\cos \theta \cot \alpha = \cos \theta_1 \cot \alpha_1. \tag{B-15}$$

The definition of uniqueness requires that $\theta = \theta_1$ and $\alpha = \alpha_1$ be the only solution of (B-15). Solving (B-15) for α_1 yields

$$\alpha_1 = \cot^{-1}(\cos \theta \cot \alpha \sec \theta_1). \tag{B-16}$$

Since the domain of the inverse cotangent is the set of real numbers there are no restrictions on θ_1(for fixed θ and α) for (B-16) to hold. This indicates that (B-16) has an infinite number of solutions which indicates that unique sets of measured values do not exist. Therefore the construction of an exact correction technique is not possible since uniqueness is required for its existence.

This result indicates that an operational correction technique must be supplemented with additional approximate information about the real trajectory. This additional information for the first phase correction technique takes the form of the assumption that all observed trajectories will be close to the jet axis. Considering the jet-like nature of the plume during this phase, this assumption is a rather good approximation. It follows that the closer the observed trajectory is to the jet axis, the greater the accuracy of the correction technique. The correction technique will thus have the potential of being exact only when the observed trajectory corresponds to the jet axis. It also follows that the accuracy of a correction technique based upon this type of supplemental information is dependent upon the spreading of the plume (and hence the trajectories). While the calculation of the plume's spreading is tenuous, it is possible to use film observations to estimate the maximum angular deviation from the jet axis. Since the error in the correction technique increases with spreading, the use of this estimation will produce maximum error. Visual estimation from the MFSC films, indicates that the spreading is on the order of 10 to 15 degrees about the jet axis. The verification was done using this estimate.

B.3 Results of Phase 1 Verification

The basic assumption for the phase 1 correction is that the plume is oriented along the jet axis, determined by the azimuth angle and the firing tower's deflection elevation angle. If the trajectory of a point follows the jet axis then it follows from the method, that the estimates of the trajectory have no error. Since the correction is purely geometric, any reasonable mathematical trajectory will suffice for the accuracy test. The most meaningful parameters for the trajectory, in terms of the physical situation, are the azimuth and elevation angles of the points which form it. It is, therefore, possible to speak in terms of maximum angular deviations from the jet axis. Physically, this corresponds to one-half of the angular width of the plume. The most convenient trajectory for analysis is a straight line segment passing through the origin with azimuth and elevation angles given by ϕ and α respectively. The verification may now be run for several trajectories with suitable estimates of ϕ and α. Preliminary results which have been obtained with the deviation set a ± 10°, indicate that the corrected value is always a better estimate than the raw uncorrected data. The error in the corrected data increases with height except for trajectories which coincide with the jet axis.

Since all but one transition height is less or equal to 220 uncorrected meters (average = 189.9), it seems logical to set this as the upper limit for the phase 1 trajectory. Therefore, the use of this phase 1 limit will slightly overestimate the error for a majority of cases.

Table B-1 shows the results of the first phase verification with a plume width of 20°, the jet axis defined by an elevation of 30° and azimuth of 40° for a transition height of 220 meters. For the purpose of physical orientation, the true azimuth or compass reading may be obtained by subtracting the azimuth reading given here from 270°. The values in Table B-1 were obtained from each of the listed trajectories by selecting real points with a measured vertical height closest to 220 meters. The information in Table B-1 was subjected to an error analysis and the results summarized in Table B-2. The first two columns of Table B-2 represent the real correction factor and estimated correction factor, while the last three columns present the percentage error in the uncorrected data, error in the X and Z values of the corrected values and error in the Y value of the corrected data respectively. From Table B-2 we conclude that:

Table B-1 Results for phase 1 correction for 20° plume width and 220 meter transition level

Trajectory data		Real data set			Measured data set		Corrected data set		
Azimuth	Elevation	XR	YR	ZR	XM	ZM	XE	YE	ZE
30°	20°	567.4	329.4	240	525.4	222.9	577.1	405.7	244.8
40°	20°	501.3	423.4	240	454.6	217.6	494.2	359.5	236.5
50°	20°	454.7	546.3	260	401.5	229.6	433.9	332.8	248.2
30°	30°	357.5	207.5	240	340.4	228.5	364.7	294.8	244.7
40°*	30°*	315.8	266.7	240	296.6	225.4	315.8	266.7	240.1
50°	30°	264.5	317.7	240	245.5	222.8	259.5	234.6	235.5
30°	40°	245.8	142.7	240	237.5	232.0	251.0	233.9	245.2
40°	40°	217.1	183.4	240	207.8	229.8	218.7	215.1	241.7
50°	40°	181.8	218.4	240	172.6	227.9	180.7	193.1	238.6

LEGEND: XR, YR, ZR = real values
XM, ZM = measured values
XE, YE, ZE = estimated values of XR, YR, ZR

* This trajectory is along jet axis.

Table B-2 Error analysis of results presented in Table B-1

Trajectory data		Correction factors		Error(a) $\frac{\text{real value - parameter}}{\text{Real value}}$		
Azimuth	Elevation	Real	Estimated	Uncorrected data (XM and ZM)	Corrected data (XE and ZE only)	Corrected data (YE only)
30°	20°	1.079	1.098	-7.4	1.7	23.1
40°	20°	1.103	1.087	-9.3	-1.4	-15.1
50°	20°	1.133	1.081	-11.7	-4.5	-38.1
30°	30°	1.050	1.071	-4.7	2.0	42.1
40°(b)	30°(b)	1.065	1.065	-6.1	0.0	0.0
50°	30°	1.077	1.057	-7.2	-1.9	-26.6
30°	40°	1.035	1.057	-3.4	+2.1	+63.9
40°	40°	1.045	1.052	-4.3	0.7	17.3
50°	40°	1.053	1.047	-5.1	-.6	-11.6

(a) Note that there may be some slight derivation between the values for X values and Z values due to round-off error of data presented in Table B-1.

(b) Jet axis.

1. While subject to error, the phase 1 corrected data is a better estimator of the real values than the uncorrected data.

2. The absolute error in phase 1 correction technique is most probably not more than two percent for a plume width of 20° (this is based on the transition height as explained above, and the fact that particles with an azimuth of 50° are most probably on the opposite side of the plume and thus are not likely to be seen, and hence measured).

3. YE is seen to have a relatively large error and, while not relevant to our study, should be dealt with cautiously in any other studies.

4. The method works best in areas where the real correction factor is small. Implicit in this conclusion is the basic criterion for the success of this method; that the deviation of the plume from the camera plane must be small when compared to the observation distance.

B.4 Phase 2 Verification

Because phase 1 errors are carried over into the phase 2 correction, the realistic verification of the phase 2 technique must include an analysis of the effects of phase 1 errors. This was accomplished by treating the phase 1 and phase 2 verification as a single mathematical investigation. In the testing, time was used as the independent variable. This required rewriting the phase 1 program which used height as the independent variable. To do this, the additional input of vertical velocity of the point along a trajectory during phase 1 was required. Phase 2 errors are also influenced by errors in measurement of transition height. The general correction technique calls for the application of the phase 1 procedure below the transition height and the application of the phase 2 procedure above the transition height. An overestimation of transition height will result in application of the phase 1 technique in a region where the phase 2 procedure should have been applied. The time and coordinates of the point as it reaches the transition height are used as an input to the phase 2 procedure. In essence, the phase 2 technique uses a numerical integration of the horizontal wind as a function of height to the trajectory of a point. The transition and phase 1 errors may be thought to be errors in the initial conditions of the integration. The third error considered in the phase 2 verification is the error inherent in the numerical integration itself.

The following inputs are needed to simulate and verify the total correction procedure:

1. average vertical velocity during phase 1
2. average vertical velocity during phase 2 (used in numerical integration)
3. transition time (used to define transition point)
4. transition height (used to estimate transition point)
5. the azimuth angle for the jet axis
6. the elevation angle for the jet axis
7. the azimuth angle for the phase 1 trajectory
8. the elevation angle for the phase 1 trajectory
9. the horizontal velocity profile in terms of u and v as a function of height (used in numerical integration)

Quite clearly, the combined verification is considerably more complex than the phase 1 verification. Each of the above parameters may be varied independently, leading to several different conclusions about the validity of the correction technique, depending upon which parameters are varied and to what degree. Since generalizing to the degree done in the phase 1 testing is virtually impossible, a case study approach was adopted. This entailed the estimation of the independent parameters from the data for each of the ten trial cases. Specifically, the vertical velocities were calculated from the measured data set; the velocity profiles were obtained by a polynomial regression analysis of sounding data. The measured transition height and time were assumed to be good estimates of actual values. Table B-3 summarizes some of the values used as inputs.

Table B-3 Inputs for the combined testing of the phase 1 and 2 correction techniques

Case #	Transition		Average Vertical velocity		Distance to camera	Jet axis	
	Height (m)	Time (sec)	Phase 1 (m/sec)	Phase 2 (m/sec)		Azimuth (°)	Elevation (°)
TWF026	196	9.0	21.8	11.6	4116	42	30
TWF027	204	9.0	22.7	13.0	4116	42	30
No. 23	172	7.0	24.6	12.3	4116	222	30
TWF037	134	7.0	19.1	7.5	4116	42	30
SIC05	220	5.0	44.0	27.7	3475	22.5	10
TWF056	217	9.0	24.1	15.8	4116	228	30
TWF031	293	13.0	22.5	11.3	4116	42	30
TWF034	148	7.0	21.1	6.6	4116	42	30
TWF033	118	5.0	23.6	13.6	4116	42	30
SIC05	197	5.0	39.4	31.3	3475	22.5	10

To obtain wind data for the numerical integration, soundings for each test were analyzed as follows:

1. Wind velocity and direction were tabulated in intervals of 100 meters to 1000 meters and intervals of 250 meters from 1000 to 2000 meters.

2. The northerly and easterly components of the wind were calculated and subjected to a regression analysis. This resulted in the generation of 5th order polynomials in height for the wind components in each case. This was necessary because the verification required an analytical solution for the trajectory for each case.

Figure B-1 shows the basic flow of the general verification program.

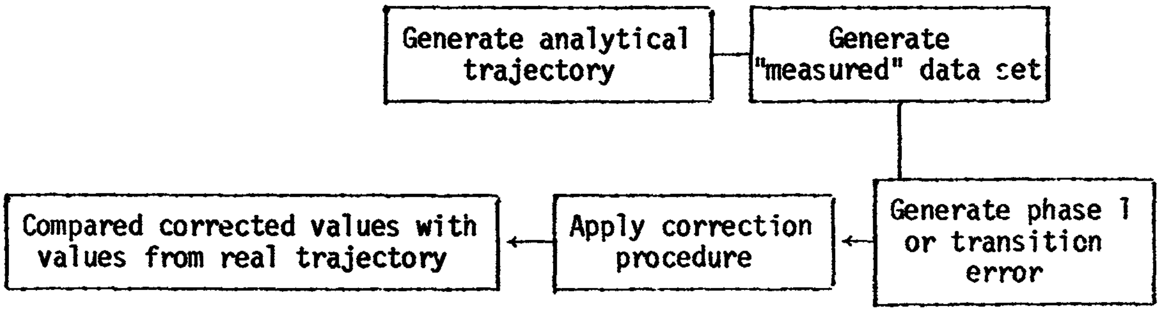

Figure B-1 Flow diagram of verification procedure

B.5 Phase 2 Results

For each case shown in Table B-3, the transition height was varied through four values and the azimuth and elevation angles of the phase 1 trajectory were both independently varied through three values. Thus, twenty-four hypothetical situations were looked at for each case for a total of 240 experiments. Due to the volume of the results, only a few experiments will be presented.

The error in the phase 2 numerical integration can be assessed by setting the phase 1 and transition errors at zero. This results in the conclusion that this error is negligible. Table B-4 which presents both the input and output data for case SIC06 illustrates this. Part b of the table lists the generated or "real" trajectory, the "measured" values, the estimated values and the real and estimated correction factors as functions of time after firing. In this case, the phase 2 period begins at t=5, and any deviation of the estimated values from the generated trajectory must be due to the numerical integration. The largest error occurs at t=37 and, for the X and Z coordinates, amounts to about 1 in 450, which is negligible in comparison with the inherent error of the film measurement technique. However, the error in the Y coordinate is much larger (1 in 63).

Since the integration error is negligible, the effects of transition errors can be assessed by setting the phase 1 error to zero (accomplished by assuming that the phase 1 trajectory is along the jet axis). The transition error is simulated by holding the transition time constant while varying the transition height. In practice, the transition height was set to zero and to values corresponding to ± 100 meters of the transition height. It is highly unlikely that such errors were made in the measurement of the transition height and, therefore, these results overestimate the true error. Tables B-5 and B-6 present the input values and results for the variation of transition height by + 100 and - 100 meters respectively. Since the jet axis, horizontal velocity components, and vertical velocities were not varied, they are presented in Table B-4 only. The underestimation of the transition by 100 meters (Table B-5) in terms of the correction technique is equivalent to the assumption that the cloud is in the phase 2 region

Table B-4 Integration error, SIC06

a. Inputs

Jet axis		1st Phase trajectory		Transition		Vertical velocity	
Azimuth (°)	Elevation (°)	Azimuth (°)	Elevation (°)	Time (sec)	Height (m)	Phase 1 (m/sec)	Phase 2 (m/sec)
10	22.5	10	22.5	5.0	220	44	27.7

Horizontal velocity components

Height	Eastward	Northward
0	2.98	1.96
100	2.49	1.43
200	2.45	1.71
300	2.78	2.39
400	3.40	3.15
500	4.23	3.74
600	5.27	4.02
700	6.53	3.92
800	8.06	3.40
900	9.99	2.50
1000	12.48	1.27
1100	15.75	-0.19

Continued

Table B-4 Integration error, SIC06 - Concluded

b. Results

Time after firing	Generated trajectory			"Measured" values		Estimated values			Correction factors	
t (sec)	X (m)	Y (m)	Z (m)	X (m)	Z (m)	X (m)	Y (m)	Z (m)	Real	Estimated
0	0	0	0	0	0	0	0	0	1.0000	1.0000
3	691	286	132	638	121	691	286	131	1.0824	1.0824
5	1152	477	220	1013	193	1152	477	219	1.1374	1.1374
Transition Point										
7	1157	481	275	1016	241	1157	481	275	1.1385	1.1385
9	1163	486	330	1020	290	1163	485	330	1.1399	1.1397
11	1169	492	386	1024	338	1169	491	386	1.1415	1.1413
13	1176	498	441	1029	386	1176	496	441	1.1434	1.1429
15	1184	505	496	1034	433	1184	503	496	1.1455	1.1449
17	1193	513	552	1039	481	1192	510	552	1.1477	1.1469
19	1203	521	607	1046	528	1202	518	607	1.1500	1.1491
21	1215	529	663	1054	575	1214	526	662	1.1523	1.1514
25	1242	544	773	1073	669	1241	542	773	1.1567	1.1559
29	1276	557	884	1100	762	1276	556	884	1.1604	1.1602
33	1320	565	995	1135	856	1321	568	996	1.1627	1.1636
37	1376	567	1106	1183	951	1379	576	1108	1.1633	1.1657

Table B-5 Transition error = -100 m, SIC06

a. Inputs

1st Phase trajectory		Transition	
Azimuth (°)	Elevation (°)	Time (sec)	Height (m)
10	22.5	5	120

b. Results

Time after firing	Generated trajectory			"Measured" values		Estimated values			Correction factors	
t (sec)	X (m)	Y (m)	Z (m)	X (m)	Z (m)	X (m)	Y (m)	Z (m)	Real	Estimated
0	0	0	0	0	0	0	0	0	1.0000	1.0000
Transition Point										
3	691	286	132	638	121	639	4	122	1.0824	1.0013
5	1152	477	220	1013	193	1015	7	193	1.1374	1.0022
7	1157	481	275	1016	241	1020	11	242	1.1385	1.0034
9	1163	486	330	1020	290	1025	16	291	1.1399	1.0046
11	1169	492	386	1024	338	1031	21	340	1.1415	1.0062
13	1176	498	441	1029	386	1037	27	389	1.1434	1.0078
15	1184	505	496	1034	433	1044	34	438	1.1455	1.0098
17	1193	513	552	1039	481	1052	40	486	1.1477	1.0117
19	1203	521	607	1046	528	1061	48	535	1.1500	1.0140
21	1215	529	663	1054	575	1071	56	584	1.1523	1.0162
25	1242	544	773	1073	669	1096	72	683	1.1567	1.0208
29	1276	557	884	1100	762	1127	87	781	1.1604	1.0250
33	1320	565	995	1135	856	1168	98	880	1.1627	1.0284
37	1376	567	1106	1183	951	1219	106	980	1.1633	1.0306

Table B-6 Transition error = +100 m, SIC06

a. Inputs

1st Phase trajectory		Transition	
Azimuth (°)	Elevation (°)	Time (sec)	Height (m)
22.5	10	5	320

b. Results

Time after firing	Generated trajectory			"Measured" values		Estimated values			Correction factors	
t (sec)	X (m)	Y (m)	Z (m)	X (m)	Z (m)	X (m)	Y (m)	Z (m)	Real	Estimated
0	0	0	0	0	0	0	0	0	1.0000	1.0000
3	691	286	132	638	121	691	286	131	1.0824	1.0824
5	1152	477	220	1013	193	1152	477	219	1.1374	1.1374
7	1157	481	275	1016	241	1158	483	275	1.1385	1.1392
9	1163	486	330	1020	290	1164	490	331	1.1399	1.1410
Transition Point										
11	1169	492	386	1024	338	1170	495	386	1.1415	1.1426
13	1176	498	441	1029	386	1177	501	441	1.1434	1.1442
15	1184	505	496	1034	433	1185	508	497	1.1455	1.1462
17	1193	513	552	1039	481	1194	515	552	1.1477	1.1482
19	1203	521	607	1046	528	1204	522	608	1.1500	1.1504
21	1215	529	663	1054	575	1215	530	663	1.1523	1.1526
25	1242	544	773	1073	669	1242	546	774	1.1567	1.1572
29	1276	557	884	1100	762	1277	561	885	1.1604	1.1614
33	1320	565	995	1135	856	1323	572	997	1.1627	1.1648
37	1376	567	1106	1183	951	1381	580	1109	1.1633	1.1670

from the time of firing. This results from the fact that the correction technique requires that transition height be equivalent to one of the vertical coordinates of the generated trajectory. Because the time sequence (0, 3, 5, 7, etc.) used is discrete, the transition height is adjusted to a height corresponding to the transition point in Table B-3 as follows:

if $Z_n < Z_T < Z_{n+1}$

then $Z_{TP} = Z_n$

where Z_n and Z_{n+1} are two consecutive vertical coordinates of the generated trajectory and, Z_T and Z_{TP} are the transition height and point respectively.

Two major points may be drawn from Table B-5: (1) the estimated values (with the exception of the Y coordinate) are better estimators of the generated trajectory than the "measured" values, and (2) that the Y estimate cannot be considered accurate and, therefore, represents a parameter from which the X and Z estimates can be calculated (for more details of the nature of the Y estimate see Appendix A).

Table B-6 indicates that overestimation of transition height has considerably less impact on the error in the correction than underestimation. The X and Z estimates are accurate to one in seven.

The error caused by deviations of the phase 1 trajectory from the jet axis was assessed by setting the transition error to zero. In terms of the accuracy of the estimated values, as compared to the measured values, there exists isolated points for which the measured value is a better estimator. Table B-7 gives an example of this.

The correction factor results for t=5 indicate that the measured value is a better estimator of the generated trajectory, however, in practical terms the error in both is the same.

Table B-7 Azimuth error = -10°, SIC06

a. Inputs

1st Phase trajectory		Transition	
Azimuth (°)	Elevation (°)	Time (sec)	Height (m)
12.5	10	5	220

b. Results

Time after firing	Generated trajectory			"Measured" values		Estimated values			Correction factors	
t (sec)	X (m)	Y (m)	Z (m)	X (m)	Z (m)	X (m)	Y (m)	Z (m)	Real	Estimated
0	0	0	0	0	0	0	0	0	1.0000	
3	730	162	132	698	126	761	314	137	1.0466	1.0906
5	1218.1	270	220	1130.3	204	1305.9	539	235	1.0777	1.1553
Transition point										
7	1223	274	275	1133	255	1311	543	295	1.0788	1.1565
9	1228	278	330	1137	306	1317	549	354	1.0802	1.1581
11	1235	284	386	1141	356	1323	555	413	1.0819	1.1597
13	1242	291	441	1146	407	1331	561	473	1.0837	1.1617
15	1250	298	496	1151	457	1339	568	532	1.0858	1.1637
17	1259	305	552	1157	507	1349	576	591	1.0880	1.1659
19	1269	313	607	1163	557	1359	584	651	1.0903	1.1681
21	1280	322	663	1171	606	1371	592	710	1.0926	1.1704
25	1307	337	773	1192	705	1400	607	828	1.0970	1.1746
29	1342	350	884	1219	803	1436	618	946	1.1007	1.1780
33	1386	358	995	1256	902	1483	626	1065	1.1030	1.1802
37	1442	360	1106	1306	1002	1543	628	1183	1.1036	1.1808

The remaining nine cases are similar, with the combined errors of the first phase trajectory and transition both augmenting and nulifying the general error of the correction technique. In the case that the errors augment each other, there are isolated sets of points for which the measured values are better estimators. However, these points are a minority, and it may be argued that the use of the estimated values increases the overall accuracy of the data.

Table C-1 Static engine exhaust cloud data

Time (sec)	Height of Cloud Rise, z (m)	Cloud Area, A (m^2)	Rate of Cloud Rise dz/dt ($m\ sec^{-1}$)
Case TWF034			
3	74	4119	36.3
5	123	9946	14.0
7	151	14315	3.5
9	158	16153	20.2
11	198	22650	8.2
13	215	27137	10.8
15	236	29780	14.3
17	265	34994	13.8
19	293	37173	10.2
21	313	43622	9.3
25	351	49037	8.8
29	386	57203	9.7
33	425	68328	6.7
37	452	73022	7.6
41	483	77752	2.9
45	495	84620	7.0
49	523	91134	5.9
53	546	100450	8.5
57	580	109550	8.3
61	614	116360	8.5
65	648	125240	5.4
69	670	134930	6.9
73	698	142940	7.3
77	727	136930	5.1
81	748	149560	2.3
85	757	149510	6.0
89	781	152970	1.6

Continued

Table C-1 Static engine exhuast cloud data - Continued

Time (sec)	Height of Cloud Rise, z (m)	Cloud Area, A (m^2)	Rate of Cloud Rise dz/dt $(m\ sec^{-1})$
Case TWF034 - Continued			
93	788	150870	8.3
97	821	152410	
Case TWF033			
3	78	4245	20.5
5	119	8538	9.6
7	139	14104	11.5
9	162	19279	22.7
11	207	26441	18.9
13	245	31651	16.8
15	279	38360	12.0
17	303	42748	8.7
19	320	49999	9.9
21	340	63295	10.3
25	382	70205	13.5
29	436	81981	16.1
33	500	87377	16.0
37	565	100450	16.2
41	630	114350	13.6
45	684	130610	12.8
49	736	150710	
Case TWF031			
3	130	8956	17.7
5	166	13385	15.2
7	197	17804	20.8
9	238	22235	14.9
11	268	27758	17.4

Continued

Table C-1 Static engine exhaust cloud data - Continued

Time (sec)	Height of Cloud Rise, z (m)	Cloud Area, A (m^2)	Rate of Cloud Rise dz/dt ($m\ sec^{-1}$)
Case TWF031 - Continued			
13	303	33020	12.1
15	328	37880	12.9
17	353	45025	20.1
19	394	47232	10.4
21	415	51831	10.8
25	458	53369	10.7
29	501	59928	12.4
33	550	63729	9.7
37	587	71281	
Case TWF056			
3	90	6302	22.5
5	135	12658	22.0
7	179	15702	21.5
9	222	20872	13.1
11	248	27293	16.9
13	282	31223	22.9
15	328	37653	18.8
17	366	46762	21.4
19	409	55877	16.3
21	442	60379	18.4
25	515	76864	19.3
29	593	100120	21.3
33	678	121780	19.2
37	755	150320	17.4
41	825	155620	14.2
45	882	181680	12.3
49	931	207110	11.6

Continued

Table C-1 Static engine exhaust cloud data - Continued

Time (sec)	Height of Cloud Rise, z (m)	Cloud Area, A (m^2)	Rate of Cloud Rise dz/dt ($m\ sec^{-1}$)
Case TWF056 - Continued			
53	978	245830	15.2
57	1039	243200	
Case TWF037			
3	98	7007	10.0
5	118	11289	9.3
7	137	16241	9.6
9	156	21318	13.5
11	183	25532	17.6
13	218	29878	12.5
15	244	34925	14.0
17	272	41036	17.4
19	307	39897	7.1
21	321	45649	11.0
25	365	53726	9.5
29	403	64801	6.4
33	429	71503	7.9
37	461	77830	6.1
41	485	88483	9.0
45	522	99211	6.3
49	547	104080	7.8
53	578	114160	7.1
57	607	126490	10.1
61	647	141020	6.4
65	673	147100	9.7
69	712	158580	6.1
73	737	173300	4.3
77	754	188690	7.1

Continued

Table C-1 Static engine exhaust cloud data - Continued

Time (sec)	Height of Cloud Rise, z (m)	Cloud Area, A (m^2)	Rate of Cloud Rise dz/dt ($m\ sec^{-1}$)
Case TWF037 - Continued			
81	783	204660	3.6
85	797	217900	2.7
89	808	233010	13.5
93	863	268390	14.5
97	868	274210	6.6
101	895	298110	5.5
105	917	317780	-2.9
109	906	308540	5.1
113	926	345300	
Case TWF027			
3	117	8556	9.0
5	135	14137	17.0
7	169	19859	20.5
9	210	26530	19.5
11	249	31463	21.1
13	291	41023	15.8
15	323	46997	11.5
17	346	48101	11.1
19	369	50948	13.1
21	395	54089	12.7
25	446	62408	15.2
29	507	81151	14.4
33	564	85750	20.0
37	644	112630	18.8
41	720	140440	13.2
45	773	151730	13.5
49	827	173220	16.4

Continued

Table C-1 Static engine exhaust cloud data - Continued

Time (sec)	Height of Cloud Rise, z (m)	Cloud Area, A (m^2)	Rate of Cloud Rise dz/dt ($m\ sec^{-1}$)
Case TWF027 - Continued			
53	893	204040	11.7
57	940	216370	12.0
61	988	248780	13.2
65	1041	264630	8.5
69	1075	293520	6.0
73	1100	298950	
Case TWF026			
3	87	7149	16.5
5	120	11400	22.5
7	165	18252	18.0
9	201	20045	10.7
11	223	23517	15.7
13	254	29817	14.2
15	283	35224	18.2
17	319	40560	15.9
19	351	45958	12.9
21	377	51913	9.3
25	415	62274	11.6
29	461	68249	12.0
33	510	80283	11.7
37	557	87445	12.1
41	605	98315	12.0
45	654	103590	8.1
49	686	110990	7.8
53	717	127300	10.3
57	759	139410	9.8
61	799	148190	

Continued

Table C-1 Static engine exhaust cloud data - Continued

Time (sec)	Height of Cloud Rise, z (m)	Cloud Area, A (m^2)	Rate of Cloud Rise dz/dt ($m\ sec^{-1}$)
Case No. 23			
3	108	9718	12.6
5	133	13024	19.4
7	172	16826	10.0
9	192	20881	13.4
11	219	26026	23.7
13	266	29790	17.6
15	302	36736	15.2
17	332	38395	16.8
19	366	47299	20.8
21	407	51686	16.2
25	472	70319	14.7
29	531	82184	12.3
33	581	98918	9.4
37	619	116000	4.8
41	638	121750	10.1
45	679	136360	10.1
49	719	137050	7.8
53	751	151480	8.7
57	786	148410	
Case SIC05			
3	84	13450	57.2
5	198	40533	32.8
7	264	63621	49.9
9	364	82264	42.9
11	450	120620	32.7
13	515	155720	36.8
15	589	186920	32.8

Continued

Table C-1 Static engine exhaust cloud data - Concluded

Time (sec)	Height of Cloud Rise, z (m)	Cloud Area, A (m^2)	Rate of Cloud Rise dz/dt ($m\ sec^{-1}$)
Case SIC05 - Continued			
17	654	210580	14.8
19	684	232790	27.4
21	739	246740	36.0
25	883	249920	36.9
29	1031	284270	29.9
33	1151	323870	25.8
37	1254	381300	
Case SIC06			
3	142	19725	40.0
5	222	40053	31.9
7	286	61394	35.8
9	358	81413	32.6
11	423	108490	24.9
13	473	134880	29.3
15	531	172420	20.2
17	572	186030	21.5
19	615	213080	31.8
21	679	234900	26.1
25	784	283380	25.5
29	886	333300	28.9
33	1001	380790	26.0
37	1105	431350	

Table C-2 Meteorological data, Case TWF034, 2221Z, September 10, 1964

Height (m)	Temperature (°C)	Pressure (mb)	Humidity (%)	Wind Direction (degree)	Wind Speed ($m\ sec^{-1}$)
0	15.9	1002	43	310	3.1
100	15.1	990	39	328	4.8
200	14.3	979	36	346	6.6
300	13.3	967	38	349	6.7
400	12.3	956	42	350	6.3
500	11.1	944	46	351	6.3
600	10.2	933	49	351	6.4
700	9.3	922	52	351	6.7
800	8.6	911	55	351	6.7
900	7.8	900	59	351	6.7
1000	6.7	889	59	350	6.6
1250	4.2	862	58	343	6.3
1500	5.0	836	11	328	6.5
1750	4.5	811	11	317	7.3
2000	3.7	786	9	312	8.1

Table C-3 Meteorological data, Case TWF033, 2306Z, August 25, 1964

Height (m)	Temperature (°C)	Pressure (mb)	Humidity (%)	Wind Direction (degree)	Wind Speed ($m\ sec^{-1}$)
0	22.5	1000	94	130	2.1
100	22.4	989	86	138	3.3
200	22.4	977	78	147	4.5
300	22.3	966	72	155	4.3
400	22.2	955	67	163	3.6
500	21.9	944	66	187	3.6
600	21.5	934	66	218	4.1
700	21.1	923	69	239	4.9
800	20.7	912	75	250	6.0
900	20.3	902	75	259	6.3
1000	19.9	892	74	267	6.3
1250	18.5	866	67	280	6.6
1500	17.9	841	64	285	7.0
1750	16.7	817	59	288	7.3
2000	15.3	793	55	293	7.4

Table C-4 Meteorological data, Case TWF031, 1729Z, August 4, 1964

Height (m)	Temperature (°C)	Pressure (mb)	Humidity (%)	Wind Direction (degree)	Wind Speed (m sec^{-1})
0	33.1	997	60	250	3.1
100	31.6	986	54	262	3.7
200	30.1	975	49	274	4.4
300	29.0	964	53	272	4.5
400	28.1	953	55	275	4.8
500	27.3	943	58	282	5.1
600	26.3	932	59	292	5.4
700	25.7	922	61	301	5.7
800	25.7	911	61	311	6.2
900	25.4	901	57	319	7.1
1000	25.1	891	52	326	8.0
1250	24.8	866	39	338	9.7
1500	22.7	842	41	344	10.6
1750	20.6	818	46	348	10.6
2000	18.4	794	58	351	10.4

Table C-5 Meteorological data, Case TWF056, 2000Z, May 26, 1965

Height (m)	Temperature (°C)	Pressure (mb)	Humidity (%)	Wind Direction (degree)	Wind Speed (m sec^{-1})
0	31.3	991	48	210	4.6
100	29.9	980	38	207	5.1
200	28.5	969	28	204	5.7
300	27.5	958	32	207	6.0
400	26.3	947	36	207	6.4
500	25.1	937	41	203	7.3
600	24.2	926	44	198	8.3
700	23.3	916	47	195	9.0
800	22.5	905	50	195	8.9
900	21.4	895	53	195	8.6
1000	20.2	884	57	195	8.1
1250	18.0	859	60	201	8.7
1500	15.7	834	64	206	8.9
1750	13.3	810	65	212	9.6
2000	11.6	786	73	219	11.3

Table C-6 Meteorological data, Case TWF037, 2240Z, October 23, 1964

Height (m)	Temperature (°C)	Pressure (mb)	Humidity (%)	Wind Direction (degree)	Wind Speed (m sec^{-1})
0	15.2	1007	43	330	[illegible].1
100	14.9	995	31	346	6 3
200	14.6	983	20	3	9.5
300	13.8	972	21	3	9.5
400	12.9	960	22	2	9.4
500	11.9	949	23	360	9.3
600	11.0	938	24	358	9.1
700	10.0	927	26	357	9.1
800	9.1	915	29	357	9.1
900	8.3	904	28	357	9.4
1000	7.6	894	23	358	9.9
1250	8.2	867	18	358	10.7
1500	7.8	841	26	355	11.0
1750	6.4	816	23	351	11.4
2000	5.5	791	22	34[illegible]	11.1

Table C-7 Meteorological data, Case TWF027, 2254Z, October 7, 1964

Height (m)	Temperature (°C)	Pressure (mb)	Humidity (%)	Wind Direction (degree)	Wind Speed (m sec^{-1})
0	29.0	996	54	20	5.7
100	27.9	985	48	22	4.7
200	27.0	974	45	24	4.3
300	26.1	963	47	27	4.7
400	25.1	952	49	24	5.0
500	24.2	941	50	17	5.1
600	23.5	931	52	7	5.0
700	22.5	920	53	357	5.0
800	21.7	909	54	346	5.0
900	21.2	899	55	335	5.1
1000	20.4	889	58	326	5.3
1250	18.2	863	64	313	5.9
1500	16.2	838	65	311	6.9
1750	14.3	814	64	312	8.2
2000	12.6	790	64	314	9.7

Table C-8 Meteorological data, Case TWF026, 2219Z, September 7, 1964

Height (m)	Temperature (°C)	Pressure (mb)	Humidity (%)	Wind Direction (degree)	Wind Speed $(\mathrm{m\ sec}^{-1})$
0	28.1	994	75	250	2.1
100	27.9	983	70	263	5.8
200	27.6	972	67	275	9.4
300	26.7	961	67	273	9.3
400	25.9	950	67	273	9.1
500	25.1	940	67	275	8.5
600	24.5	929	67	279	7.8
700	23.8	919	67	283	7.2
800	23.1	908	67	285	6.7
900	22.2	898	67	290	6.1
1000	21.4	888	66	297	5.5
1250	19.4	862	71	324	4.1
1500	17.5	838	74	330	4.6
1750	15.7	813	74	330	4.9
2000	14.2	790	67	327	5.4

Table C-9 Meteorological data, Case No. 23, 2237Z, September 24, 1964

Height (m)	Temperature (°C)	Pressure (mb)	Humidity (%)	Wind Direction (degree)	Wind Speed (m sec^{-1})
0	21.8	1001	35	300	2.1
100	21.6	989	30	309	4.9
200	21.5	978	25	319	7.7
300	20.6	967	24	323	8.4
400	19.5	955	24	323	8.5
500	18.6	944	24	320	8.2
600	17.6	933	25	315	7.9
700	16.5	923	25	310	7.6
800	15.7	912	26	308	7.9
900	14.7	901	27	305	8.0
1000	13.7	890	28	302	7.8
1250	11.1	864	28	292	6.9
1500	8.7	839	31	295	8.0
1750	7.2	814	27	303	9.4
2000	7.0	789	20	310	12.8

Table C-10 Meteorological data, Case SIC05, 2110Z, May 6, 1965

Height (m)	Temperature (°C)	Pressure (mb)	Humidity (%)	Wind Direction (degree)	Wind Speed (m sec^{-1})
0	28.5	1002	36	210	1.5
100	26.9	990	46	177	2.7
200	25.5	979	54	150	4.0
300	24.6	968	55	155	5.4
400	23.7	957	57	161	6.6
500	22.7	946	58	172	6.8
600	21.7	935	59	176	8.0
700	20.9	925	61	174	9.9
800	20.0	914	62	177	10.2
900	19.1	904	64	182	10.4
1000	18.1	893	66	188	10.5
1250	15.6	867	70	188	12.3
1500	13.1	842	72	187	13.5
1750	11.0	817	70	188	15.8
2000	10.8	793	50	195	13.7

Table C-11 Meteorological data, Case SIC06, 1900Z, May 20, 1965

Height (m)	Temperature (°C)	Pressure (mb)	Humidity (%)	Wind Direction (degree)	Wind Speed (m sec^{-1})
0	27.5	1001	59	60	3.5
100	26.4	990	63	55	3.2
200	25.4	979	67	50	2.8
300	24.3	968	69	48	3.3
400	23.3	957	70	49	4.7
500	22.3	946	71	50	6.2
600	21.3	935	70	53	6.4
700	20.3	924	70	55	6.6
800	19.4	914	69	60	6.9
900	18.8	903	66	68	7.4
1000	18.3	893	64	77	7.9
1250	17.4	867	58	108	8.9
1500	15.6	842	65	133	9.4
1750	13.7	818	63	154	9.8
2000	12.2	794	40	173	11.1

APPENDIX D: METHOD OF SOLUTION TO THE CUBIC EQUATION (Equation 2-30) DETERMINING THE TRANSITION HEIGHT OF EXHAUST CLOUD RISE

Recall the following equation for determining the transition height of exhaust cloud rise:

$$\frac{1}{k^3 z_1^{\,4}} \left[\frac{3}{2} \frac{Ag}{\theta_e c^2} + \frac{1}{z_1^{\,2}} \left(w_o^{\,3} z_o^{\,3} - \frac{3}{2} \frac{Ag}{\theta_e c^2} z_o^{\,2}\right)\right] = 1. \qquad (2\text{-}30)$$

This is Equation (2-30) in Section 2.2.2.1.3.

The equation will now be rewritten as

$$\frac{3}{2} \frac{Ag}{\theta_e c^2 k^3} \frac{1}{(z_1^{\,2})^2} + \left[\frac{1}{k^3} \left(w_o^{\,3} z_o^{\,3} - \frac{3}{2} \frac{Ag}{\theta_e c^2} z_o^{\,2}\right)\right] \frac{1}{(z_1^{\,2})^3} = 1 \qquad (\text{D-1})$$

Now, let.

$$a = \frac{3}{2} \frac{Ag}{\theta_e c^2 k^3} \qquad (\text{D-2})$$

$$b = \frac{1}{k^3} \left(w_o^{\,3} z_o^{\,3} - \frac{3}{2} \frac{Ag}{\theta_e c^2} z_o^{\,2}\right) \qquad (\text{D-3})$$

$$Z = z_1^{\,2}.$$

Substitution of Equations (D-2), (D-3), and (D-4) into Equation (D-1) will yield

$$\frac{a}{Z^2} + \frac{b}{Z^3} - 1 = 0.$$

Multiply both sides of Equation (D-5) and rearrange terms, and we have:

$$Z^3 - aZ - b = 0 \qquad \text{(D-6)}$$

which is a cubic equation in Z $(z_1{}^2)$.

The solution to Equation (D-6) is well known and can be written as

$$Z = A + B,\ -\frac{A+B}{2} + \frac{A-B}{2}\sqrt{-3},\ -\frac{A+B}{2} - \frac{A-B}{2}\sqrt{-3} \qquad \text{(D-7)}$$

where

$$A = \sqrt[3]{\frac{b}{2} + \sqrt{\frac{b^2}{4} - \frac{a^3}{27}}} \qquad \text{(D-8)}$$

$$B = \sqrt[3]{\frac{b}{2} - \sqrt{\frac{b^2}{4} - \frac{a^3}{27}}}\ . \qquad \text{(D-9)}$$

The solution of Z from Equation (D-7) will vary according to the following situations:

If $b^2/4 - a^3/27 > 0$, there will be one real root and two conjugate imaginary roots.

If $b^2/4 - a^3/27 = 0$, there will be three real roots of which two at least are equal.

If $b^2/4 - a^3/27 < 0$, there will be three real and unequal roots.

Obviously, the solution we are interested in is the first root in Equation (D-7).

$$Z = A + B \qquad \text{(D-10)}$$

In order to obtain (D-10), the following conditions have to be satisfied:

$b^2/4 - a^3/7 > 0$, in this case the real root $Z = A + B$ is desired.

$b^2/4 - a^3/7 = 0$, in this case, $A = B$, or $Z = 2A = 2B$ is the root desired.

Combining the two relationships and writing them in terms of real parameters, we have

$$\frac{\left[k^{-3}\left(w_o{}^3 z_o{}^3 - \frac{3}{2}\frac{Ag}{\theta_e c^2} z_o{}^2\right)\right]^2}{4} \geqq \frac{\left[\frac{3}{2}\frac{Ag}{\theta_e c^2 k^3}\right]^3}{27} \tag{D-11}$$

which is identical with (2-29) in Section 2.2.2.3.

When the situation $b^2/4 - a^3/7 = 0$ arises, a further condition has to be met in order to have solution in Z:

$$b > 0 \tag{D-12}$$

or

$$w_o{}^3 z_o{}^3 > \frac{3}{2}\frac{Ag}{\theta_e c^2} z_o{}^2 \tag{D-13}$$

which, incidentally, is (2-28) in Section 2.2.2.3.

When Equation (D-11) is not satisfied under general conditions or Equation (D-13) is not satisfied under the special situation just described, iterative methods will have to be used to solve Equation (2-26) numerically.